# DEVELOPING A MAGNETIC-BASED FORCE SPECTROSCOPY WITH HIGH MOLECULAR RESOLUTION

A Dissertation

Presented to

the faculty of the Department of Chemistry

University of Houston

In Partial Fulfillment

of the Requirements for the Degree

Doctor of Philosophy

By

Lashan Madusha De Silva

August 2014

# DEVELOPING A MAGNETIC-BASED FORCE SPECTROSCOPY WITH HIGH MOLECULAR RESOLUTION

Lashan Madusha H. De Silva

APPROVED:

Dr. Shoujun Xu, Chairman
Department of Chemistry

Dr. Steven Baldelli
Department of Chemistry

Dr. Allan Jacobson
Department of Chemistry

Dr. Ding-Shyue Yang
Department of Chemistry

Dr. YuhongWang
Department of Biology & Biochemistry

Dean, College of Natural Sciences and Mathematics

# Acknowledgements

I would like to thank my advisor, Associate Professor Dr. Shoujun Xu for his continuous support, suggestions, assistance, encouragement, and kindness throughout my graduate career. His knowledge and ideas have been a great resource and inspiration.

I am grateful to Faculty members at the Department of Chemistry, College of Natural Science and Mathematics, University of Houston for providing the great knowledge in chemistry and made me feel that University of Houston is a great place to study in. I am thankful to the staff of the chemistry department for effort they have spent supporting my research and easing my work.

I would like to express my appreciation to all of my great colleagues that I have been working with. Dr. Li Yao, a postdoc, has always been there to help me out. All the help from him is priceless to me. I would like to acknowledge other former and current members of my research group for their collaborate, support and good-fellowship over the years, including Dindi Yu, Nissa Garcia, Songtham Ruangchaithaweesuk, Bian Hu, Vasudeva Chintamsetti, Qiongzheng Hu, Yi-Ting Chen, Te-Wei Tsai, Haina Jia and Lecheng Zhang.

Finally I would like to thank the most important people in my life. To the one and only, my wife Anuradha, for being my life, my love and my sunshine. Without her this thesis would never exists. I owe her an enormous, unpayable debt. To my parents for their love, support and encouragement throughout my life and who made me a person I am today. Nothing that I have accomplished would have been possible without them. I dedicate this dissertation to my wife and my parents.

# DEVELOPING A MAGNETIC-BASED FORCE SPECTROSCOPY WITH HIGH MOLECULAR RESOLUTION

An Abstract of a Dissertation

Presented to

the faculty of the Department of Chemistry

University of Houston

In Partial Fulfillment

of the Requirements for the Degree

Doctor of Philosophy

By

Lashan Madusha De Silva

August 2014

# Abstract

Magnetic materials are widely used in chemistry, biology, and medicine. Consequently, many magnetic-based techniques have been developed to facilitate these applications by providing quantity, spatial information, and molecular specificity for the targeted molecules. However, each of the three aspects represents a challenge for the techniques, namely, sensitivity, resolution, and specificity, respectively. Recently, our group has reported several new techniques for quantitative and molecule-specific detection of magnetic signals. Using an atomic magnetometer coupled with a scanning detection method, as low as $10^3$ magnetically labeled molecules can be detected; using the force-induced remnant magnetization spectroscopy (FIRMS) technique, specific molecular bonds can be distinguished from nonspecific absorption. These progresses have paved the way for the research reported here.

In this dissertation, I will present two major achievements in resolving molecular information using the FIRMS technique. The first is obtaining high resolution in measuring the noncovalent binding forces between molecules using the FIRMS technique. The force resolution of 1.8 pN is nearly an order of magnitude better than the current state-of-the-art technique—atomic force microscopy (AFM). This high resolution enables precise determination of the targeted noncovalent bonds hence the molecules of interest. DNA duplexes with a single basepair difference can be completely resolved in the same sample, which cannot be accomplished by AFM or any other force spectroscopic techniques. The other accomplishment is using acoustic radiation force to distinguish molecular interactions for the first time. Antibodies of different subclasses and DNAs with different

binding forces can be clearly identified. The small size of the ultrasound transducer allows for potential integration with the atomic magnetometer. The resulting instrument will be uniquely suitable for noninvasive manipulation of molecular interactions.

This dissertation is organized as follows. In Chapter 1, I will provide an overview of magnetic materials and the related detection techniques. The principle of FIRMS will be introduced. Chapter 2 will be the principle of atomic magnetometry. This is the basis of the detection method for FIRMS and its derived techniques. Chapters 3 and 4 will describe in details the research progresses, both of which have been published. In Chapter 5, I will present an ongoing project that concerns building an apparatus that integrates an ultrasound probe and an atomic magnetometer. The goal is to ultimately achieve detection and manipulation of molecule-specific noncovalent bonds. Preliminary results have demonstrated feasibility of such an apparatus.

# Contents

# List of Figures

# List of Tables

# Chapter 1

# Overview: Magnetic Materials and Molecular Imaging

Magnetic materials have found many valuable applications in biomedical research and biotechnology. In particular, magnetic particles are used in cell separation, immunoassay, drug and gene delivery, radionuclide therapy, hyperthermia and magnetic resonance imaging (MRI). Magnetic particles are attractive for these applications due to their physical properties. The magnetic field they produce can be detected precisely with various techniques. In addition, these particles can be manipulated by an external magnetic field to facilitate applications in separation, immunoassay and drug targeting. Another feature of magnetic particles is hysteresis when they are subjected to an alternating magnetic field, which leads to the applications in hyperthermia treatment [1].

This dissertation mainly focuses on using magnetic particles in molecular imaging by resolving the different molecular bonds labeled with magnetic particles. Molecular imaging is the predominant diagnostic discipline that aims to visually characterize normal and pathological processes at the molecular and cellular levels under in vitro condition or in living organisms. The technique presented here is the force-induced remnant magnetization spectroscopy (FIRMS) technique, which couples an atomic magnetometer with mechanical manipulation of noncovalent bonds. Before discussing the technique in details, I will provide a brief description of magnetic materials and their properties.

The power of magnetite or lodestones ($Fe^{II}OFe^{III}{}_2O_3$) to attract iron appeared in Greek writings as early as 600 B.C. It has been claimed that the Chinese used the compass before 2,500 B.C. Thus some of mankind's earliest scientific discoveries are related to magnetism. P. Peregrines discovered the two regions called magnetic poles which attracted a piece of iron more strongly than the rest of the magnetite in 1269 A.D. William Gilbert (1540-1603) realized that the Earth is a huge magnet and now it is known that the Earth has a magnetic field of approximately $5 \times 10^{-5}$ T. Charles Coulomb (1736 – 1806) found that there were two types of poles, now known as the North (positive) and South (negative) Poles [2]. Like poles repel each other and unlike poles attract each other. Now this phenomenon is explained in terms of magnetic dipoles contained in magnetic materials.

## 1.1 Magnetic dipoles and magnetic field vectors

Magnetism emerges from the moving charged particles and it is convenient to consider magnetic forces in terms of magnetic fields. A magnetic field exists in region of

space near a magnet, electric current, or moving charge particle in which magnetic force acts on any other magnet, electric current, or moving charge particle. Imaginary lines can be drawn to indicate the direction of the magnetic force at any point in the field. Force lines of a bar magnet is shown in the Figure 1.1 [3].

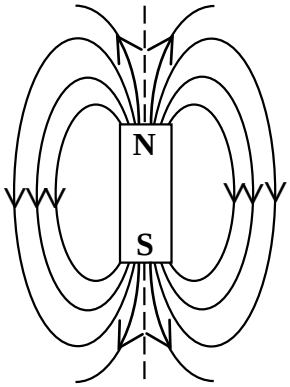


Figure 1.1 Magnetic force lines around a bar magnet. Magnetic force lines are drawn from north pole to south pole outside the magnet.

Magnetic dipoles in magnetic materials can be considered as small bar magnets with north and south poles. The force of the magnetic field itself exerts a torque that tends to orient the dipole with the field. Magnetic dipole moments are simply represented by arrows as shown in the Figure 1.2.

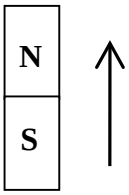


Figure 1.2 Representation of the magnetic dipole moment of a bar magnet.

Magnetic behavior of magnetic materials can be described in terms of several field vectors. The magnetic field strength or the externally applied magnetic field is denoted by

$H$. The $H$ field generated by a cylindrical coil (or solenoid) with length $l$ and $N$ closely spaced turns, which is carrying a current $I$ [4], is given by

$$H = nI. \tag{1.1}$$

where $n$ is the number of turns per unit length ($n = N/l$). The magnetic field that is generated by a bar magnet in Figure 1.1 is an $H$ field. Thus units of H are ampere-turns per meter or simply amperes per meter.

When a material is placed in an external magnetic field, the magnetic moments of atoms response to the external field, resulting in magnetic inductance in the material. The magnitude of the internal magnetic field strength of a substance that is subjected to an $H$ field is represented by the magnetic flux density or by the magnetic induction. This is represented by $B$ and given by Equation 1.2. $B$ has the unit of Tesla [or webers per square meter ($\mathrm{Wb/m^2}$); weber is the units that used for measuring magnetic pole strength].

$$B = \mu_0 (M + H) \tag{1.2}$$

where $\mu_0$ is the permeability of a vacuum. The permeability has the unit of newtons per ampere squared ($\mathrm{N/A^2}$) or henries per meter ($\mathrm{H/m}$). The value of $\mu_0$ is $4\,\pi \times 10^{-7}$ $\mathrm{H/m}$.

$M$ is called the magnetization of the material, which represents the magnetic dipole moment $m$ per unit volume as shown by Equation 1.3 [5]. Magnetic dipole moment is in $\mathrm{Am^2}$ thus magnetization has the unit of Amperes per meter.

$$M = \frac{m}{V} \tag{1.3}$$

The value of $M$ depends on the type of the material and temperature. $M$ is related to the applied field according the following equation,

$$M = \chi_m H \tag{1.4}$$

where $\chi_m$ is called the magnetic susceptibility, a unitless parameter. The magnetic susceptibility is related to the relative permeability ($\mu_r$) as follows:

$$\chi_m = \mu_r - 1 \tag{1.5}$$

The relative permeability is the ratio between the permeability of a material and vacuum. It can be denoted by the equation,

$$\mu_r = \frac{\mu}{\mu_0} \tag{1.6}$$

where $\mu$ is the permeability of the material. The relative permeability or permeability is a measure of the degree to which the material can be magnetized. Thus $\mu$ or $\mu_r$ is one of the parameters used to describe the magnetic properties of materials.

There are two commonly used systems for magnetic units: SI system (meter-kilogram-seconds) and cgs-emu system (centimeter-gram-second-electromagnetic unit). Throughout this thesis we use SI unit system. Table 1.1 summaries the relevant magnetic units in SI system with the corresponding conversion factors for cgs system.

Table 1.1 Magnetic units of SI system

| Quantity | Symbol | SI units | |
|---|---|---|---|
| | | Primary | Conversion factor |
| Magnetic field strength | H | A/m | A/m = $4\pi \times 10^{-3}$ oersted (Oe) |
| Magnetic induction | B | $kg/As^2$ | $kg/As^2$ = Tesla = $10^4$ gauss (G) |
| Magnetization | M | A/m | A/m = $10^{-3}$ maxwell/$cm^2$ |
| Magnetic dipole moment | m | $Am^2$ | $Am^2 = 10^3$ gauss $cm^3$ |
| Permeability of vacuum | $\mu_0$ | $kgm/A^2s^2$ | $4\pi \times 10^{-7}$ H/m ($N/A^2$) |
| Relative permeability | $\mu_r$ | Unitless | Unitless |
| Magnetic Susceptibility | $\chi_m$ | Unitless | Unitless |

## 1.2 Origin of magnetic moment

Macroscopic magnetic properties of a material are a sequel of magnetic moments associated with individual electrons. For the simplicity, here we use classical Bohr model for explaining the origin of magnetic moments. But it should be noted that the quantum mechanical picture of magnetic moment origin is more complicated than the classical model. As schematically illustrated in Figure 1.3, the magnetic moments of each electron are originated from two sources. The first source is the orbital motion of an electron around the nucleus. A moving electron can be considered as a small current loop, which generates a very small magnetic field with magnetic moment along its rotation axis.

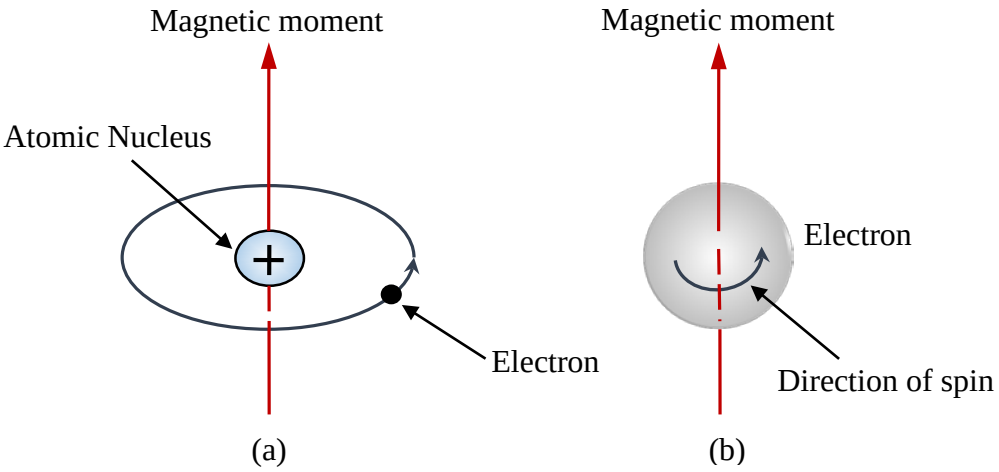


Fig 1.3 Representation of the magnetic moment associated with (a) orbital motion of an electron and (b) spinning of an electron.

The second source is the spinning of an electron. This magnetic moment is directed along the spinning axis. The direction of the spin magnetic moments is either “up” or “down”. Thus an electron in an atom may be considered as a small magnet having orbital and spin magnetic moments. The **Bohr magneton** $\mu_B$ is the most fundamental magnetic

moment and has a value of $9.27 \times 10^{-24}$ $Am^2$. The spin magnetic moment of an electron is $\pm \mu_B$. The orbital magnetic moment contribution is $m_l \mu_B$, where $m_l$ is the magnetic quantum number [6].

## 1.3 Categories of magnetic materials

The net magnetic moment of an atom is the sum of the magnetic moments of each constituent electron, including both orbital and spin contributions. However, the orbital and spin moments of some electron pairs of an atom are cancelled out. As an example, there is a total cancellation of orbital and spin moments for atoms which have completely filled electron shells or subshells. Consequently, these atoms are not capable of being permanently magnetized. The magnetic response of bulk materials can be understood in terms of the behavior of individual atoms. According to the magnetic response, the materials can be categorized into main magnetism types: diamagnetism, paramagnetism, ferromagnetism, antiferromagnetism and ferrimagnetism [6].

Diamagnetism is a very weak type of magnetism, which is not permanent. It only persists as long as the external field is applied. It emerges from a change in the orbital motion of electrons due to the applied field. This induced magnetic moment has a direction opposite to the applied field. The relative permeability $\mu_r$ of diamagnetic materials is less than one and their magnetic susceptibilities are negative.

In paramagnetism, each atom possess a permanent dipole moments due to incomplete cancellation of its electrons' orbital or/and spin magnetic moments. When there is no external magnetic field, the orientations of these magnetic moments are random and

there is no net macroscopic magnetization. In the presence of an external field, these dipole moments tend to be aligned with the field by rotation. These magnetic dipoles act individually and they do not have any mutual interaction between adjacent dipoles. The relative permeability $\mu_r$ of paramagnetic materials is greater than one and magnetic susceptibilities are positive but have relatively smaller values.

Ferromagnetism refers to materials showing permanent magnetic moments even in the absence of an external magnetic field. It occurs in some transition metals such as iron (body centered cubic α ferrite), cobalt, nickel, and some of the rare earth metals such as gadolinium (Gd). Compared to diamagnetic and paramagnetic materials, ferromagnetic materials have very high susceptibility values on the order of $10^6$.

The permanent magnetic moments of these materials are mainly from the electron spin magnetic moments; electronic structure of the material leads to uncancelled spins. Although there is a contribution from the orbital magnetic moment, it is small compared to spin magnetic moment. In addition, ferromagnetic materials have coupling interactions which result in net spin magnetic moments of adjacent atoms to align with one another in a cooperative fashion. This parallel alignment of spins can exist over a large region in a crystal called magnetic domain. When all the magnetic dipoles of the material aligned with external field, the magnetization reaches its maximum value called saturation magnetization ($M_s$). The saturation magnetization can be calculated as the product of the net magnetic moment per atom and the number of atoms present. For nickel, net magnetic moment per atom is 0.66 $\mu_B$ and the density is $8.90 \times 10^3$ $k\mathrm{g/m^3}$. So then saturation magnetization of nickel is $5.1 \times 10^5$ $\mathrm{A/m}$.

As described above, the coupling forces in ferromagnetic materials result cooperative parallel alignment of spins. In some materials the magnetic coupling between the neighboring atoms (or ions) results in the spin moments in opposite direction (antiparallel alignment). Such a phenomenon is named antiferromagnetism. For example, the magnetic moments of adjacent $Mn^{2+}$ ions in manganese oxide (MnO) are antiparallel, thus the material has no net magnetic moment as illustrated in Figure 1.4 [7].

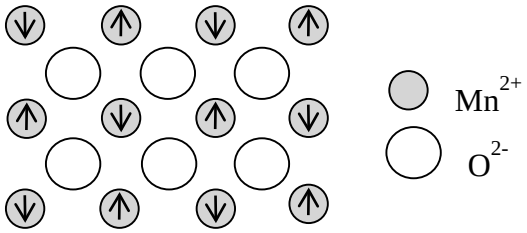


Figure 1.4 Schematic illustration of the antiparallel alignment of spin magnetic moments in antiferromagnetic material MnO.

Some other materials also show permanent magnetic moment in the absence of an external field, which is referred to as ferrimagnetism. The characteristics of the ferrimagnetic are similar to the ferromagnetic materials; the only difference is the source of the net magnetic moment. Cubic ferrites $MFe_2O_4$, where M is a metal, such as magnetite ($Fe_3O_4$), show ferrimagnetic behavior. The structure of $Fe_3O_4$ can be rewritten as $Fe^{2+}O^{2-}$-$(Fe^{3+})_2(O^{2-})_3$ in which Fe ions exist in both +2 and +3 oxidation states. $Fe^{2+}$ and $Fe^{3+}$ ions have different net spin magnetic moments and $O^{2-}$ ions are nonmagnetic. There is a net magnetic moment for $Fe_3O_4$ as a whole structure where the spin magnetic moments are not totally cancelled out. Although magnetic moments of $Fe^{3+}$ are cancelled out by their anti-parallel alignment of spins, the magnetic moments of $Fe^{2+}$ are aligned in the same direction (parallel) as ferromagnets, which results in net magnetic moment for the material. The

schematic representation of the spin magnetic moment configuration of $Fe_3O_4$ is shown in Figure 1.5. Ferrites with different magnetic properties can be generated by adding other ions such as $Co^{2+}$ and $Ni^{2+}$ to $Fe_3O_4$ [8].

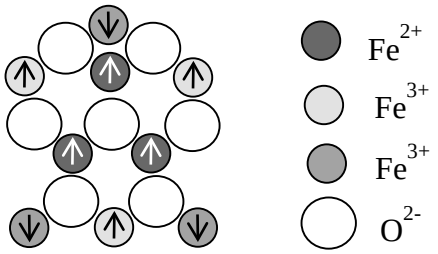


Figure 1.5 Schematic of spin magnetic moment configuration of $Fe_3O_4$.

The magnetic properties of materials change with temperature. For example, magnetic properties of ferromagnetic and ferrimagnetic materials depend on coupling forces between neighboring atoms; at higher temperatures, random orientations of spins are favorable due to entropy effects, which results in an alleviation of saturation magnetization. When increasing the temperature the saturation magnetization decreases; at Curie temperature ($T_c$) it becomes zero and the material becomes paramagnetic. The Curie temperature for $Fe_3O_4$ is 585 ℃.

## 1.4 Magnetic domains and B-H curves

Magnetic domains are the small volume regions with parallel alignment of magnetic dipoles. They exist in any ferromagnetic and ferrimagnetic materials as shown in Figure 1.6. Each domain is magnetized to its saturation magnetization and separated by domain boundaries [4]. Each grain of a polycrystalline specimen may contain more than

one single domain. The magnitude of the magnetization of the entire solid is the vector sum of the magnetizations of all the domains.

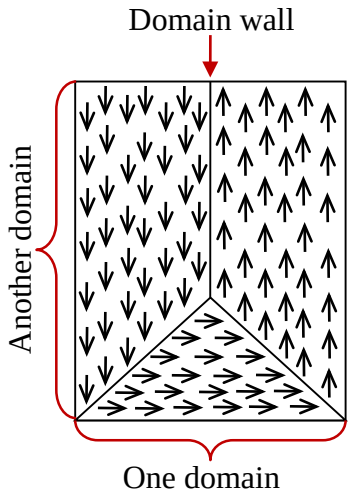


Figure 1.6 Schematic representations of magnetic domains.

For ferromagnetic and ferrimagnetic materials, field intensity $H$ and magnetic flux density $B$ are not proportional to each other. If the material is initially unmagnetized, the variation of $B$ versus $H$ is schematically illustrated in Figure 1.7. The curve begins at the origin. $B$ increases as $H$ increases, first slowly then rapidly. Finally $B$ reaches a plateau and becomes independent of $H$. The maximum value of $B$ is the saturation flux density $B_s$ which corresponds to the saturation magnetization $M_s$. The shape of $B$ versus $H$ profile can be understood by the response of constituent domains of the material to the external field. As $H$ increases, domains change their shape and size by the movement of domain boundaries. Changes of domain structures are illustrated in small circular insets on the profile. Initially domains are randomly oriented that results in no net $B$ or $M$. When $H$ increases the domains which have orientations favorable to the applied field are grown while the others with unfavorable orientations are expended. This process continues until

only the most favorably oriented domains remain. After domain growth is completed, a further increase in the magnetic field causes the domains to rotate and align parallel to the external field. The material reaches the saturation magnetization point and no further change will take place with the increases of the external magnetic field [6].

When the $H$ field is removed or reversed, the curve does not always repeat its original path (Figure 1.8). Instead, $B$ field decreases at a lower rate than $H$ field ($B$ lags behind $H$), which is called hysteresis effect. There is a residual $B$ field when the $H$ field is zero, which is called the remanent flux density $B_r$, so the material remains as magnetized with no external field. As the external field is reversed, $B$ becomes zero at $H_c$ which is called coercivity. Further increasing of $H$ in the reverse direction results in magnetic saturation of the material in opposite direction as indicated by point S'. Reversal of $H$ back to the initial saturation point S completes the symmetric hysteresis loop which yields both a negative remanence ($-B_r$) and a positive coercivity ($+H_c$) [8].

## 1.5 Magnetic particles

Magnetic particles are available in many different sizes and compositions due to their enormous and prevalent usage in medical and biological applications. Commercially available particles typically range from 100 nm to 5–6 μm diameter and most of them consist of small 10–50 nm iron oxide nanocrystals within an organic polymer, typically some type of carbohydrate. Some larger particles in which the carbohydrate is replaced with a plastic or silica, are also available [9]. These polymer- or silica-coated particles are further functionalized with specific components, depending on their applications, such as

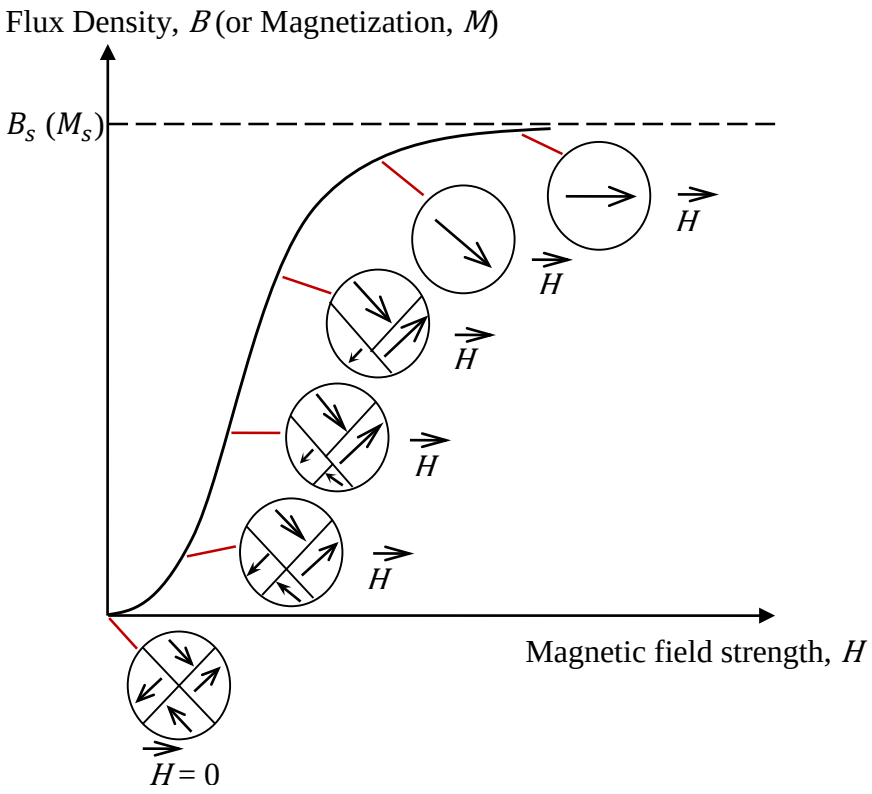


Figure 1.7 Schematic illustration of $B$ versus $H$ curve for initially unmagnetized ferromagnetic and ferrimagnetic materials. At the beginning, the material contains multiple domains. As $H$ increases domains change their shape and size until only the most favorably oriented domains remain. When the domain growth is completed, a further increase in the magnetic field causes the domains to rotate and align parallel with it. The material reaches the point of saturation magnetization.

catalytically active species, specific binding sites, drug molecules or other functional groups [10]. Thus, various biomolecules coated magnetic particles are commercially available nowadays.

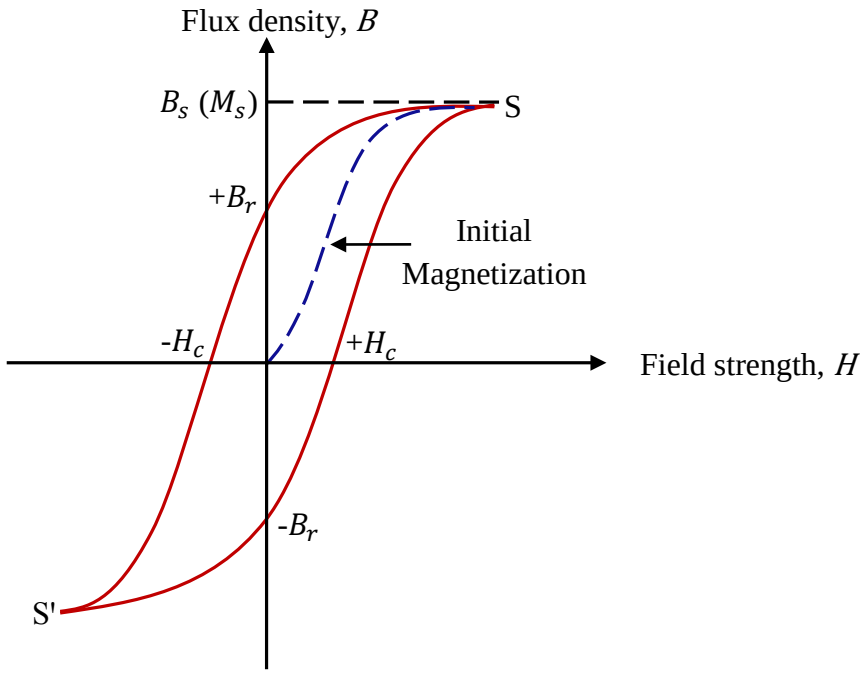


Figure 1.8 Schematic representation of $B-H$ curve for ferromagnetic and ferrimagnetic materials as $H$ variess in both forward and reverse directions.

Many factors, including composition, crystal structure and the size, affect the properties of magnetic particles. In biological applications, particle size plays a major role. Large particles, whose diameters are greater than 1 μm, are used in microbiology for immunomagnetic separation of pathogenic microorganisms, whereas small particles with diameters less than 1 μm are often used in drug delivery, gene delivery and hyperthermia. Therefore it is useful to consider the effect of particle size on the magnetic properties [7].

The particle size is one of the factors that determine the shape of the $B-H$ loop. Large particles (> 1 μm) contain many magnetic domains, which leads to a narrow hysteresis loop. For small particles (< 1 μm), it is energetically favorable to have single domain which leads to a broader hysteresis loop. If the particle size is reduced further (< 20 nm, depending on the material), superparamagnetism arises in which the magnetic moment of the particle is free to fluctuate in response to thermal energy. When particle size decreases, the number of atoms per particle also decreases. This leads to the interaction energy (exchange energy) approaching the thermal energy $k_B T$ at room temperature. As a result, spontaneous random orientation of spins in the particle occurs, thus remanence magnetization or coercitivity becomes zero, which means paramagnetic behavior with no hysteresis. The $B-H$ curve for superparamagnetic particles is shown in Figure 1.9. For example, such a behavior can be observed in < 20 nm iron oxide ($\gamma$-$Fe_2O_3$ or Maghemite) particles and 3 nm pure iron [11].

The magnetic particles used in biomedical applications are either ferromagnetic or ferrimagnetic. Depending on the size, the particles exhibit either a multi-domain, single-domain or superparamagnetic B-H curve. When particles are used for *in vivo* applications, the magnetic response of the blood vessels is negligible compared to the magnetic particles because the blood vessels just have paramagnetic response (from iron containing hemoglobin molecules) and diamagnetic response (from intra vessel proteins). Thus, magnetic signal from particles, regardless of their size, can be detected without interference from the blood vessels [5]. The most-commonly used magnetic particles in biomedical applications are superparamagnetic magnetite ($Fe_3O_4$) and maghemite ($\gamma$-$Fe_2O_3$). This is

due to their biocompatibility (and U.S. Food and Drug Administration approval) and ease of synthesis using physical and chemical approaches [12].

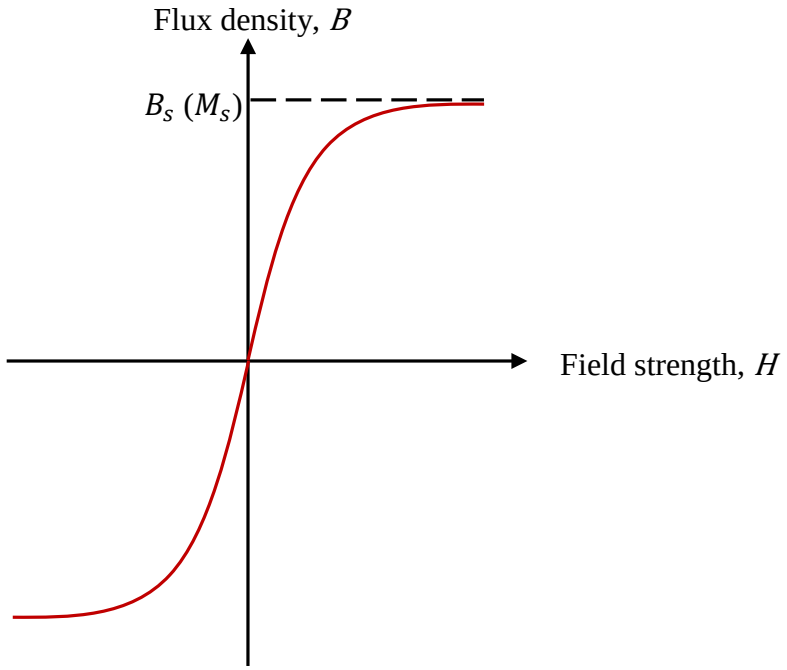


Figure 1.9 Schematic representation of $B-H$ curve for a superparamagnetic material. Compared to the ferromagnetic and ferrimagnetic materials, there is no hysteresis in the curve.

## 1.6 Relaxation of magnetic particles

If the external magnetic field is removed, the net magnetization of magnetic particles will relax. There are two mechanisms for magnetic relaxation. The first one is Néel relaxation in which the internal magnetization vector within the particle returns to the lowest energy state in the direction of the easy axis (the directions minimize the magnetic energy) [Figure 1.10 (a)]. The typical Néel relaxation time is given by the following equation [13].

$$\tau_N = \tau_0 \exp(KV/k_B T) \tag{1.7}$$

The pre-exponential factor is typically $10^{-10}$ – $10^{-12}$ for non-interacting particles and is weakly dependent on the temperature. $K$ is the anisotropy energy density ($K = 2 \times 10^4\ \mathrm{J/m^3}$ for iron oxide) and $V$ is the particle volume. $k_B T$ is the thermal energy where $k_B$ is Boltzmann constant and $T$ is the absolute temperature [11].

The relaxation time of the magnetic particles can be adjusted by changing the size or composition of the particles. Magnetic particles with longer relaxation times (thermally blocked nanoparticles) with stable remanent magnetization have developed to be used as information carriers in magnetic identification and data storage systems [14].

The second relaxation mechanism of magnetic particles is Brownian relaxation, which occurs when particles are suspended in liquids. In this mechanism, the magnetic moment of the particles is relaxed by rotational diffusion of the particles [Figure 1.10 (b)].

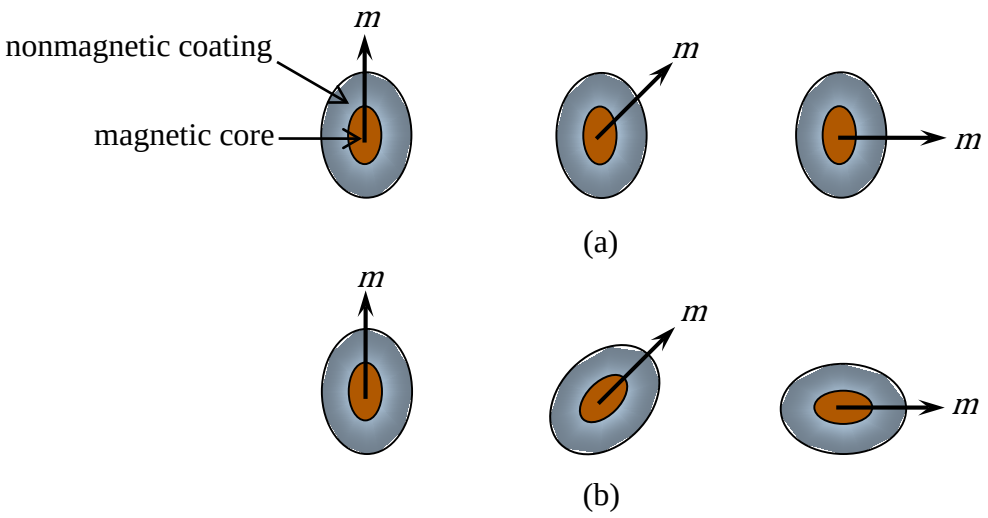


Figure 1.10 Magnetic particle relaxation processes. (a) Néel relaxation by rotation of the magnetic moment of a fixed particle. (b) Brownian relaxation by mechanical rotation of the entire particle.

The Brownian relaxation time is given by the following equation [13].

$$\tau_B = 3V_H\eta/k_BT \tag{1.8}$$

where $V_H$ is hydrodynamic volume of the particles, and $\eta$ is the viscosity of the medium.

Compared to the Néel relaxation where relaxation is governed by the rotation of the magnetic moment within the particles, Brownian relaxation is due to the rotation of the entire particles as shown in Figure 1.10 [15]. Furthermore, Brownian relaxation can take place only in liquids while Néel relaxation does not depend on the dispersion of the particles [16].

## 1.7 Molecular imaging using magnetic particles

The characterization of human diseases by their underlying molecular aberrations is the most powerful tool in molecular medicine. Molecular imaging uses various techniques to visually characterize normal and pathogenic processes at molecular and cellular levels. Typically, the reporting molecules are visualized based on their chemical and biological properties [17].

Many techniques are currently used in molecular imaging. In these techniques, imagine modalities and contrast agents are coupled with molecular specificity. These contrast agents are often called traces or molecular probes that usually consist of two components. The first one is the signaling component which emits a detectable signal and the second one is the targeting component which confers localization. The targeting component may be a peptide, receptor ligand, oligonucleotide, enzyme substrate or antibody. Then the imaging instrument remotely detects this signal with spatial resolution

and sensitivity. The currently used molecular imaging modalities are positron emission tomography (PET), single photon emission computed tomography (SPECT), optical imaging, magnetic resonance imaging (MRI) and ultrasound (US) [18].

PET and SPECT are nuclear-imaging techniques, which use radiolabeled substances as nuclear probes. These probes specifically linked to compounds used by targeted cell. Then the appropriate instruments remotely sense molecular events by detecting radioactive emissions from targeted radionuclides. PET specifically detects positrons. Therefore, positron emitting isotopes are used in PET such as $^{11}C$, $^{13}N$, $^{15}O$, $^{18}F$ and $^{124}I$. In contrast, SPECT detects γ rays in which $^{99m}Tc$, $^{111}In$, $^{123}I$ and $^{131}I$ are used as γ-ray emitters [19]. Optical imaging detects photons emitted from imaging probes by using sensitive CCD cameras. In ultrasound imaging, the image is generated by detection of differential reflection of sound waves. Contrast agents used in ultrasound imaging are capsulated microbubbles, liposomes and perfluorocarbons emulsions [20]. MRI detects signals which generated from proton spin relaxation after the application of a radiofrequency pulse. In MRI probes, paramagnetic agents such as gadolinium and superparamagnetic agents such as iron oxide are commonly used as contrast agents. These agents alter the relaxation time [21].

These various imaging modalities differ in five main aspects: sensitivity, spatial resolution, temporal resolution, penetration depth and cost. Each one has its unique advantages and is often associated with certain disadvantages. For comparison, the characteristics are summarized in Table 1.2.

Superparamagnetic iron oxide nanoparticles are used in MRI as contrast agents for *in vitro* and *in vivo* cellular and molecular imaging. Compared to the paramagnetic contrast

agents of gadolinium chelates, superparamagnetic contrast agents have an advantage of much higher relaxivity, producing an enhanced proton relaxation. Consequently, less amount of agent is needed. Superparamagnetic iron oxide nanoparticles are usually dispersed into a biocompatible and biodegradable carrier prior to their in vivo use [16].

Table 1.2 Comparison of molecular imaging modalities. [17, 21]

| Modality | Sensitivity | Spatial Resolution | Temporal Resolution | Penetration depth | cost |
|---|---|---|---|---|---|
| PET | High | Low | Low | High | High |
| SPECT | Medium | Low | Low | High | Medium |
| Optical imaging | High | Low | High | Low | Low |
| Ultrasound imaging | Medium | Medium | High | Medium | Low |
| MRI | Low | High | High | High | High |

In contrast to the conventional MRI applications that is typically performed in a strong magnetic field (> 1.5 T), we use an ultralow magnetic field technique for molecular and cellular imaging. Our technique is based on the binding force between probe molecules and receptor molecules where the probe molecules are labeled with magnetic particles. The magnetic signal of those particles are detected by atomic magnetometers. This technique is coined as Force-Induced Remnant Magnetization Spectroscopy (FIRMS) in which magnetization of magnetic particles are measured as a function of the binding force between the magnetically labeled probe molecules and the target molecules. A brief description of the technique is presented below [22].

First, receptor molecules are attached to a glass surface, coated with gold, biotin, or other materials. Magnetically labeled ligand molecules are then incubated with those receptor molecules. Next, an external mechanical force is applied to the system to specifically dissociate the bound ligand molecules from receptors. The magnetization of the magnetic particles, which bound to the ligand molecules, is measured by atomic magnetometer after each force step. A schematic representation of FIRMS technique is shown in Figure 1.11.

The force from a shaker, centrifuge or sonicator can be applied on magnetic particles as the external force. At the beginning, magnetization of the particles remains nearly constant when the force is increasing. At the point $F_p$ (Figure 1.11), magnetization decreases due to the dissociation of physisorbed (non-specifically bound) molecules. Detached particles do not contribute to the magnetization because they undergo Brownian motion, which randomizes the magnetic dipole of the particles. Thus, only the remaining specifically bound molecules contribute to the magnetization. Further increasing of the force causes the magnetization to become zero at point $F_s$ due to the dissociation of the specifically bound molecules. In order to determine the exact position of the dissociation force, the derivative of the magnetization verses force graph is plotted (the bottom one). This derivative plot is termed as a FIRM spectrum. The FIRMS technique allows for distinguishing specifically bound molecules from physisorbed ones as well as resolving different types of specifically bound molecules in the same system [23].

Compared to the other molecular imaging modalities, the probe or contrast agent for our technique is magnetically labeled ligand molecules. The signaling component is the

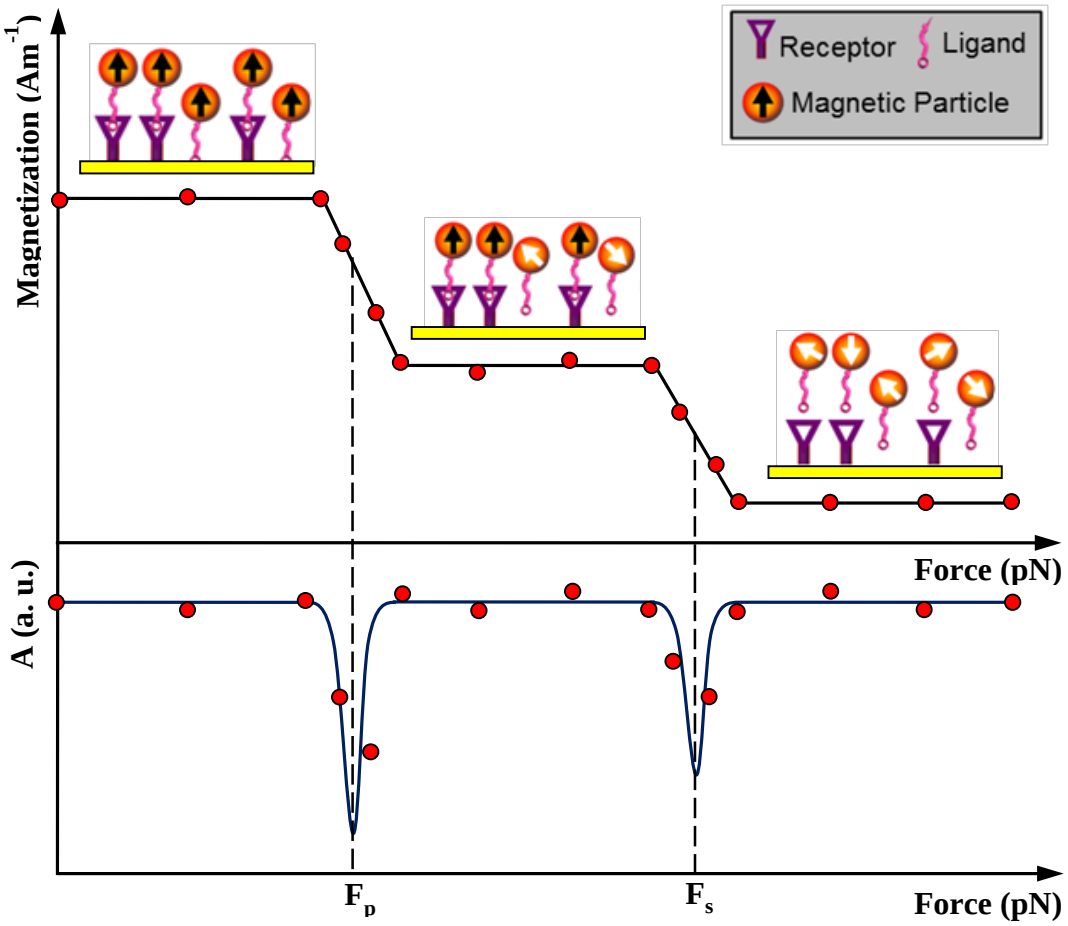


Figure 1.11 Schematic representation of the FIRMS technique. Top, the magnetic signal profile as a function of the amplitude of an external force. Bottom, the derivative of the profile in the top panel.

magnetic particles, and the targeting component is ligand molecules which are specifically bound to the receptor molecules. The imaging instrument is an atomic magnetometer.

In addition to the molecular imaging, our technique provides more useful information regarding dissociation forces of biomolecules. For example, we can provide very high force resolution that is sufficient to distinguish DNA duplexes which have single base pair difference. Thus, our technique is suitable for characterization of non-covalent bonds. Non-covalent bonding is important in biology because it holds the two strands of the DNA double helix together, folds polypeptides into secondary structures, enables enzymes to bind to their substrates, enables antibodies to bind to their antigens, enables proteins to bind to their receptors and permits the assembly of such macromolecular machinery as ribosomes. Therefore, the determination of non-covalent bonding strength of biological molecules contributes to a better understanding of the mechanics of biomolecules [24]. Compared to the well-established force techniques, mainly atomic force microscopy (AFM) and optical tweezers, FIRMS provides higher force resolution and measures a large number of non-covalent bonds at the same time. Therefore, it is more suited for practical applications in molecular imaging. In addition, the noninvasiveness of our detection allows a unique rebinding method to confirm the dissociated non-covalent bonds, which will be discussed in Chapter 3.

## 1.8 Detection of magnetic particles

The versatile usage of nanometer- and micrometer-sized magnetic particles in many biological applications requires a sensitive detection method. Many techniques have been

developed for detecting weak magnetic fields such as giant magnetoresistive (GMR) sensors, superconducting quantum interference devices (SQUIDs), atomic magnetometers, and recently nitrogen-vacancy (NV) diamond magnetometers.

Each technique has its own advantages and disadvantages. For example, GMR sensors are cheap and convenient to use but they require the sample to be very close to the sensor, on the order of micrometers. SQUIDs have ultrahigh sensitivity in detecting weak magnetic fields but they require cryogenics [25]. NV diamond magnetometers are the newest technique for magnetic field detection. However, their sensitivity is still several orders of magnitude worse than that of SQUIDs or atomic magnetometers [26]. Atomic magnetometers offer high sensitivity that is comparable to SQUIDs, but does not require cryogenics [25]. For instance, spin exchange relaxation-free (SERF) atomic magnetometers have reached the sensitivity of $aT/\sqrt{Hz}$ level at an operating temperature of 160 °C [27]. The work presented in this dissertation has used atomic magnetometers for magnetic particle detection. Atomic magnetometers measure the intensity or polarization change of a laser beam after it interacts with spin-polarized alkali atoms in the presence of a magnetic field [28]. Chapter 2 of this dissertation explains the basic principles and instrumentation of atomic magnetometry.

# Chapter 2

# Atomic Magnetometry

This chapter provides the basic principle of atomic magnetometry, which is based on the magneto-optical effects in the presence of an external magnetic field. We will also discuss the sensitivity of atomic magnetometry, instrumentation of our Cs-based atomic magnetometer, and scanning of magnetic particles using our instrument.

## 2.1 Linear magneto-optical rotation

### 2.1.1 The Faraday effect

In 1845, Michael Faraday discovered the interaction between light and a magnetic field in a medium. This interaction is named as Faraday rotation or Faraday effect, which describes the rotation of the polarization plane of linearly polarized light when the light propagates through a material sample in a longitudinal magnetic field which is applied along the light propagation direction as shown in Figure 2.1 [29-31]. If the applied magnetic field is perpendicular to the medium, the interaction phenomenon is called the Voigt effect (in gases) or the Cotton-Mouton effect (in liquids) [32].

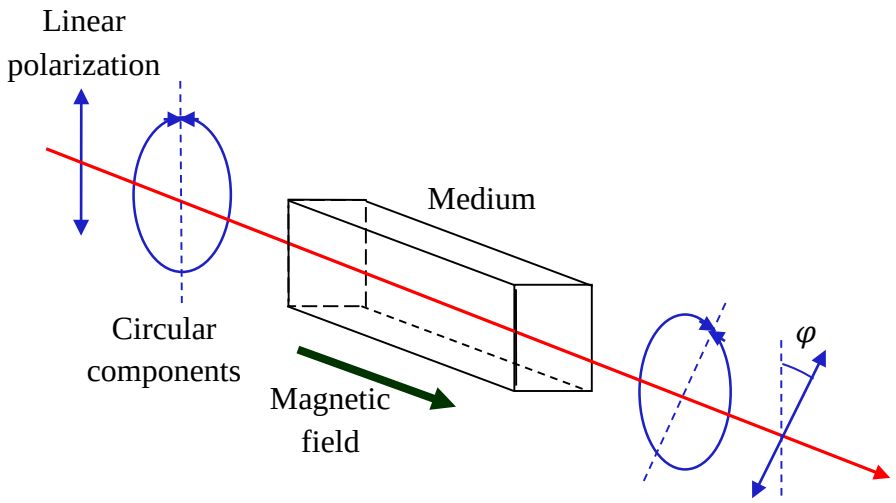


Figure 2.1 General scheme for linear magneto optical rotation of light.

Faraday observed that the rotation angle $\varphi$ is proportional to the magnetic field intensity $B$ and to the propagating distance $l$ of the active medium. The proportionality

coefficient is named as Verdet constant $V$, which describes mediums' ability to rotate the polarization plane [33].

$$\varphi = VlB \tag{2.1}$$

The physical origin of the magneto-optical rotation is the difference in the refractive indices of left- and right- circularly components of polarized light in the medium induced by the applied magnetic field. Linearly polarized light can be expressed as a superposition of two circularly polarized (left and right) components. The representation of the light can be transformed from circular into the Cartesian basis by the following equations.

$$\hat{e}_x = \frac{1}{\sqrt{2}} (\hat{e}_+ + \hat{e}_-) \tag{2.2}$$

$$\hat{e}_y = \frac{-i}{\sqrt{2}} (\hat{e}_+ - \hat{e}_-) \tag{2.3}$$

where $\hat{e}_x$ and $\hat{e}_y$ are the unit vectors representing light linearly polarized along *x* and *y* directions, respectively. $\hat{e}_+$ and $\hat{e}_-$ are the unit vectors representing right and left circularly polarized light, respectively.

Suppose the light is linearly polarized in *y* direction and wave vector **k** propagates along the *z*. Then the electric field ***E*** of light waves can be written as

$$E = E_0 \hat{e}_y \cos(kz - \omega t) = \frac{-iE_0}{2\sqrt{2}} \left[\hat{e}_+ e^{-i(kz-\omega t)} - \hat{e}_- e^{-i(kz-\omega t)}\right] + c.c., \tag{2.4}$$

where $E_0$ is the amplitude of the electric field, $\omega$ is the frequency of the light and $c.c.$ indicates the complex conjugate. The wavenumber $k$ is given by

$$k = \frac{2\pi}{\lambda} = \frac{\eta\omega}{c} \tag{2.5}$$

where $\lambda$ is the wave length of the light and $\eta$ is the complex refractive index. $\eta$ is given by the equation

$$\eta = n + i\kappa. \tag{2.6}$$

The real part of the complex refractive index is the refractive index $n$, which characterizes the dispersion of a medium, while the imaginary part is absorption coefficient $\kappa$, which describes the light absorption ability.

If the refractive indices of two circular components are different ($n_+ \neq n_-$), each component travels in the medium with different velocity which leads to a phase shift of

$$\phi = \frac{\omega l}{c} (n_+ - n_-) \tag{2.7}$$

This phase shift $\phi$ causes to rotation of the polarization plane by angle $\varphi$

$$\varphi = \frac{\phi}{2} \tag{2.8}$$

In Faraday rotation, the change of refractive indices is induced by the applied magnetic field.

The physical origin of the difference in refractive indices was unknown until more than 50 years after Faraday's discovery. Italian Physicists Domenico Macaluso and Orso Corbino brought some insight into this problem by their studies of light absorption spectra of alkali atoms (sodium vapor) in the presence of a magnetic field. Their observation of magneto-optical rotation of alkali atoms leads to the Macaluso-Corbino effect.

According to the equation 2.1, Verdet constant V indicates the magnitude of optical rotation of a material per unit magnetic field and unit length. Compared to the dense flint glasses which have typical $V \simeq 3 \times 10^{-1}$ radT$^{-1}$cm$^{-1}$ (Faraday used lead glass in his

experiment), alkali atoms have very high values of Verdet constants. For example, Rubidium atoms with $3 \times 10^9$ $cm^{-3}$ vapor density has the value of $V \simeq 10^8$ $radT^{-1}cm^{-1}$. Due to the difference of density between glass and rarified atomic vapor, the later can be considered as $10^{20}$ greater rotation "per atom" than the heavy flint [34].

### 2.1.2 Macaluso-Corbino effect

Macaluso and Corbino observed the Faraday rotation of gaseous alkali atoms in their experiments. They used the same experimental setup as Faraday's except that their source of light was the sun and their medium was sodium atomic vapor. They also used a diffraction grating in order to select specific frequencies of sunlight. Macaluso and Corbino observed that the magneto-optical rotation of the light was enhanced when the frequency of the incident light was tuned near an atomic resonance frequency in sodium [35, 36].

The experimental work of Faraday, Macaluso and Corbino, in addition with Pieter Zeeman's discovery of the splitting of atomic spectral lines in magnetic field, led Woldemer Voigt to explain the magneto-optical rotation as follows [37,38]. The shifting of the spectral lines in the magnetic field caused a difference in refractive indices for the circular components of the linearly polarized light; consequently, optical rotation is observed. This linear near-resonance Faraday effect is known as the Macaluso-Corbino effect.

Macaluso-Corbino effect can be understood by considering the simplest case of $F = 0 \rightarrow F' = 0$ transition, where $F$, $F'$ denote the total angular momenta of the ground and excited states, respectively (Figure 2.2). The linearly polarized light can be considered as a combination of two counter-rotating components of right circular ($\sigma^+$) and left circular

($\sigma^-$) polarized light with respective $\Delta M = \pm 1$ selection rules, where $M$ is the magnetic quantum number related to $F$. In the absence of a magnetic field, the ground-state sublevels are degenerate and resonance frequencies of $\sigma^+$ and $\sigma^-$ are same. So both components has the same refractive index.

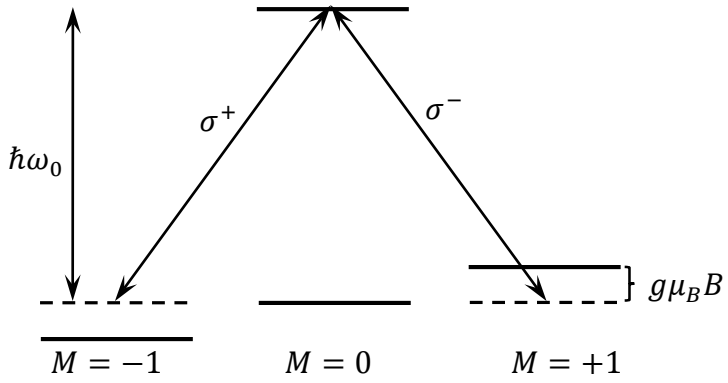


Figure 2.2 Illustration of energy level diagram for an $F = 0 \rightarrow F' = 0$ atomic transition. In the presence of a magnetic field, the Zeeman sublevels are shifted by $\pm\, g\mu_B BM$, changing the resonance frequencies of right- and left- circular polarized light.

If a magnetic field is applied, the Zeeman sublevels $M = \pm 1$ shift in energy by an amount of $\pm\, g\mu_B B$ , where $g$ is the Landé factor, $\mu_B$ is the Bohr magneton and $B$ is the applied field. The different components of the linearly polarized light couple to different ground state Zeeman sublevels, resulting in a difference between the resonance frequencies for the two circular components. Thus Zeeman splitting creates a difference in refractive indices for circular components to lead optical rotation of plane polarized light by an angle

$$\varphi = \pi(n_+ - n_-)\frac{l}{\lambda} \tag{2.9}$$

where $l$ is the length of the medium traversed and $\lambda$ is the wavelength of the light.

For monochromatic light at resonance the optical rotation can be estimated as a function of $B$ by the following equation.

$$\varphi \simeq \frac{2g\mu_B B/\hbar\Gamma}{1+(2g\mu_B B/\hbar\Gamma)^2}\cdot\frac{l}{l_0} \tag{2.10}$$

where Γ is the Doppler width of the absorption line and $l_0$ is the absorption length in the medium. The dependence of $\varphi$ on $B$ has a characteristic dispersion-like shape. $\varphi$ is linear with respect to $B$ at small values of $B$, peaks at $2g\mu_B B \approx \hbar\Gamma$ and falls off at larger fields [39].

Atoms with non-zero nuclear spins show linear magneto-optical rotation due to the mixing of different hyperfine components (in particular states of the same $M$ but different $F$) induced by a magnetic field [40-42]. In many practical situations, the contribution of this mechanism (hyperfine-mixing effect) is comparable to the above Zeeman sublevels shifting effect (level-shifting effect) [43]. For example, linear magneto-optical rotation of alkali atoms at near the resonance frequency. The rotation angle due to hyperfine-mixing effect can be estimated as

$$\varphi \simeq \frac{g\mu_B B}{\Delta_{hfs}}\cdot\frac{l}{l_0} \tag{2.11}$$

where $\Delta_{hfs}$ is the separation between the hyperfine levels. Unlike the level-shifting effect, it only leads to a change in magnitude of refractive indices ($n_+$ and $n_-$) and not the resonance frequencies. The spectral rotation profile is dispersion-like curves around the hyperfine components of the transition.

According to Boltzmann distribution, the populations of the ground state Zeeman sublevels that are split by the magnetic field are different. This causes a different refractive

indices for light polarization components thus leading to linear magneto-optical rotation. This effect is known as paramagnetic effect, which is relatively small for gaseous media compared to the level-shifting effect and hyperfine-mixing effect. However, it can be enhanced by optical pumping, which creates a non-equilibrium population distribution of Zeeman sublevels. Optical pumping is the mechanism in the nonlinear version of magneto-optical rotation that used to detect ultra-low magnetic fields.

Magnetic signals generated from the magnetic particles are very small (typically in pico-Tesla range). Therefore, very sensitive magnetometers are required to detect such signals. Linear magneto-optical rotation is not sensitive enough for detecting very low magnetic fields, because their optical rotation widths are hundreds of gauss and rotation angles are extremely small at very low magnetic fields (Figure 2.3). Therefore narrow optical rotation widths are required for higher sensitivity. Nonlinear magneto-optical effects resolve this problem, which create ultra-narrow optical rotation widths and allow to detect ultra-low magnetic fields. Figure 2.3 shows the comparison of optical rotation widths of linear and nonlinear magneto-optical rotations.

## 2.2 Nonlinear magneto-optical rotation

### 2.2.1 Nonlinear optical effects

A nonlinear optical effect is a process in which the optical properties of a medium depend on the light field itself. So it concerns the medium's susceptibility to light and the ability of the light to change the properties of the medium. It is useful to consider a nonlinear

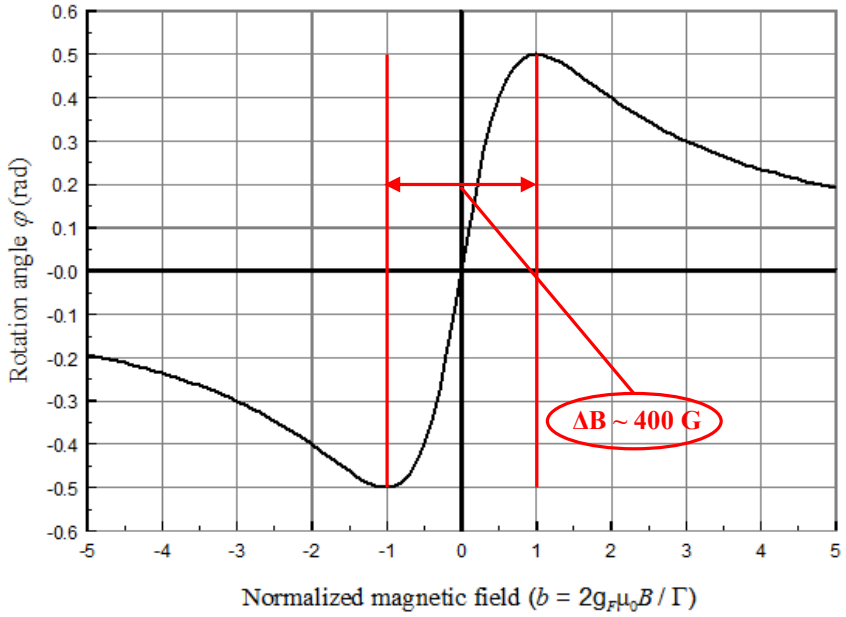


(a) Linear optical rotation

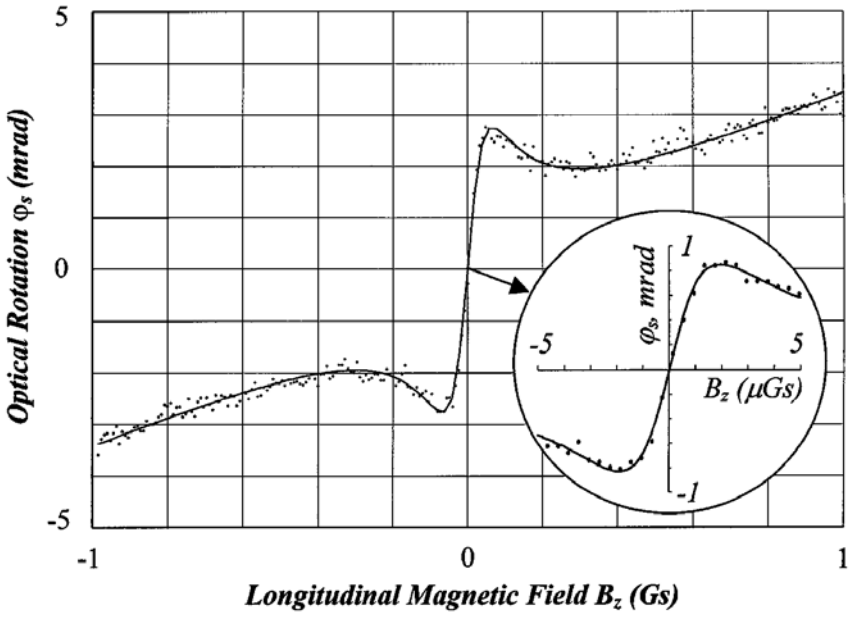


(b) Nonlinear optical rotation

Figure 2.3 Comparison of linear and nonlinear magneto-optical rotation widths. The drastic narrowing of the optical rotation can be seen in nonlinear optical effects. Figures are taken from [44] and [45] respectively.

effect as three-stage processes of pumping, evolution and probing. At the first stage (pumping), light field modifies the optical properties of medium. During the second stage (evolution) the medium evolves and so do its optical properties, while evolving the medium can be subject to an interaction with the other fields such as magnetic fields. In last stage (probing), medium changes the properties of the propagating light. In many cases, these three stages may be simultaneous. The light used to interact with the medium may be a single beam or multiple beams. When a single beam is used, which both modifies the medium and probes its properties. In multiple beam arrangements, separate beams are used for pumping and probing.

Generally nonlinear effects are associated with high light intensities and it is important to realize that the degree of the nonlinear effect strongly depends on not only the specific mechanism of atomic saturation by the light but also the relaxation rate of atomic polarization. So it is useful to introduce saturation parameters which are commonly applied for all nonlinear optical process near resonance.

### 2.2.2 Saturation parameters

The degree of saturation of a transition is characterized by a saturation parameter, which is the ratio of the rates of coherent light atom interactions and incoherent relaxation processes such as spontaneous decay [46]. The saturation parameter can be generally expressed by,

$$\kappa = \frac{excitation\ rate}{relaxation\ rate} \tag{2.12}$$

Consider a two level system with ground state and the excited state [Figure 2.4 (a)] where light is tuned to resonance, the upper state decays back to the lower state and the saturation parameter is given by

$$\kappa_1 = \frac{\Gamma_{pump}}{\gamma_0} = \frac{d^2\varepsilon_0^2}{\gamma_0^2}. \tag{2.13}$$

where $d$ is the transition dipole moment, $\varepsilon_0$ is the amplitude of the electric field and $\gamma_0$ is the homogeneous width of the transition. In this equation, excitation rate $\Gamma_{pump} = d^2\varepsilon_0^2/\gamma_0$ and relaxation rate is $\gamma_0$ [46].

When $\kappa_1 \ll 1$, the spontaneous emission dominates and the lower sublevels are mostly populated. When $\kappa_1 \gg 1$, atoms undergo cyclical absorption and emission of photons (Rabi oscillations) at a rate much faster than spontaneous emission, and the average population of the upper and the lower states become equal.

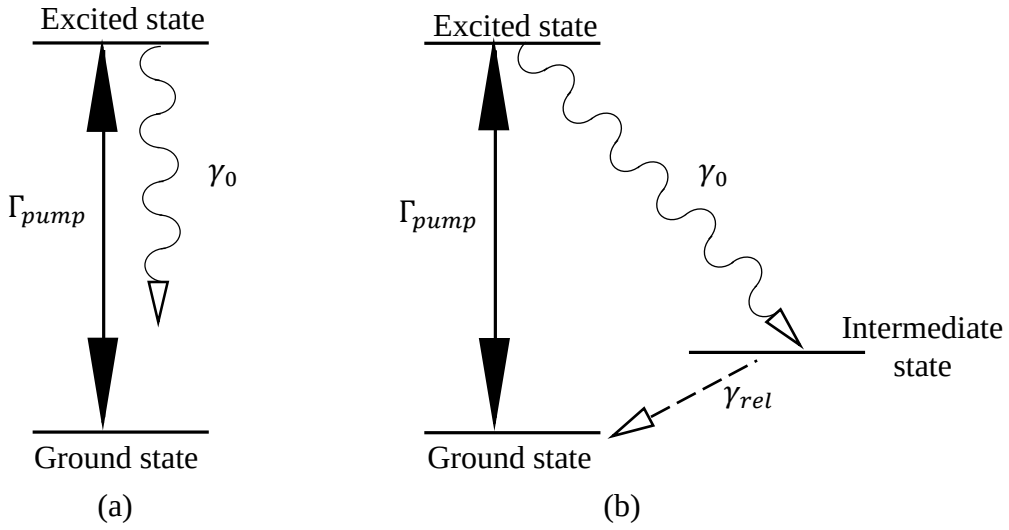


Figure 2.4 Energy level diagrams (a) for a two level system in which the excited state spontaneously decays back to the ground state with rate $\gamma_0$ and (b) for a three level system in which the excited state spontaneously decays to an intermediate state with rate $\gamma_0$. Atoms

in both systems are resonantly excited from the ground state to the excited state at the rate $\Gamma_{pump}$.

If the upper level predominantly decays to some other intermediate state other than the lower state (Figure 2.4 b), the saturation parameter is given by the following equation.

$$\kappa_2 = \frac{\Gamma_{pump}}{\gamma_{rel}} = \frac{d^2 \varepsilon_0^2}{\gamma_0 \gamma_{rel}}. \tag{2.14}$$

where $\gamma_{rel}$ is the relaxation rate from intermediate state to lower state.

The relevant saturation parameters for the nonlinear effects associated with Zeeman sublevels depend on the specifics of the transitions and the external fields. For example, if a "dark" state (described under next topic) is present in the lower state, the saturation parameter $\kappa_2$ applies. As another example, $F = 1/2 \rightarrow F' = 1/2$ transition pumped with linearly polarized light has no dark state and the saturation parameter $\kappa_1$ applies.

In order to achieve nonlinear condition optical pumping is required, which creates a population distribution among Zeeman sublevels and leads to generate bright and dark states on those sublevels.

### 2.2.3 Optical pumping, dark and bright states

Optical pumping is the process which redistributes the population of Zeeman sublevels occupied by a collection of atoms by using photons. An isolated collection of atoms in the form of a gas will occupy their available energy levels at a given temperature, which is referred to as the thermal equilibrium distribution. But the distribution of the atoms among these energy levels can be radically altered by the application of resonant light. Thus optical pumping redistributes the population of Zeeman sublevels and creates

coherences between the Zeeman sublevels (creating a medium of polarized atoms). Now the atomic medium becomes optically anisotropic.

Optical pumping can be easily understood by considering the interaction of circularly polarized light with two level system (Figure 2.5) in the limit of large $\kappa$ ($\kappa = \kappa_2$). Here it is assumed that the atoms excited to the upper level can only decay back to the lower level ("closed transitions") and the light used for the excitation is on resonance.

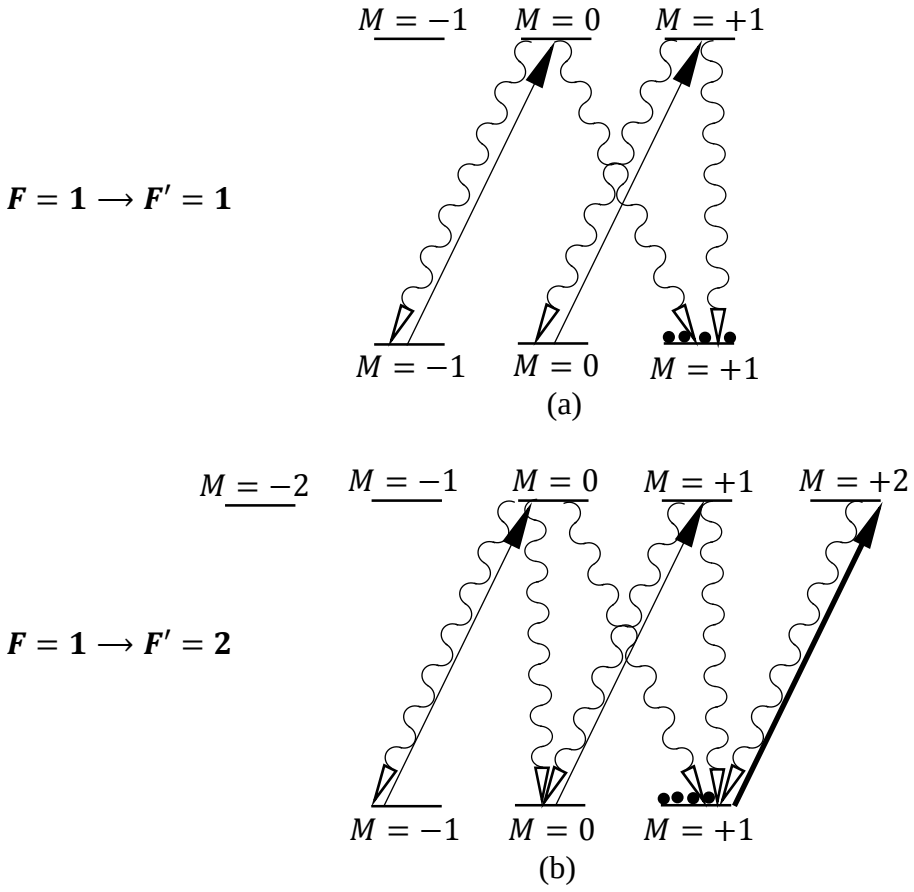


Figure 2.5 Schematic representation of the effects of optical pumping with circularly polarized light component $\sigma^+$ on the populations of ground state Zeeman sublevels in the case of (a) $F = 1 \rightarrow F' = 1$ and (b) $F = 1 \rightarrow F' = 2$ transitions.

As we have seen in Section 2.1.2, $\sigma^+$ component of the polarized light couples the $M$ sublevel in the ground state to the $M+1$ sublevel in the excited state. In quantum mechanics, a state is represented by $|F, M>$ notation. Thus $\sigma^+$ light will couple the $|F, M>$ state to the $|F, M+1>$ state [46].

Figure 2.5 shows the transitions of $F=1 \rightarrow F'=1$ and $=1 \rightarrow F'=2$. For the $F=1 \rightarrow F'=1$ case, optical pumping causes increasing of the population in the $M=+1$ state but depleting the $M=0$ and $M=-1$ states in the lower level. Thus the atoms end up in the state that does not absorb light, which is called a dark state. A sample of atoms that do not absorb light photons is called transparent medium.

The opposite can be seen in the $F=1 \rightarrow F'=2$ case, where the atoms end up in the state that does absorb light, which is called a bright state. In this case, absorption increases as a result of optical pumping.

Similar results could be seen for the interaction of linearly polarized light with the system. Although a qualitative picture of optical pumping is presented here, it should be noted that the generation of the dark and bright states can be derived mathematically with the aid of relative transition probabilities, which use Clebsch-Gordon coefficients. We believe that such a kind of work is beyond the limit of this dissertation because the work presented here focuses on the applications of nonlinear magneto-optical rotation in detecting magnetic fields.

#### 2.2.3.1 Optical pumping of cesium vapor

We use cesium atomic medium in nonlinear magneto optical rotation. Compared to the above two-level system, the splitting of Zeeman sub levels in the case of cesium is more

complicated. Cesium is a Group I element, which has the electron configuration of [Xe]6s[1] with total electronic angular momentum of $J = 1/2$. The stable isotope $^{133}$Cs, which is used in magnetometry applications, has a nuclear spin $I = 7/2$. The $6S_{1/2}$ ground state splits by the hyperfine interactions into the two hyperfine levels $F = |I \pm J| = 3{,}4$ as shown in Figure 2.6.

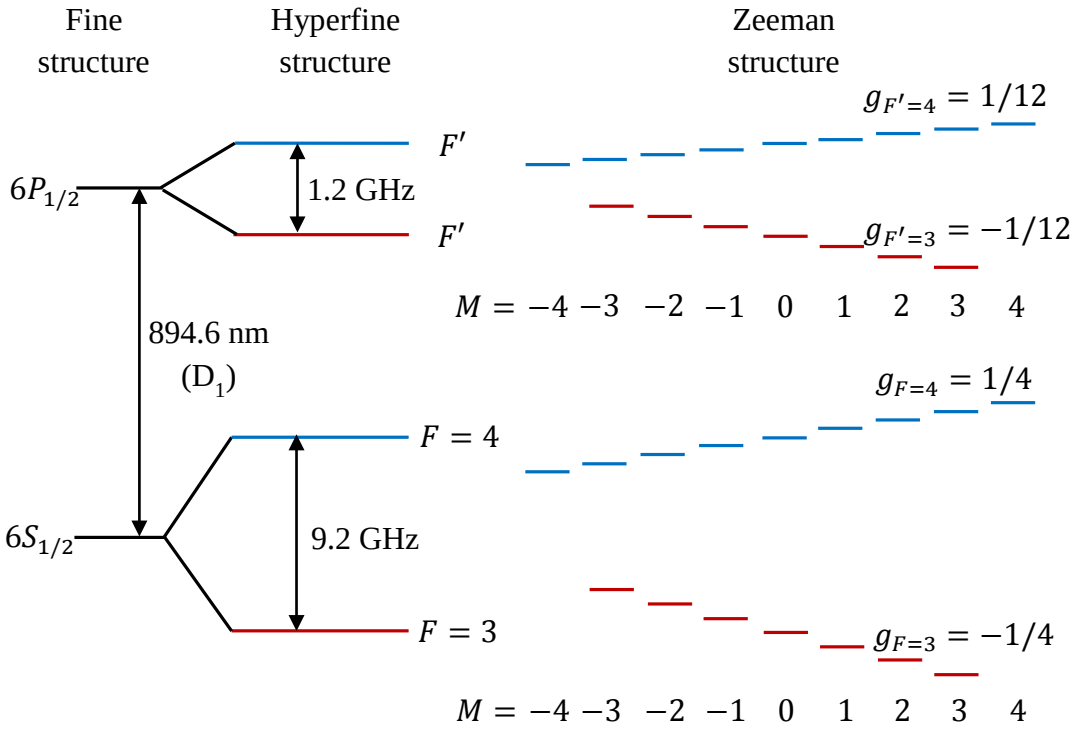


Figure 2.6 Energy level diagram of $Cs^{133}$. $D_1$ transition with hyperfine structure resulted by interaction of electronic states with nuclear spin of $Cs^{133}$ (left). Splitting of Zeeman sublevels in the presence of a magnetic field (right). Due to the different signs of $g$-factors ($g_{F=3}$ and $g_{F=3}$) the energy shifts also have opposite sign.

The energy difference between the two hyperfine states is 9.2 GHz. By using the D1 transition in the near infrared (894.6 nm), the atoms can be excited to the lowest excited

state, $6P_{1/2}$, which splits into the hyperfine levels $F' = 3,4$ separated by 1.2 GHz. Each hyperfine level $F$ consists of $2F + 1$ degenerate magnetic sublevels. When a magnetic field is applied, energies of Zeeman sublevels are shifted by $\pm\, g\mu_B BM$, which is represented by Zeeman structure in Figure 2.6.

Compared to the thermal energy of atoms ($\approx 10^4$ GHz) at room temperature, the energy difference between the two ground state hyperfine levels in Cs ($\approx$ 9 GHz) is much smaller so that all 16 sublevels are equally populated. In order to observe nonlinear magneto-optical rotation, a population imbalance of these sublevels should be created by optical pumping. A tunable laser with wavelength of 894.6 nm (corresponding to the $D_1$ transition) is used for this purpose which excites a single hyperfine transition of $6S_{1/2}, F \rightarrow 6P_{1/2}, F'$.

Consider a right-circularly polarized ($\sigma^+$) light beam which is resonant with the $F = 4 \rightarrow F' = 3$ hyperfine transition of $D_1$ line, irradiating a sample of Cs atoms. $\sigma^+$ light couples the $|4, M>$ state to the $|3, M+1>$ state as shown in the Figure 2.6. (c). The excited atoms spontaneously decays to a ground state levels by generating dark states. These transitions obey the selections rules of $\Delta F = 0, \pm 1$ and $\Delta M = 0, \pm 1$ (excluding $\Delta F = 0, |F', M = 0> \rightarrow |F, M = 0>$). The lifetime of the excited state $6P_{1/2}$ is about 30 ns. The possible decay channels for the state $6P_{1/2}$ $|F = 3, M = -1>$ are shown in Figure 2.7 [47].

The inset represents the relative population distributions of the Zeeman sublevels. Thus Cs atoms can be selectively polarized via optical pumping. In our experiments, we use linearly polarized light for optical pumping.

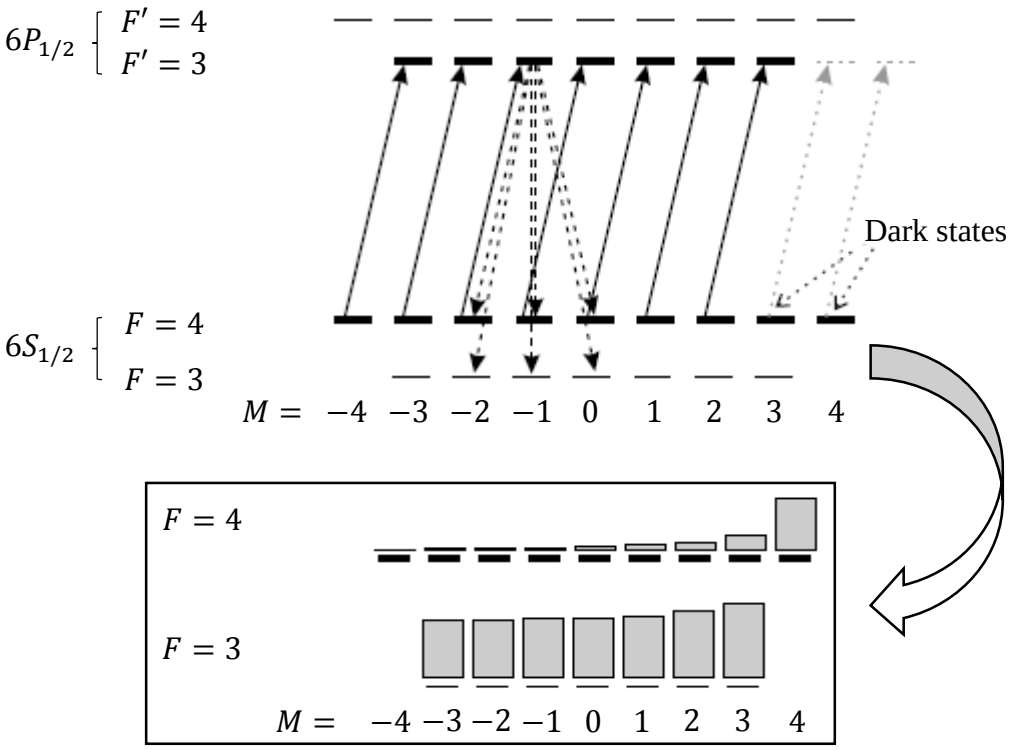


Figure 2.7 Optical pumping of Cs atoms by right circularly polarized light. The inset shows the population distribution of two ground state Zeeman sublevels. The figure is taken from Ref. [47].

## 2.2.4 Nonlinear magneto-optical rotation

Nonlinear magneto-optical rotation (NMOR) is a typical nonlinear optical effect. NMOR is a light intensity dependent rotation of the polarization plane of linearly polarized light when the light propagates through a medium placed in a magnetic field. The first measurement of this kind of work were performed by W. Gawlik *et al*. in 1974 [48]. They discovered that the dependence of the rotation angle on the magnetic field is more complex for intense light sources than weak light, and observed very narrow features close to zero magnetic field ($B = 0$). The rotation angle associated with these narrow signals were dependent on the light intensity. These results were the first observation of NMOR.

### 2.2.4.1 Different contributions to NMOR

Compared to the linear magneto-optical rotation, NMOR has ultra-narrow optical rotation widths. The two processes that are responsible for this enhanced rotation are: (1) Bennett-structure effect – the formation of Bennett structures in the atomic velocity distribution due to optical pumping and (2) the coherent effects - evolution of light-induced atomic polarization in the magnetic field. The primary difference between these two effects is the magnitude of the magnetic field $B_{max}$ at which optical rotation reaches maximum and $B_{max}$ is given by

$$B_{max} = \frac{\hbar\Gamma}{2g\mu_B}. \tag{2.15}$$

where Γ is the line width. For Bennett-structure effect, the smallest obtainable line width is corresponds to the natural width of the atomic transition (~ 2π × 1-10 MHz). For

coherence effects, the line width depends on the rate of relaxation of atomic polarization and the smallest one has found is ~ $2\pi \times 1$ Hz for antirelaxation-coated vapor cell [34].

#### 2.2.4.1.1 Bennett-structure effect

When light interacts with an atomic medium via optical pumping, atoms absorb light energy. This depletes their ground state atomic velocity distribution at a certain velocity group and creates a "hole" in the velocity distribution. This redistributed atomic population changes the properties of the medium where sub-Doppler features arise in the refractive indices of $n_+$ and $n_-$ of circular polarized components. In the presence of a magnetic field, the refractive indices $n_+$ and $n_-$ are displaced relative to each other (Figure 2.8) due to the Zeeman shift, resulting in optical rotation of the polarization plane [38].

The enhanced optical rotation compared to linear effect is the feature in refractive indices due to "holes" in velocity distribution. In the absence of the Bennett structure (holes), this gives the linear Faraday effect. The resultant optical rotation due to Bennett holes can be considered as rotation produced by linear Faraday rotation minus that would have been produced by the pumped out atoms. So the rotation due to Bennett holes has opposite sign compared to the liner Faraday rotation.

#### 2.2.4.1.2 Coherent effects

Further narrowing of the optical rotation width arises due to coherence effects in the ground state Zeeman sublevels. Barkov et al [50] observed that the coherent effects caused to enhance the optical rotation by ~ $10^4$ times larger than that due to the linear

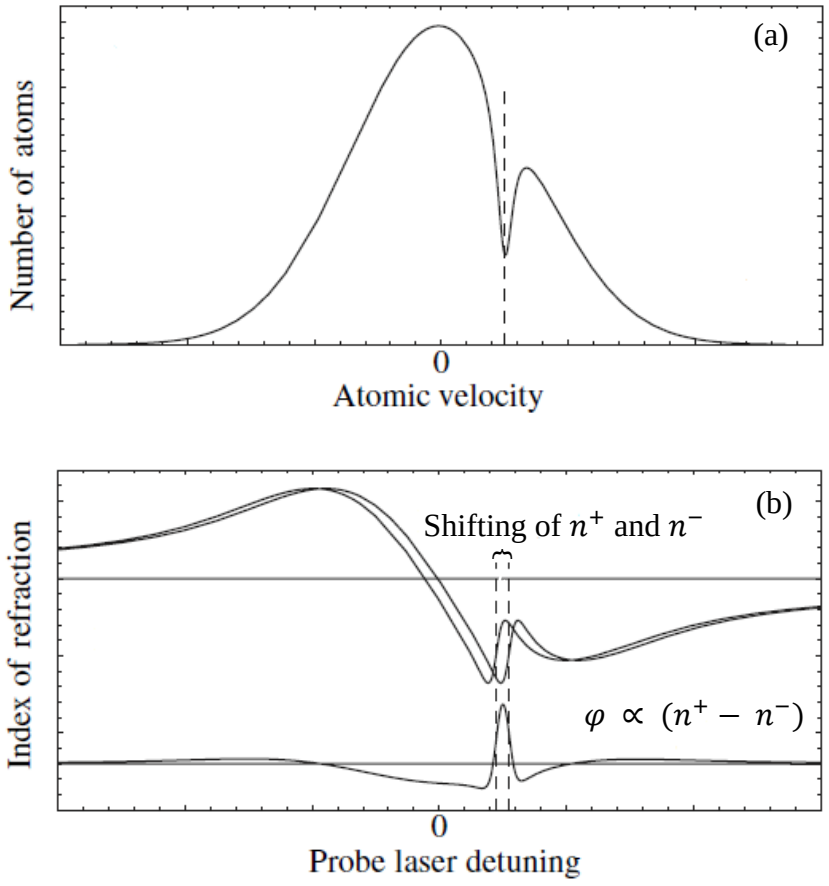


Figure 2.8 Bennett structure effect in NMOR (For $F = 1/2 \rightarrow F' = 1/2$ transition with linearly polarized light). (a) Formation of Bennett holes in the atomic velocity distribution via optical pumping. (b). Shifting of refractive indices $n^+$ and $n^-$ relative to each other (real part of refractive indices are shown) in the presence of a magnetic field (upper trace). NMOR feature due to Bennett holes where rotation angle is proportional to the difference between $n^+$ and $n^-$(Lower trace). The figure is taken from Ref. [49].

Macaluso-Corbino effect. So it's useful to discuss the generation and the evolution of the ground state coherences.

Coherent effects can be considered as a three stage process as described in the Section 2.2.1. But all these processes may occur simultaneously and continuously. The first one is the generation of polarized atoms via optical pumping, the second one is the evolution of atomic polarization such as Larmor precession, and the last one is the probing of atoms cause change in properties of propagating light.

Consider initially unpolarized atoms with total angular momentum $F = 1$. Suppose these atoms are subject to a linearly polarized light with frequency corresponding to a transition to a $F' = 0$ state. Initially, atoms can be considered as an incoherent mixture of the following states.

$$|z> = |M = 0> \tag{2.16}$$

$$|x> = \frac{1}{\sqrt{2}} (|M = +1> - |M = -1>) \tag{2.17}$$

$$|y> = \frac{1}{\sqrt{2}} (|M = +1> + |M = -1>) \tag{2.18}$$

The $|z>$ state can only be excited to $F' = 0$ by $z$-polarized light and it is decoupled from $x$- and $y$- polarized light. Similarly, the other two states $|x>$, $|y>$ can only absorb $x$- and $y$- polarized light. These two states are coherent superposition of Zeeman sublevels.

Suppose the $x$-polarized laser light is used for optical pumping. This causes depletion of $x$-absorbing state, leaving the $y$- and $z$- states as dark states. The medium is now transparent to $x$-polarized light but can still absorb and refract orthogonal polarized

light. Thus the medium becomes linearly dichroic (absorption of light is dependent on polarization), much like a linear polarizer. The atoms are now in an aligned state and has an axis of alignment. The atomic moments of atoms are oriented with respect to this axis of alignment. In the presence of a magnetic field, the aligned atomic moments experience a torque and precess around the axis of the magnetic field at Larmor frequency. This rotates the medium's axis of linear dichroism, which is observed as a rotation of propagating light with respect to the initial light polarization.

Visualization of atomic polarization is a very useful tool. It describes NMOR in an intuitive way. Generally atomic polarization is visualized by drawing a surface in three dimensions representing the probability distribution of the angular momentum. In order to visualize the angular momentum state of atoms with total angular momentum $F$, a surface is drawn whose distance from the origin is equal to the probability of finding the projection $M = F$ [51]. Presenting a complete three-dimensional surface of atomic polarizations is beyond the limit of this dissertation. However, Figure 2.9 shows the schematic representations of atomic polarizations in three stages of NMOR. It should be noted that the atomic polarizations have not drawn into scale. Before optical pumping, all the ground state sublevels are equally populated and there is no coherence in the system. Such a state is represented by a sphere [Figure 2.9 (a)]. Interaction with the linearly polarized light ($x$-plarized) results redistribution of the atomic populations, which leads to a Zeeman coherence. The state of these polarized atoms is represented by a dumbbell-shaped surface. [Figure 2.9 (b)]. In the presence of a magnetic field $B$, the atomic alignment hence the "dumbbell" rotates along the axis determined by the magnetic field [Figure 2.9 (c)]. The rotation of the atomic alignment leads to the rotation of the plane of polarized light.

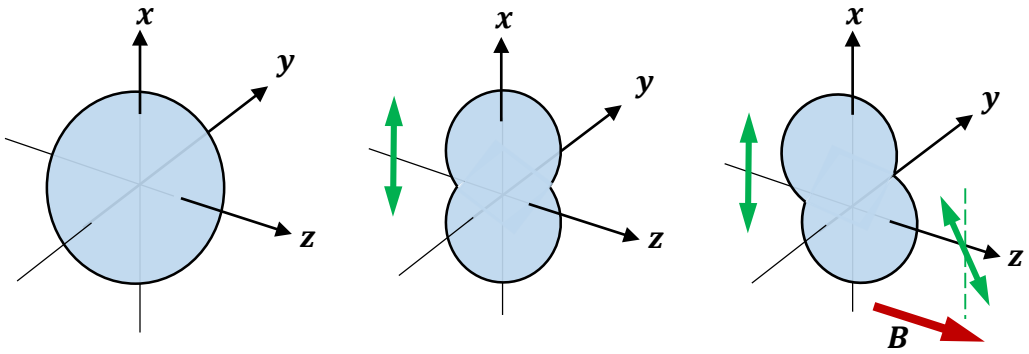


(a) (b) (c)

Figure 2.9 Schematic representation of atomic polarization. (a) Before optical pumping the atoms are unpolarized, which is represented by a spherical surface. (b) Interaction with the $x$-polarized light causes the redistribution of atomic populations and creates Zeeman coherence. This atomic polarization is represented by a dumbbell-shaped surface. (c) Net rotation of the atomic alignment in the presence of a magnetic field leads to the rotation of the plane of linearly polarized light. These representations correspond to an $F = 1 \rightarrow F' = 0$ system.

The magnetic field dependence of the rotation angle is given by the following equation.

$$\varphi \simeq \eta \frac{l}{2l_0} \frac{2g\mu_B B/\gamma_{rel}}{1 + (2g\mu_B B/\gamma_{rel})^2} \tag{2.19}$$

where $\eta < 1$ is the factor that measures the efficiency of optical pumping and probing in the system and $\gamma_{rel}$ is the relaxation rate of the atomic alignment. It is clear from Equation 2.19 that the magnetic field dependence of the optical rotation produced by the alignment precession coherence effect is much similar to linear Faraday rotation. The only difference is the atomic resonance width is replace with the $\gamma_{rel}$. Since the magnitude of the $\gamma_{rel}$ is much smaller than the atomic resonance width, the small-field optical rotation from the coherence effects is much larger than that for linear magneto-optical rotation.

The optical rotation width decreases in size from hundreds of Gauss to ~μGauss for linear- to nonlinear magneto-optical rotation, therefore NMOR allows a more sensitive magnetometry.

#### 2.2.4.2 Relaxation of atomic polarization

According to Equation 2.19, the optical rotation is a function of the relaxation rate of atomic alignment or atomic polarization. When atoms collide with the wall of their container (atomic vapor cell), atomic polarization is destroyed. Generally two methods are used to increase the relaxation time. The first method is coating of the inner cell wall with a chemical such as paraffin. The alkali atoms in these antirelaxation-coated cells bounce off the cell walls up to ~ $10^4$ times before they relax their atomic polarization, which results in extremely narrow magneto-optical resonances [52, 53]. The second method is filling the alkali vapor cell with a high pressure of an inert buffer gas such as helium to inhibit the diffusion of alkali atoms towards the wall. Since alkali atoms depolarize upon the collision with the glass wall of the vapor cell, at high buffer gas pressure, alkali atoms need a much longer time to reach the cell wall, which minimizes the number of wall collisions [54].

Relaxation of atomic polarization can occur through some other mechanisms. For instance, spin-destruction collisions involve the collisions of alkali atoms with the buffer or quenching gases; spin-exchange collisions involve the collision of oppositely polarized alkali atoms with the preservation of the total angular momentum. Spin exchange relaxation-free (SERF) atomic magnetometers have been developed to minimize the effect of spin-exchange collisions [27].

#### 2.2.4.3 NMOR feature in antirelaxation coated cells

In paraffin-coated cells, the NMOR feature depends on other two effects in addition to the Bennett-structure effect and the coherence effect. The first one is “the transit effect” in which the optical rotation width is determined by the transit time of atoms through the light beam as they make one pass through the light beam (Figure 2.10). This is an additional nonlinear effect which can be observed “nested” in the magnetic-field dependent profile in NMOR. The Narrowest NMOR feature is due to “the wall-induced Ramsey effect” in which atoms leave the light beam after being optically pumped and later optically probed when they return to the light beam after colliding with the cell walls [55]. This effect can be considered as a variant of the separated-field transit effect. The only difference between the transit effect and the wall-induced Ramsey effect is the polarization lifetime.

#### 2.2.4.4 Overcoming of NMOR limitations

The NMOR is very sensitive method for detecting magnetic fields. But it has some limitations, for example, it is limited to weak magnetic fields only and cannot be directly extended to fields higher than the widths of the typical resonance. Another limitation is NMOR confers scalar magnetic field measurements; it just yields absolute intensity of the field but no directional information. These limitations can be successfully overcome by using modulated laser light. The light can be modulated by either frequency or amplitude. In our experiments, we use frequency-modulated laser light [54].

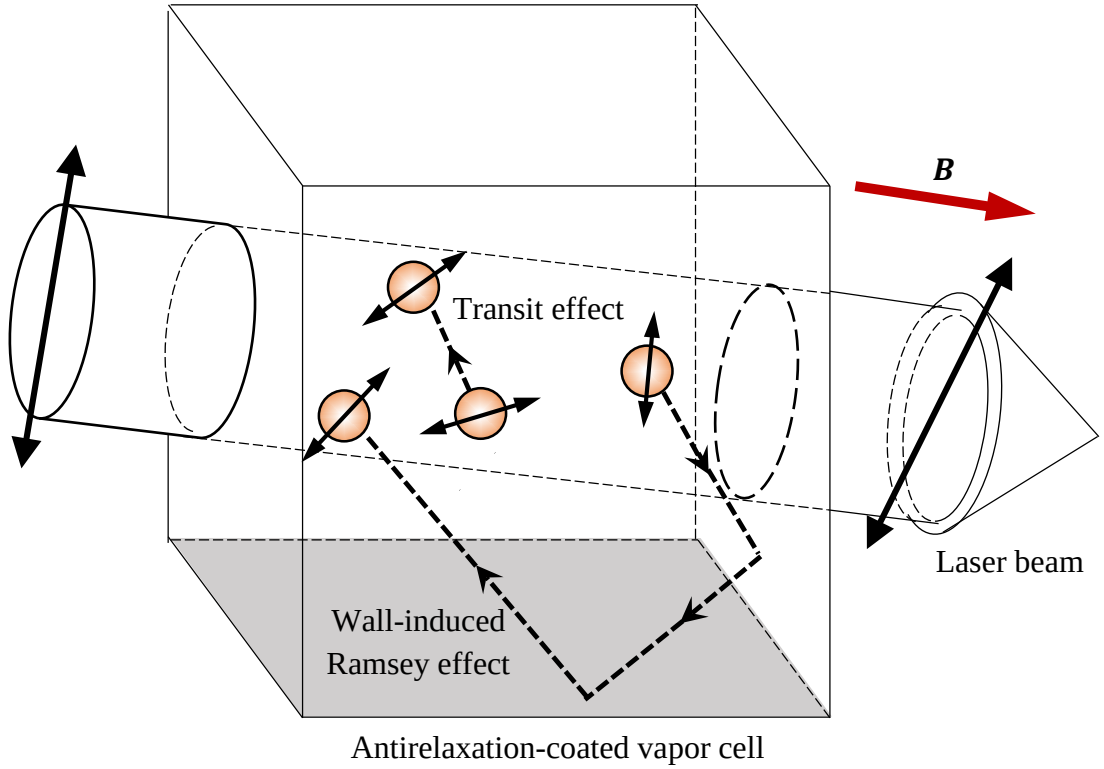


Figure 2.10 Illustration of the NMOR effects in the antirelaxation-coated vapor cell. Gaseous atoms polarize by the linear polarized light when they pass through the beam. In the presence of a magnetic field atomic polarization precesses. The plane of the linearly polarized light rotates upon a second interaction with the atoms, either during a single pass through the beam (transit effect), or after the atoms exit and re-enter the beam (wall-induced Ramsay effect).

#### 2.2.4.5 NMOR with frequency-modulated light

Atomic magnetometers based on frequency modulated NMOR are widely used in many applications of geophysical field measurements, nuclear magnetic measurements, magnetic resonance imaging and magnetic particle detection. There are many practical advantages of using frequency modulated light in NMOR. Some of those advantages are discussed below.

Noise and systematic effects associated with spurious rotations can be dramatically reduced with the frequency modulated NMOR. For example, the problem called "drifting zero" – any relative rotation of the analyzer and polarizer (this happened in previously used polarization modulation technique), or an alternation in the birefringence of the optical elements, will be detected as an optical rotation signal. This signal cannot be distinguished from the desired signal due to magneto-optical rotation by the atoms. When frequency modulation is implemented, most of the sources that cause spurious rotation do not lead to spectral features as sharp as atomic resonance, so they do not produce significant optical rotation at the modulation frequency. Therefore, the detection of the optical rotation at light modulation frequency avoids such problems [56].

Another advantage of measuring NMOR with a single frequency modulated light is additional ultra-narrow resonances are observable when the light modulation frequency $\omega_m$ coincides with twice the Larmor precession frequency, $2\omega_L$ (and also with $\omega_L$, etc.). This substantially extends the dynamic range of NMOR-based atomic magnetometer above the Earth field range (~$5 \times 10^{-5}$ T) thus useful in many applications [56].

Magnetic fields can be directly measured by using frequency modulated NMOR. In order to do that, the frequency of the laser is modulated to achieve resonance condition

with the atomic precession. As described before, the light modulation frequency is related to the Larmor precession frequency of the atomic alignments by the following equation.

$$\omega_m = 2\omega_L \tag{2.20}$$

So Larmor precession frequency of atoms can be measured by using laser modulation frequency.

The Larmor precession frequency is related to the applied magnetic field by

$$\omega_L = \gamma B \tag{2.21}$$

where $\gamma$is the gyromagnetic ratio which serves as the conversion factor between the frequency and the field strength. Therefore magnetic fields can be directly measured by the aid of Equation 2.21. This is the fundamental equation for atomic magnetometry.

## 2.3 Sensitivity of atomic magnetometers

In general, magnetometers are characterized by their sensitivity. The sensitivity of a magnetometer can be considered either as the smallest change in the magnetic field level that the sensor can discern, or as the size of the smallest magnetic field that it can detect. At the fundamental level, the magnetometer actually measures the energy splitting between the Zeeman sublevels of the atomic ground state due to the magnetic field (Equation 2.21, derived from $\hbar\omega_L = g\mu_B B$ where $g\mu_B/\hbar = \gamma$). So it is clear that sensitivity of atomic magnetometers can be expressed by using Equation 2.21 as

$$\delta B = \frac{\delta\omega_L}{\gamma} = \frac{1}{\gamma\tau} \tag{2.22}$$

where $\tau$ is the coherence lifetime (the time taken by an atom to go from the polarized state to the unpolarized state). The spectroscopic linewidth $\Delta\omega_L$ in Equation 2.22 is given by the

coherence lifetime $\tau$. Equation 2.22 was derived by using the observation that a measurement with a single atom with the duration of $\tau$ produces an uncertainty in the Larmor precession angle of the order of 1 rad. Rearranging the above equation for $N$ number of atoms and the measuring time $T$ results the following equation [28].

$$\delta B = \frac{1}{\gamma\sqrt{N\tau T}} \tag{2.23}$$

This is the equation for the intrinsic sensitivity of an atomic magnetometer. Generally we use 20 ms / 30 ms as measuring time for our experiments. It should be noted that units of sensitivity are $\mathrm{T}/\sqrt{\mathrm{Hz}}$ or $\mathrm{G}/\sqrt{\mathrm{Hz}}$ .

It is clear from Equation 2.23 that if the polarization lifetime is longer, then the magnetometer is more sensitive. As described in Section 2.2.4.1.2., two methods are generally used to achieve long polarization lifetimes, which are filling the alkali vapor cell with a high pressurized buffer gas or coating the cell wall with paraffin. In our experiments, we use paraffin coated Cs atomic sensors.

Detection of magnetic fields by NMOR is based on measuring of optical rotation angles by polarimeters. In addition to the intrinsic sensitivity described before, the polarimeter sensitivity to light polarization rotation $\delta\varphi$ should also be considered. $\delta\varphi$ is given by the following equation [28].

$$\delta\varphi = \frac{1}{2\sqrt{\dot{N}_{ph}T}} \tag{2.24}$$

where $\dot{N}_{ph}$is the probe-photon flux (in photons per second) behind the atomic sample and $T$ is the measuring time. The units of $\delta\varphi$ is $\mathrm{rad}/\sqrt{\mathrm{Hz}}$. $\delta B$ and $\delta\varphi$ are related to each other by the equation:

$$\delta B = \left(\frac{\delta\varphi}{\delta B}\right)^{-1} \delta\varphi \tag{2.25}$$

where $(\delta\varphi / \delta B)$ is the slope of the optical rotation with respect to a longitudinal magnetic field $B$ [55].

From a pure experimental point of view, the magnetic field noise should be minimized and the optical detecting system should be stable. Diode lasers are stable and can be tuned very easily, which allows measurements of optical rotation with extremely low noise. The resonance signal can be enhanced by increasing the number of alkali atoms $N$, either by increasing the vapor density or by using a large vapor cell. However, spin-exchange collisions at high vapor density can limit the polarization lifetimes of atoms. But spin exchange relaxation-free (SERF) magnetometers have been developed to overcome this issue. These SERF magnetometers operate at zero magnetic field to enable longer polarization lifetimes and has achieved sensitivity better than 1 $\mathrm{aT}/\sqrt{\mathrm{Hz}}$ (57).

## 2.4 Cs-based magnetometer instrumentation

Construction of a compatible Cs-based magnetometer is a part of this dissertation. Therefore, a complete description of the constructed instrument will be presented in Chapter 5. The principle of the constructed new instrument is much similar to our old one except the compatible structure and some alternations. Here we present a brief summary of our old instrument which was used to obtain the experimental results in Chapter 3 and 4.

The main instrument is composed of magnetic shields with internal coils, cesium vapor cells, a diode laser with controlling electronics, optical components, and electronics

for signal amplification and data acquisition (Figure 2.11). A four-layer magnetic shield is employed to reduce the laboratory magnetic field and noise. Internal coils which are mounted inside the magnetic shields are used to provide a bias magnetic field and to balance the residual magnetic fields and gradients. The bias field is used to define the detection axis of the magnetometer. It is coaxial with the magnetic field of the sample and with the propagation of the beam.

A glass cell containing cesium vapor is used as the magnetic field detector. The inner wall of the cell has been coated with a layer of paraffin to minimize relaxation of ground-state polarization due to collision with the wall. Cesium was chosen over potassium and rubidium because it has the highest vapor density at a given temperature. In addition, cesium is isotopically pure, making it efficient to lock the laser wavelength without interferences from other isotopes.

A diode laser (New Focus, model 7018) with linear polarization was tuned to the F =4 → F'=3 of $D_1$ line transition of $^{133}Cs$. Two beam samplers are used for producing two side beams to control the laser. The first one feeds a power monitor for constant-power operation. The second one is used for a dichroic atomic vapor laser lock (DAVLL), employed to lock the laser at the optimal wavelength. A mirror coated with gold was placed at the back of the Cs cell, which makes the light reflected back to the cell, leading to an increase in optical length that leads to increased sensitivity. A lock-in amplifier measures the rotation of light based on the differential photocurrents. A LABVIEW program is developed for both controlling the frequency modulation and signal processing.

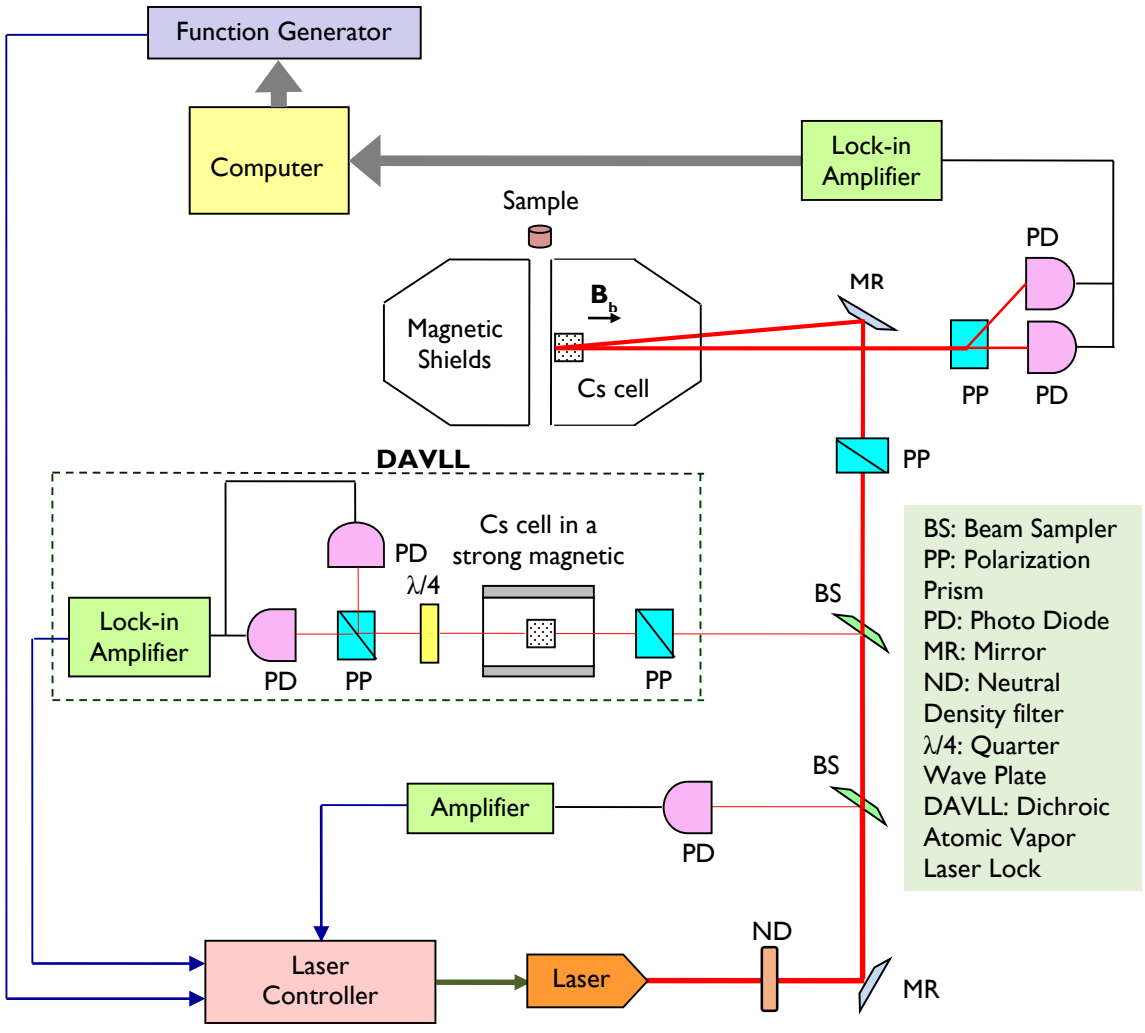


Figure 2.11 Optical layout of a Cs-based atomic magnetometer.

The main portion of the laser beam is used for both optical pumping and probing. The polarization of the probe beam is rotated after it passes through the polarized cesium atoms in the presence of a magnetic field. The rotation angle is measured by using two photo diodes and its value is given by the equation [58].

$$\varphi = \frac{I_1 - I_2}{2(I_1 + I_2)} \tag{2.26}$$

where $I_1$ and $I_2$ are the photocurrents of photodiodes and φ is the optical rotation angle.

The magnetic field to be measured is coaxial with the propagation of the laser beam. In the presence of the magnetic field, optically pumped atoms precess with Larmor frequency ($\omega_L$). The frequency of the laser is modulated to achieve resonance condition with the atomic precession as described in Section 2.2.4.2. The modulation frequency of the laser is swept to observe the nonlinear magneto-optical resonance, which occurs when the modulation frequency is equal to twice the Larmor precession frequency. So Larmor precession frequency of Cs atoms are measured.

When the modulation of light is synchronized with the atomic precession, the magnetic field of the sample, $B_s$, is deduced from the corresponding precession frequency according to the equation:

$$\omega_L = \gamma(B_b + B_s) = \frac{g\mu_B}{\hbar(2I + 1)}(B_b + B_s) \tag{2.27}$$

where γ is the gyromagnetic ratio of cesium (3.5 Hz/nT), $\mu_B$ is the Bohr magneton, $\hbar$ is the Planck's constant, g is the electron g factor, $I$ is the nuclear spin quantum number and $B_s$ is the magnetic field from the sample. The biased magnetic field $B_b$ is a known value [59]. Therefore the magnetic field of the sample is measured directly. The sensitivity of our instrument is 100 $\mathrm{fT}/\sqrt{\mathrm{Hz}}$ for dc magnetic fields.

## 2.5 Detection of magnetic particles using an Cs-based atomic magnetometer

We directly measure the magnetic field arising from magnetic particles which were previously magnetized by using a permanent magnet (~1 T). In order to do that, we scan the sample with magnetic particles by moving them towards the sensor. The sensor detects the magnetic signals in the direction of light propagation (the same direction as the bias field). Therefore it is important to consider the orientation of magnetic dipole moment in the space. Consider a dipole moment $m$, which is directed along the $z$-direction as shown in Figure 2.12.

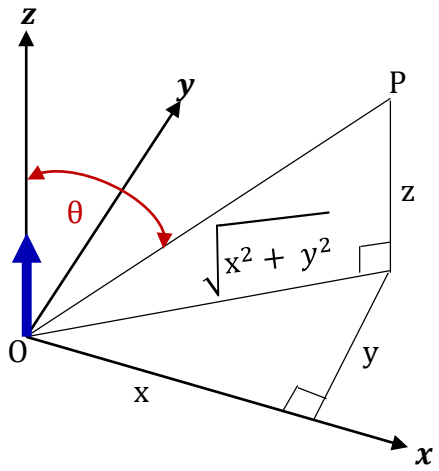


Figure 2.12 Representation of the magnetic dipole moment of magnetic particles in three-dimensional Cartesian coordinate system.

The magnetic field components of a magnetic dipole moment $m$ in the $x$-, $y$- and $z$-directions at any arbitrary point P are given by the following equations:

$$B_x = \frac{3m \sin\theta \cos\theta}{r^3} \tag{2.28}$$

$$B_y = 0 \tag{2.29}$$

$$B_z = \frac{m(3\cos^2\theta - 1)}{r^3} \tag{2.30}$$

where $r$ is the distance between the dipole moment and point P, $\theta$ is the angle between the direction of the dipole moment and the line OP. The sensor detects the magnetic field component $B_z$ in the $z$-direction. Figure 2.13 shows the variation of the $B_z$ with different angles of $\theta$ for a given distance of $r$.

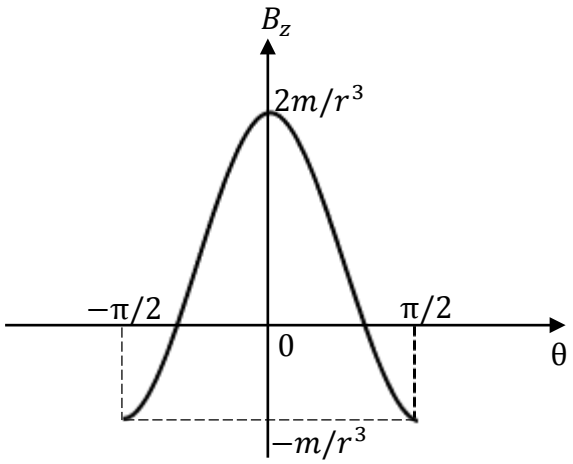


Figure 2.13 Variation of the magnetic field component $B_z$ in the $z$-direction with different angles.

Since the magnetic field is a function of $r$, it is essential to determine the magnetic dipole moment (or magnetization) of the particles to quantify magnetically labelled molecules. To achieve this, we use a magnetic field profile which was generated by scanning the magnetic sample perpendicular to the laser ($x$-direction). The atomic

magnetometer measures the magnetic field generated by the magnetic particles at each position during the scan. The result for a single scan along the $x$-direction is shown in Figure 2.14. Since the magnetic field corresponds to the overall dipolar field of the magnetic particles, the profile follows the following equation.

$$B = B_0 + \frac{\mu_0 M}{4\pi[(x - x_0)^2 + d^2]^{3/2}}\left(3\frac{d^2}{(x - x_0)^2 + d^2} - 1\right) \tag{2.31}$$

where $B$ is the magnetic field measured by the magnetometer, $B_0$ is the base line correction, $x_0$ is the position of the $x$-axis that corresponds to the maximum signal and $d$ is the distance between the sample and the detector. $M$ is the magnetic dipole moment (or magnetization as a relative term). We obtain both the magnetic dipole moment (magnetization) of the particles and the distance between the sample and the detector by performing a least-square fit on the magnetic field profile. Since atomic magnetometers directly measure the absolute value of magnetic fields, the magnetization values are no need to calibrate [60].

In our FIRMS technique, we use this scanning method for magnetic particle detection. In the next chapter, we will present the FIRMS technique in characterizing DNA duplex interactions with single-base pair resolution.

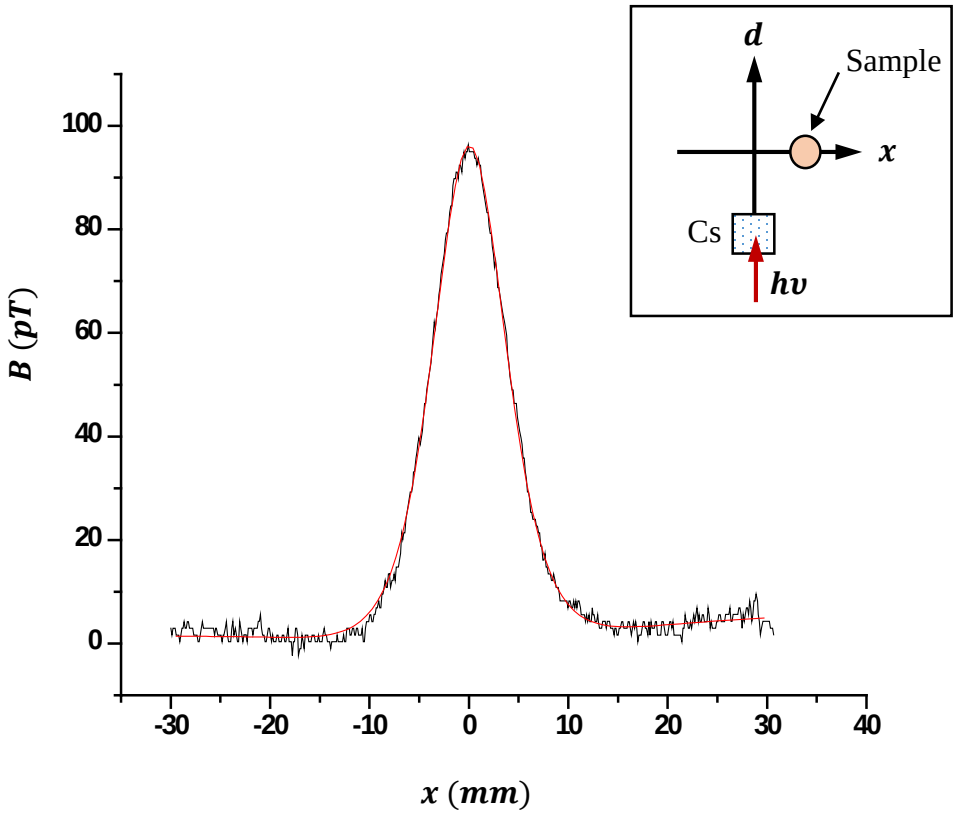


Figure 2.14 Magnetic field profile of a sample with magnetic particles. The position which corresponds to the maximum magnetic signal ($x_0$) has normalized to the zero in this figure for convenience. The least square fit on the magnetic field profile yields the magnetic dipole moment of the particles, $2.66 \times 10^{-10}$ $Am^2$. The inset shows the geometry of the scanning axes with respect to the Cs detector and the laser beam.

# Chapter 3

# Force-Induced Remnant Magnetization Spectroscopy with Single-Base Force Resolution

This chapter presents the application of force-induced remnant magnetization spectroscopy (FIRMS) as a force spectroscopy with molecular specificity in characterizing the noncovalent binding of DNA duplexes. It consists of motivation of the study of molecular interactions, resolution of DNA duplexes with single base-pair difference, measurements of the binding forces of DNA oligomers, detection of multiple DNA interactions, and dependence of the dissociation force on DNAs' mismatching position.

## 3.1 Motivation of the study

As discussed in the previous chapters, the main focus of this dissertation is using magnetic particles for molecular spectroscopy, using the techniques we have developed based on atomic magnetometry. The reason for detecting various molecular targets relates to the mechanism of biological processes and disease diagnostics [61]. We use the FIRMS technique in order to achieve quantitative molecular identification based on the binding forces of the involved noncovalent interactions. The molecular systems are various DNA duplexes.

## 3.2 Significance of DNA duplex interaction

Deoxyribonucleic acid (DNA) contains the genetic information that is used in the development and functioning of most living organisms. The main role of DNA molecules is the long-term storage of genetic information. DNA consists of two long polymers, with backbones made of sugar molecules and phosphate groups joined by ester bonds. These two strands run in opposite directions to each other. The double-stranded structure arises as the four types of molecules attached to the sugar-molecules, called bases (Adenine (A), Cytosine (C), Guanine (G) and Thymine (T)) forming hydrogen bonds between the two separate chains as shown in Figure 3.1.

Noncovalent binding between the two DNA or RNA strands in a double helix is one of the most important molecular interactions in chemistry and the life sciences [62 - 65]. For example, DNA binding is critical to understand the fundamental biological processes such as DNA replication, transcription, repair and drug effects. Furthermore, the

sequence-specific binding between DNA strands has been used for molecular sensing [66, 67] and construction of novel composite materials [68, 69]. Therefore, investigating the binding forces of DNA/RNA is of both fundamental significance and practical merit. Extensive research has been devoted to investigating DNA/RNA binding forces, primarily using atomic force microscopy (AFM) [70-72] and optical tweezers [73-75]. These techniques have provided detailed information on the conformational changes and binding forces during DNA/RNA stretching and dissociation. The force resolution of optical tweezers has reached sub-piconewton (pN) [73]. However, the resulting force distribution is generally broad, on the order of ten pN [75, 76].

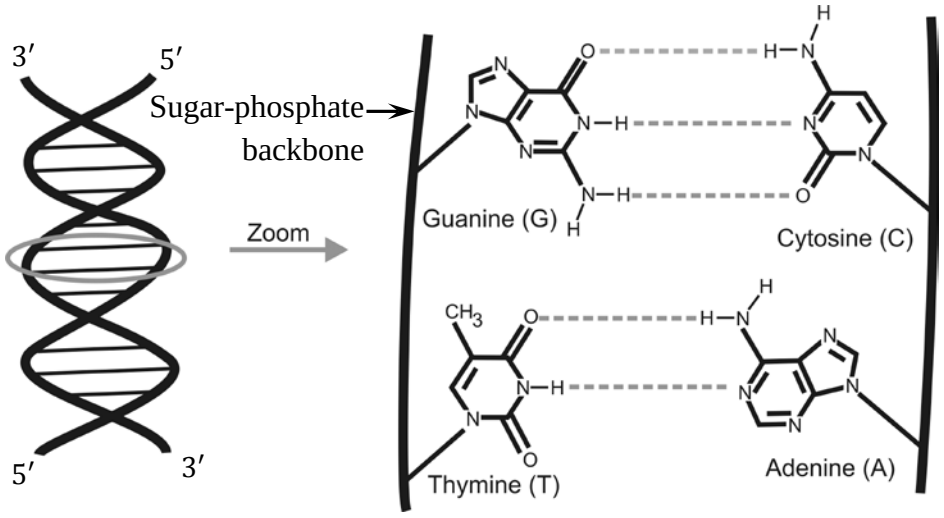


Figure 3.1 Schematic representation of double-stranded DNA. Two strands run in opposite direction to each other where each one is named by 3′ end to 5′ end. The zoom-in image on the right shows the base pairing between two single stranded DNA molecules. Dashed lines indicate the hydrogen bonds between complementary bases.

In addition, some important cellular processes may be difficult to measure by these methods. For example, in order to measure the ribosome translocation, an artificial hairpin

RNA and substantial external force have to be applied [77]. Therefore, an open question is whether it is possible for a technique to measure a well-defined force of DNA or RNA systems with minimum invasion.

In order to address this question, we developed FIRMS technique that uses an external mechanical force to distinguish different noncovalent bonds. A complete description of the FIRMS technique has been provided in the first chapter. Briefly, FIRMS is based on the following concept: the magnetically labelled ligand molecules undergo Brownian motion once they dissociate from the receptor molecules, randomizing the magnetic orientations of the particles and consequently decreasing the magnetization. Initially, we reported this technique to distinguish specific antibody-antigen noncovalent bonds from nonspecific physisorption [22]. Then we used our technique to measure the binding force between an antibody-antigen pair, which was substantially higher than the binding force of physisorption [23]. However, it remains unknown whether our technique can resolve different noncovalent bonds. One ultimate test for revealing force resolution will be measuring the binding forces of DNA duplexes because their binding forces can be finely tuned by changing the sequences and because extensive experimental work and theoretical modelling are both available for comparison.

Here, we show the feasibility of determining well-defined, sequence-specific binding forces for DNA duplexes by using the FIRMS technique. The binding forces have a very narrow distribution. Multiple DNA interactions with only one base pair (bp) difference can be completely resolved. In addition, DNA strands that differ only in the position of a mismatched base may have different binding forces. The results will have

significant impact on fundamental biochemical research, theoretical modeling, and other applications.

## 3.3 Experimental Section

### 3.3.1 Immobilization and Hybridization of DNA

Immobilization of DNA strands onto surfaces such as gold or biotinylated glass via linker molecules and hybridization of those strands with complementary strands are widely used in current researches. We use the established methods in the literature for sample preparations. The following is the chemistry behind the immobilization and hybridization processes.

Thiol groups (SH) can bind with gold surface to form a stable, covalent bond (Figure 3.2) [78]. We use thiol-modified single stranded DNA (ssDNA) to create a molecular layer on a gold surface, which is used as a platform for hybridization with the complementary strands. These thiol-modified DNA molecular layers can be studied by using various techniques such as surface plasmon resonance spectroscopy [79], X-ray photoelectron spectroscopy, $^{32}$P-radiolabeling [80] and neutron reflectivity [81].

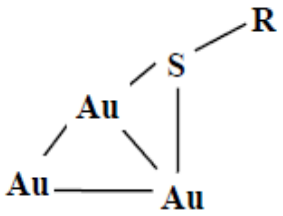


Figure 3.2 Covalent binding between thiol and gold, which has bond energy of 418 kJ/mol and binding force of 1.4 nN.

Before the immobilization, we clean the gold surface with Piranha solution, which is a volume mixture of 70% concentrated sulfuric acid ($H_2SO_4$) and 30% hydrogen peroxide ($H_2O_2$). Piranha is used to clean organic residues of substrates because the mixture is a strong oxidizer, it will remove most organic matter. The following is the chemical reaction between $H_2SO_4$ and $H_2O_2$.

$$H_2SO_4 + H_2O_2 \longrightarrow H_3O^+ + HSO_4^- + O$$

Cleaned gold surface is then treated with thiol-modified ssDNA oligomers. We purchase these small oligomers from Integrated DNA Technologies (Iowa, USA). There is a chain of six $CH_2$ groups (C-6 linker) in between DNA and sulfur atom (Figure 3.3). This C-6 linker provides good flexibility for hybridizing with the complementary strand. Thiol-modified ssDNA are available as R-S-S-R form, which are reduced to SH- groups by using *tris*(2-carboxyethyl)phosphine (TCEP) as a reducing agent.

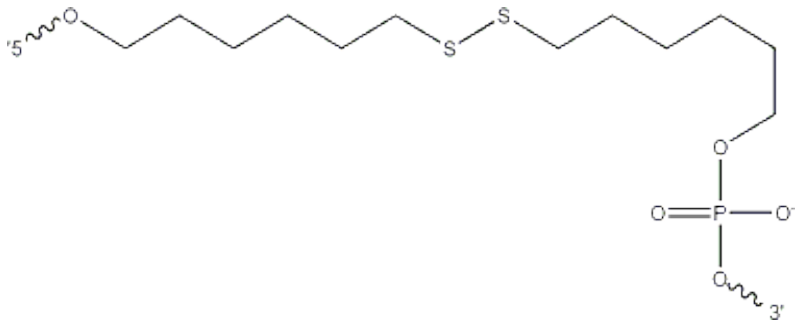


Figure 3.3 Thiol-modified group in ssDNA in which C-6 linker increases the flexibility of ssDNA.

All DNA oligomers are dissolved in 10 mM tris(hydroxymethyl)aminomethane, 1 mM EDTA (TE-buffer solution) and 1 M NaCl solution of pH 8.0. TE-buffer solubilizes DNA, while protecting it from degradation. DNA nucleases are supposed to be less reactive

at pH 8.0. EDTA (ethylenediaminetetraacetic acid) further inactivates nucleases by chelating metal cations such as $Mg^{2+}$, which are required for the activity of these enzymes. NaCl facilitates the hybridization of DNA by providing $Na^{+}$ ions that block the negative charges from phosphates on DNA and allow two complementary DNA molecules to approach together.

Before hybridizing with the complementary strands, ssDNA molecular layers are optimized for hybridization by introducing mercaptohexanol (MCH) as the spacer molecules (Figure 3.4). MCH is known to diminish the non-specific interactions between the gold surface and ssDNA molecules by lifting the ssDNA molecules from the surface, which makes them more accessible for hybridization [81].


Figure 3.4 Mercaptohexanol (MCH) which acts as a spacer molecule to make ssDNA molecules more accessible for hybridization.

Biotinylated complementary strands (Figure 3.5) are then introduced into the sample system for hybridization. Those strands have also been dissolved in the same buffer solution. Before adding streptavidin-coated magnetic particles, 1% (w/v) bovine serum albumin (BSA) solution in tris-buffered saline (TBS) solution is introduced to the system, which also contains 0.05% of the detergent Tween 20. BSA is a blocking agent that prevents non-specific binding of magnetic particles on the gold surface. Streptavidin forms strong bonds with the biotin group of complementary strands.

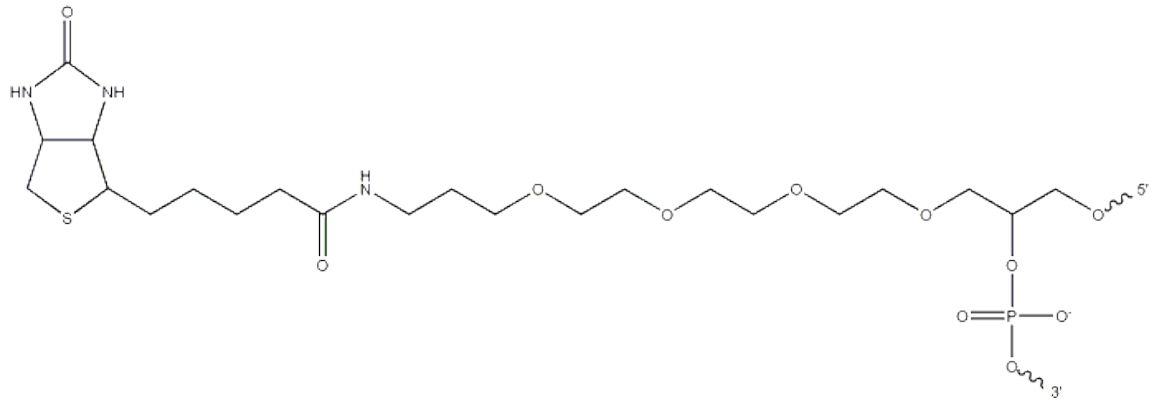

Figure 3.5 Biotinylated group in ssDNA in which biotin group connects to the DNA via a linker molecule which facilitate the binding of biotin and streptavidin.

### 3.3.2 Experimental steps

A sample well (4 mm × 2 mm × 1 mm) with a gold-coated bottom surface (Figure 3.6) was loaded with 8 μL of 10 μM single-stranded thiolated oligonucleotides 5'-thiol-GGG TTT TTT GGG-3' (IDT DNA) in 10 mM tris(hydroxymethyl)aminomethane, 1 mM EDTA (TE-solution) and 1 M NaCl solution of pH 8.0 for 2 hours. After rinsing with water, the sample well was immersed in 8 μL of 1 mM mercaptohexanol for 1 hour, rinsed in deionized water, and dried again under nitrogen.

For hybridizing, the cell was incubated with a solution of biotinylated probing strand, with sequences 5′-CCC AAA AAA CCC-3′ (complementary), CCC GAA AAA CCC (9th-mismatched), 5′-CCC AGA AAA CCC-3′ (8th-mismatched), or 5′-CCC AAG AAA CCC-3′ (7th-mismatched). The sample well was then immersed in a 1% (w/v) bovine serum albumin (BSA) solution in tris-buffered saline (TBS) solution containing 0.05% of the detergent Tween 20 for 2 hours. After incubation with 8 μl of streptavidin-coated magnetic particles (Invitrogen, M280) for 3 hours, the sample well was immersed in a heat

block at 65 ºC for 5 minutes and cooled down overnight. The sample was magnetized for 2 min using a permanent magnet after the incubation. The magnetizations of the magnetic particles were measured by an atomic magnetometer.

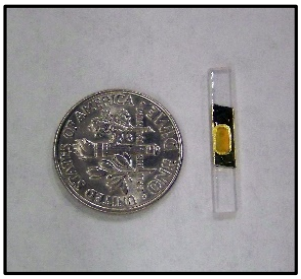

Figure 3.6 A photo of the sample well in comparison with a US dime.

Figure 3.7 shows a schematic of the experimental steps. One of the strands, termed the target strand, is immobilized on a gold-coated surface via gold-sulfur bonds [82]. The other strand, the probing strand, is labeled with a magnetic particle via biotin-streptavidin coupling. A surface area of $4\times2$ mm$^2$ of the sample well contains tens of thousands of such magnetically labeled DNA duplexes.

Mechanical forces with increasing amplitudes, provided by a shaker (VWR, 12620-942) or a centrifuge (Eppendorf 5417R), are then applied to induce the dissociation of the double strands. After each force, the magnetization M of the magnetic particles is measured by an atomic magnetometer using a scanning magnetic imaging scheme as described in Chapter 2.

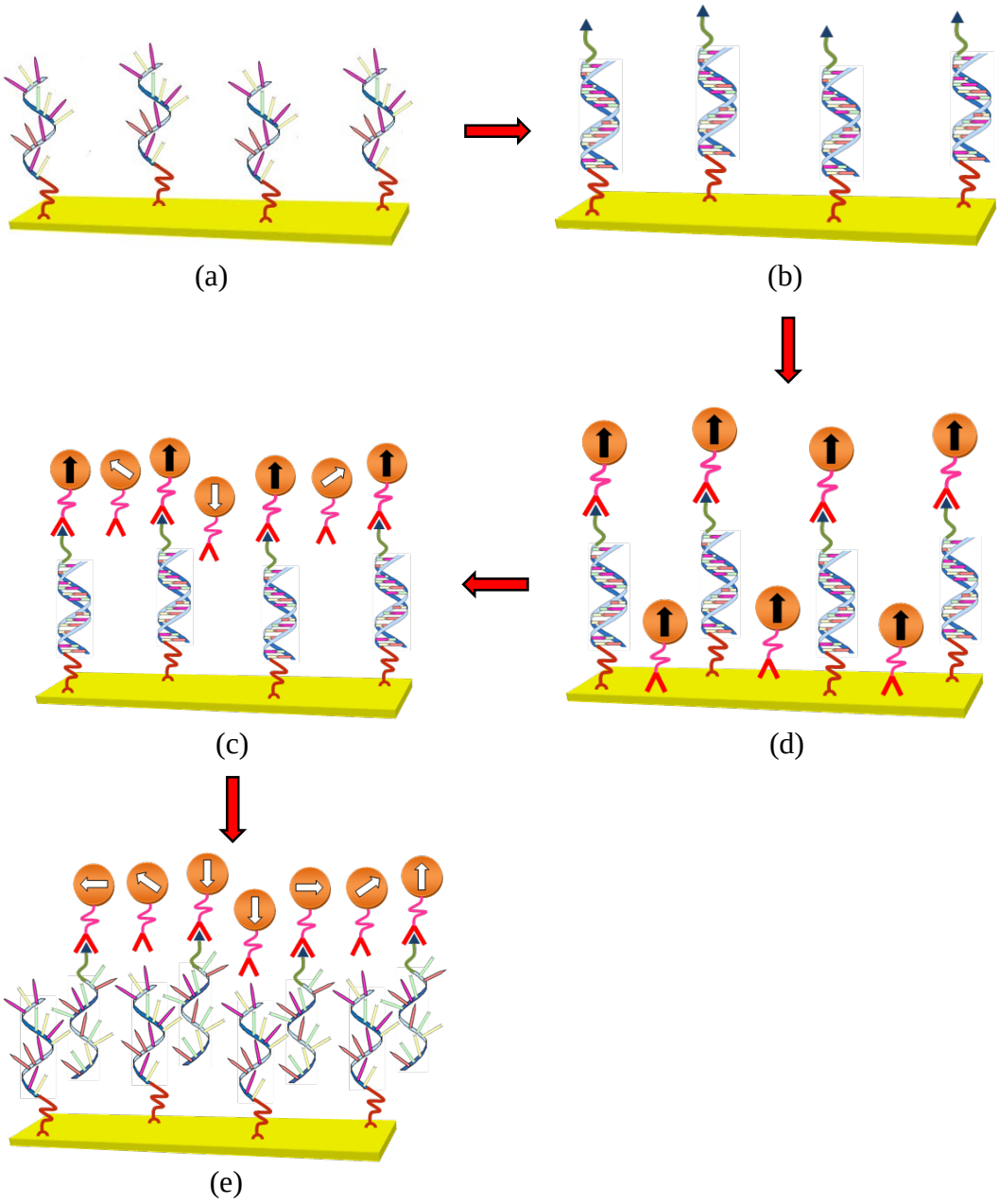


Figure 3.7 Schematic of experimental steps: (a) Immobilization of ssDNA on gold surface. (b) Hybridization with biotinylated complementary strands. (c) Incubation with streptavidin coated magnetic particles. Some particles specifically bind to DNA strands via biotin-streptavidin bond while others nonspecifically bind to the surface. (d) Application of a mechanical force causes dissociation of nonspecifically bound particles at first. (e) Further increasing of the force leads to specific dissociation of the bound particles.

## 3.4 Results and Discussion

### 3.4.1 Single base-pair resolution

Figure 3.8 shows the results of testing a single type of DNA binding in the sample, using a shaking force to induce dissociation. For the 12-bp binding, the target strand was 5′-GGG TTT TTT GGG-3′, and the probing strand was 5′-CCC AAA AAA CCC-3′, which was fully complementary to the target strand. For the 11-bp DNA binding, the target strand was the same as that for the 12-bp binding, but the probing strand was 5′-CCC GAA AAA CCC-3′, with one mismatching base at the ninth position (9th mismatching). The magnetization profiles revealed that the dissociation force was 950 rpm (revolution per minute) for the 12-bp binding and 800 rpm for the 11-bp binding. The initial decreases at 200-300 rpm in both cases were due to nonspecific physisorption, confirmed by a control experiment in which the magnetic particles did not contain the probing strands.

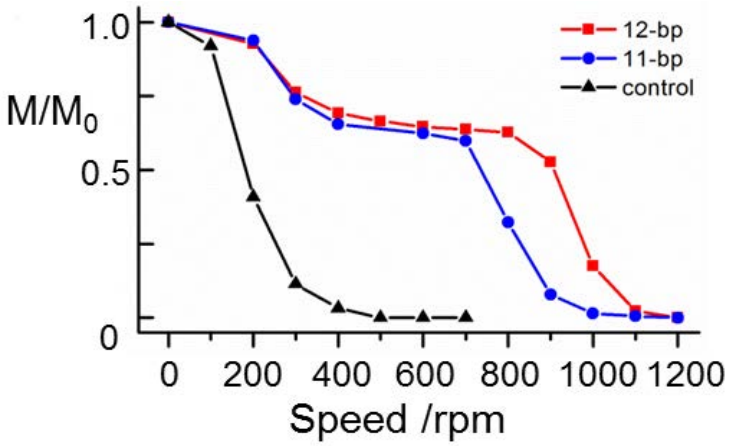


Figure 3.8 Plots of relative magnetization vs. shaking force for two different DNA duplexes, one 12 bp and one 11 bp plus a mismatching pair, and a control. $M_0$ is the initial magnetization.

For force calibration, we used centrifugal force to dissociate the 9th mismatching duplex. Figure 3.9 shows the relative magnetization vs. the centrifuge speed. The value of $M$ at 1500 rpm is $1.29\pm0.04\times10^{-10}$ Am$^2$, which we define as $M_0$ to represent the total number of specifically bound magnetic particles (Figure 3.10). The uncertainty indicates that the error for $M/M_0$ is typically 0.03 throughout this work. A sharp transition was observed between 2600 rpm and 2800 rpm.

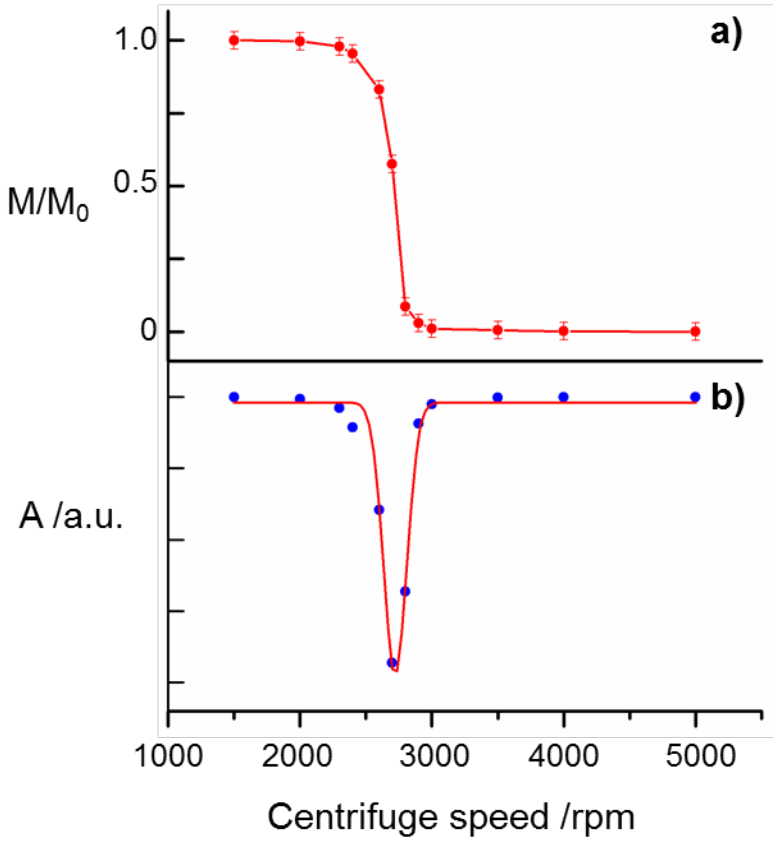


Figure 3.9 Force calibration and resolution for the 11-bp DNA binding. (a) Relative magnetization $M/M_0$ under various external forces measured as centrifuge speed. (b) The corresponding FIRM spectrum and its Gaussian fitting. A: amplitude.

To obtain the precise force value for the dissociation, we took the derivative of the

magnetization curve to obtain a FIRM spectrum [Fig. 3.9 (b)]. Fitting the spectrum with a single Gaussian function yielded a peak position of 2720 rpm. Therefore, the centrifugal force can be determined from $f = m\omega^2 r$, where $m$ is the buoyant mass of the magnetic particles, $\omega$ is the angular velocity, and $r$ is the distance of the particles from the rotation center [83].

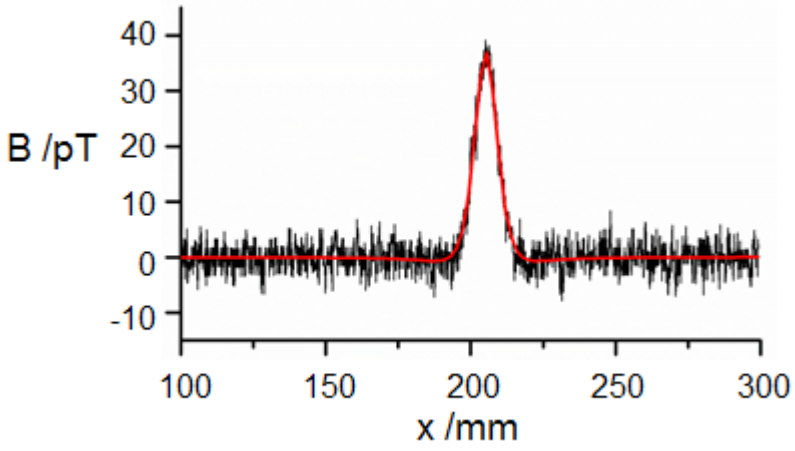


Figure 3.10 The magnetic field profile after a centrifugal force of 1500 rpm (9 pN). A magnetization value of 1.29±0.04 $\times 10^{-10}$ $Am^2$ was obtained from fitting the profile with a dipolar magnetic field model (red trace).

The M280 magnetic particles used here have a very narrow size distribution, which was verified by scanning electron microscopy (Figure 3.11). The measured average particle diameter was 2.54±0.07 μm.

The density of the particles was measured by dispersing the particles in saturated caesium sulphate ($Cs_2SO_4$) solution with continuous dilution until the particle density matches the solution density (Figure 3.12). The measured value of the particle density was 1.52±0.02 g/ml.

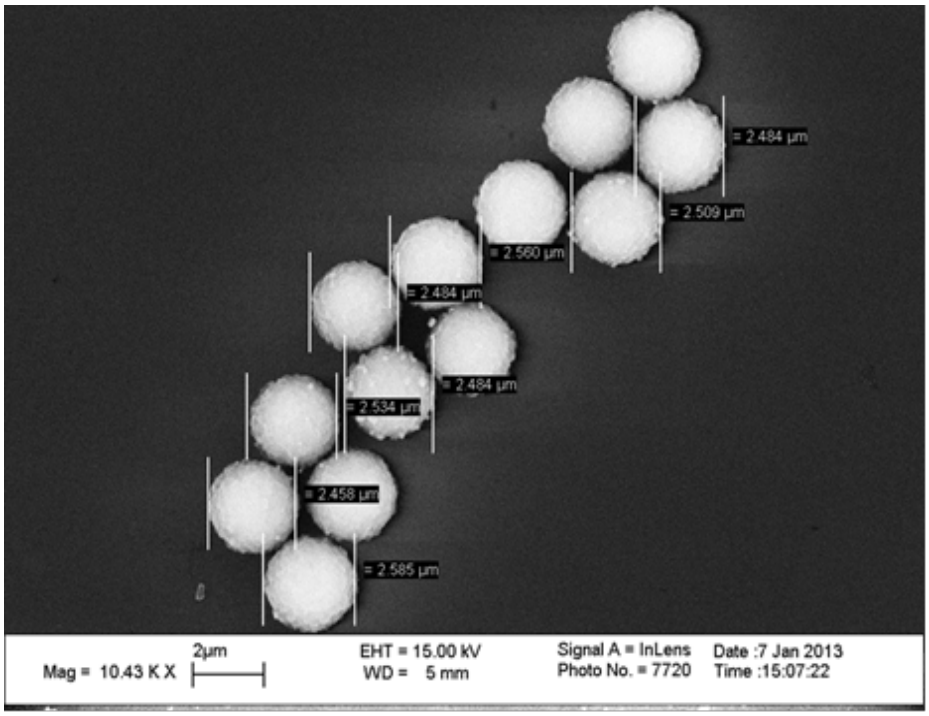


Figure 3.11 A representative SEM image of M280 particles. The average diameter was determined to be 2.54±0.07 µm.

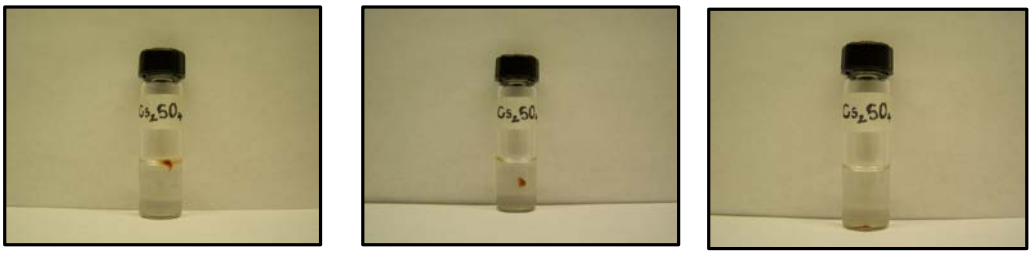

(a) (b) (c)

Figure 3.12 The density measurement of M280 particles using $Cs_2SO_4$ solution. Images show the three cases of: (a) The particle density < $Cs_2SO_4$ density (b) The particle density = $Cs_2SO_4$ density (c) The particle density > $Cs_2SO_4$ density. The measured density was 1.52±0.02 g/ml.

By using the measured diameter and the density of the particles we determined the buoyant mass in the buffer solution (density 1.0 g/ml) to be $4.6\times10^{-15}$ kg. The peak position

at 2720 rpm yields a $\omega$ value of 285 $s^{-1}$. For the centrifuge used in this work, $r$ = 8.0 cm. Therefore, the binding force for the 11-bp DNA duplex is 30 pN. The binding force for the 12-bp duplex can then be calculated using this value and the dissociation transitions in Figure 3.8: $30\times(950/800)^2$ = 42 pN. An independent force calibration for the 12-bp duplex was also performed using centrifugal force, which yields a binding force of 43 pN (Figure 3.13).

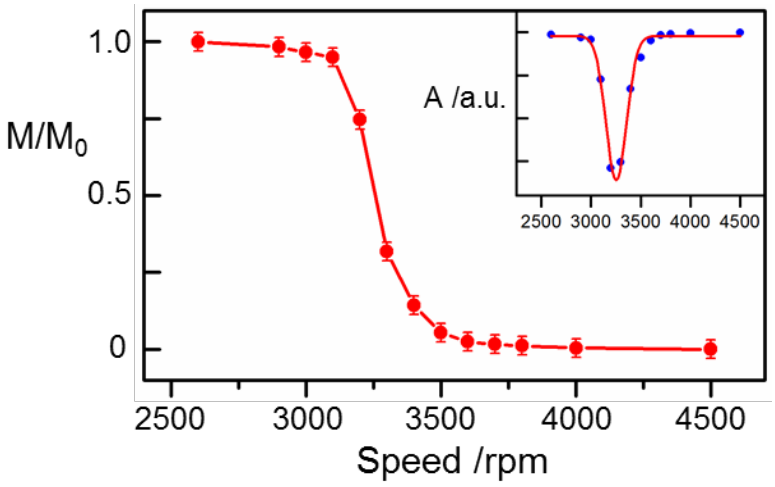


Figure 3.13 Relative magnetization vs. centrifugal speed for dissociating the 12-bp DNA duplex. Inset shows the corresponding FIRM spectrum. Gaussian fitting gives a peak position of 3250 rpm. A: amplitude.

The sharp transition in Fig. 3.9 represents a very narrow distribution of the binding force, which indicates the high resolving capability for different noncovalent bonds with different binding forces. The resolving capability can be quantified from the half-width half-maximum of the Gaussian fit. The half-width of the peak is 80 rpm, corresponding to $30 \times (2 \times 80/2720)$ = 1.8 pN. The factor of 2 is because of the square dependence of force with respect to $\omega$. For comparison, the typical half-width of the force distribution by AFM is more than 5 pN [76].

### 3.4.2 Verification of the dissociation force

To verify that the dissociation of noncovalent bonds only occurs at a certain force, we performed kinetics measurements at two different centrifugal forces: one at 23 pN (2400 rpm) and one at 42 pN (3200 rpm), i.e., before and after the above observed transition force of 30 pN, respectively. The results are shown in Figure 3.14. At 23 pN, the magnetization remained high and unchanged for as long as 20 min; no bond dissociation took place. At 42 pN, the magnetization was reduced to zero within 5 min, and the magnetization remained zero thereafter. This result confirms that the dissociation of the DNA duplex occurs only when the external force exceeds the well-defined binding force.

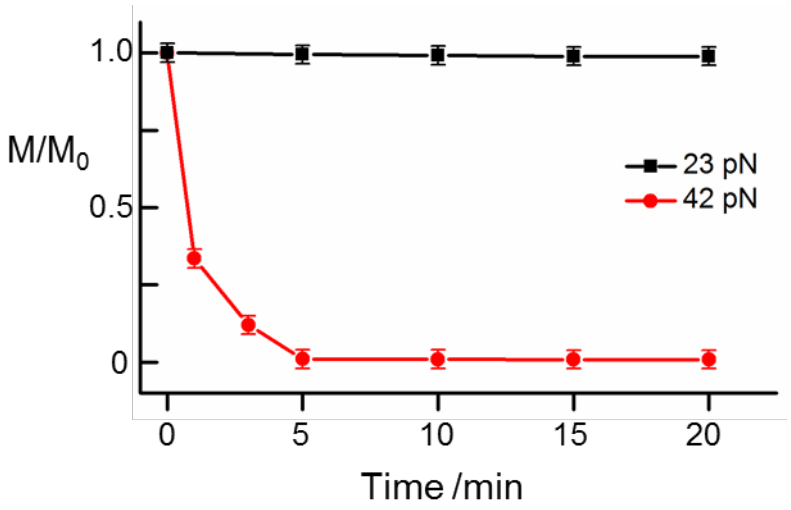


Figure 3.14 Dissociation time at two different force amplitudes, 23 pN and 42 pN, for the 11-bp DNA duplex.

To ensure that the duration of the external force does not alter the measured binding force, we varied the force duration from 5 min in Figure 3.9 to 10 min. The results are shown in Figure 3.15. Gaussian Fit of the FIRM spectrum gave a peak value of 2716 rpm. Because this value is consistent with the result of 2720 rpm from using 5 min force duration

in Figure 3.9, the measured binding force does not depend on the force duration in the tested time range. This also confirms the result in Figure 3.14 that the binding force is well-defined.

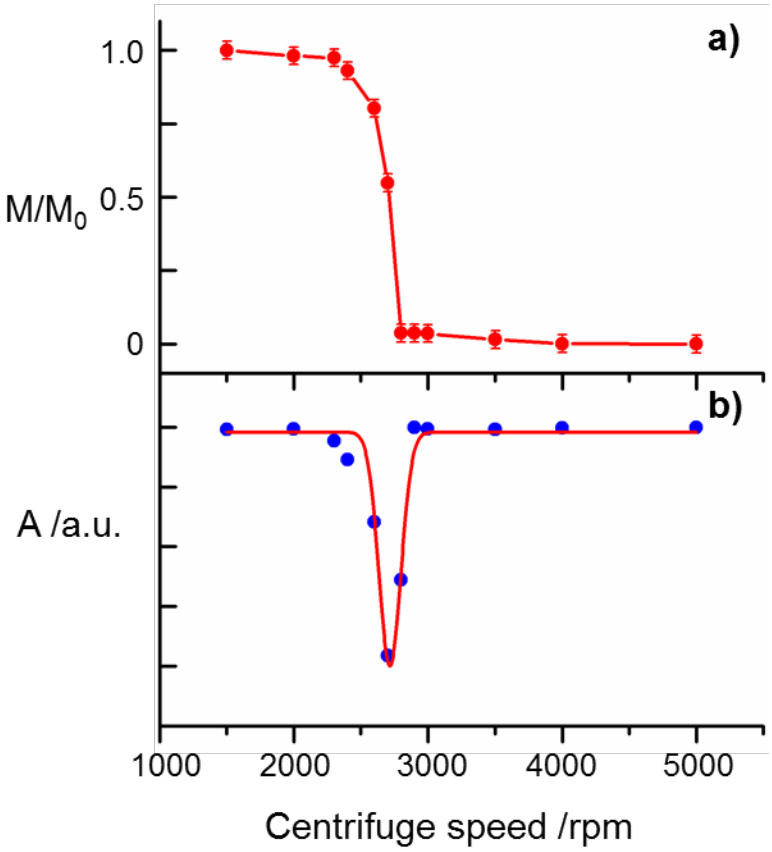


Figure 3.15 Dissociation of the 11-bp DNA binding for force durations of 10 min. (a) Relative magnetization $M/M_0$ under various external forces measured as centrifuge speed. (b) The corresponding FIRM spectrum and its Gaussian fitting. A: amplitude.

### 3.4.3 Comparison of the dissociation force

We attempt to compare the binding force values with those obtained from AFM and optical tweezers. The 12-pN difference between the 11-bp and 12-bp duplexes agrees well with both the results by AFM and optical tweezers: the AFM results showed that the force required to dissociate an A-T pairing is 9±3 pN [84], which is the difference between

the two sequences here; optical tweezers showed 10-15 pN force during the unzipping of DNA [85]. In addition, our result of 42 pN for the 12-bp duplex agrees well with the literature value of 40 pN for a similar duplex of 5′-CGC TTT TTT GCG-3′ binding its complementary sequence, obtained by AFM at a high loading rate of force [86]. Interestingly, theoretical work showed that at high loading rates, the bond strength reached a plateau [87]. AFM operating in the force-clamp mode has similar experimental condition to our FIRMS technique, in which a constant force is applied instead of a constant loading rate [88]. However, it has been mainly used for studying protein folding, not DNA rupture [89, 90]. Thermodynamic analysis indicates that a minimum of ~8 basepairs is required to have a stable DNA duplex. Our force values, 30 pN for 11-bp and 42 pN for 12-bp, are in line with this analysis and a detailed AFM study [91].

### 3.4.4 Calculation of the number of dissociated bonds

One advantage of our technique is the capability of calculating the number of dissociated bonds, which is obtained from the measured magnetization prior to the bond dissociation and using the magnetization calibration curve (Figure 3.16). For each data point, a known number of magnetic particles, calculated from particle density and sample volume, was immobilized on the surface of the sample well. Then a magnetic profile similar to that in Figure 3.10 was obtained by scanning the sample across the atomic magnetometer. Fitting the magnetic profile yields the magnetization value.

The magnetization value prior to bond dissociation was $1.29\pm0.04\times10^{-10}$ $Am^2$. Therefore, the number of bound magnetic particles was calculated to be $9.5\pm0.6\times10^4$. The error bar for $M$ is approximately $4\times10^{-12}$ $Am^2$.

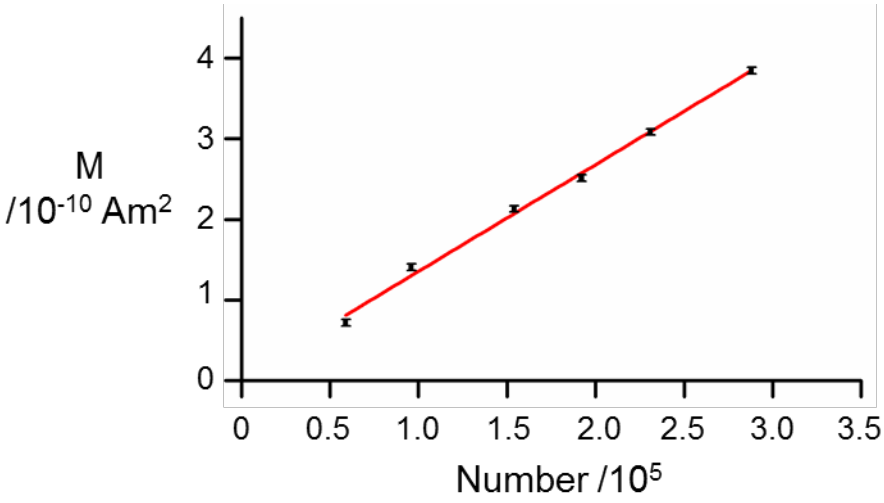


Figure 3.16 Calibration curve of magnetization vs. the number of magnetic particles.

A significant feature of our force spectra is that they are much narrower than the results obtained by AFM. This difference may be due to two possible reasons. One is that FIRMS simultaneously measures a large number of bonds. As described in the above paragraph, based on the magnetization value of $1.29\pm0.04\times10^{-10}$ $Am^2$ and the magnetization calibration curve of the magnetic particles, we calculated that $9.5\pm0.6\times10^4$ bonds underwent dissociation (Figure 3.16). This number is approximately two orders of magnitude higher than the typical number of events measured by single-molecule techniques such as AFM. Another possible reason could be the labelling with microparticles. Similar to our narrow force-induced dissociation, sharp melting profiles have been observed, in which DNAs were labelled with gold nanoparticles [92]. Further investigation is needed to clarify this effect by using magnetic particles with different sizes and size distributions.

### 3.4.5 Detection of multiple DNA interactions

The well-defined binding force with an ultra-narrow distribution makes it possible to distinguish different DNA interactions for very similar sequences. To demonstrate the unprecedented resolving capability, we made a 1:1 mixture of the two probing strands used in Figure 3.8 to form both the 12-bp and 11-bp DNA duplexes with the common target strand. Two distinct decreases were obtained (Figure 3.17). The plateau between the two transitions is located at 50% $M/M_0$, consistent with the ratio of the two probing strands [Figure 3.17 (a)]. The corresponding FIRM spectrum in Figure 3. 17 (b) shows fully resolved two peaks.

Compared to a previous AFM study with single bp resolution [91], our work is able to directly reveal different DNA interactions without using a sophisticated model for data analysis. Different DNA interactions are also quantitatively obtained. The ability to resolve different DNA interactions in a single sample will allow FIRMS to be employed in biochemical research that involves multiple DNA interactions.

### 3.4.6 Dependence of the dissociation force on the mismatch position

High-resolution force spectroscopy also provides accurate force measurements to aid in the theoretical modelling of DNA interactions. We studied two more probing strands, with sequences 5′-CCC AGA AAA CCC-3′ and 5′-CCC AAG AAA CCC-3′, respectively, in addition to the 9th-mismatching strand. These two strands differ from the 9th-mismatching strand only in the position of the mismatched base G. We called the two strands the 8th-mismatching and the 7th-mismatching strands, respectively.

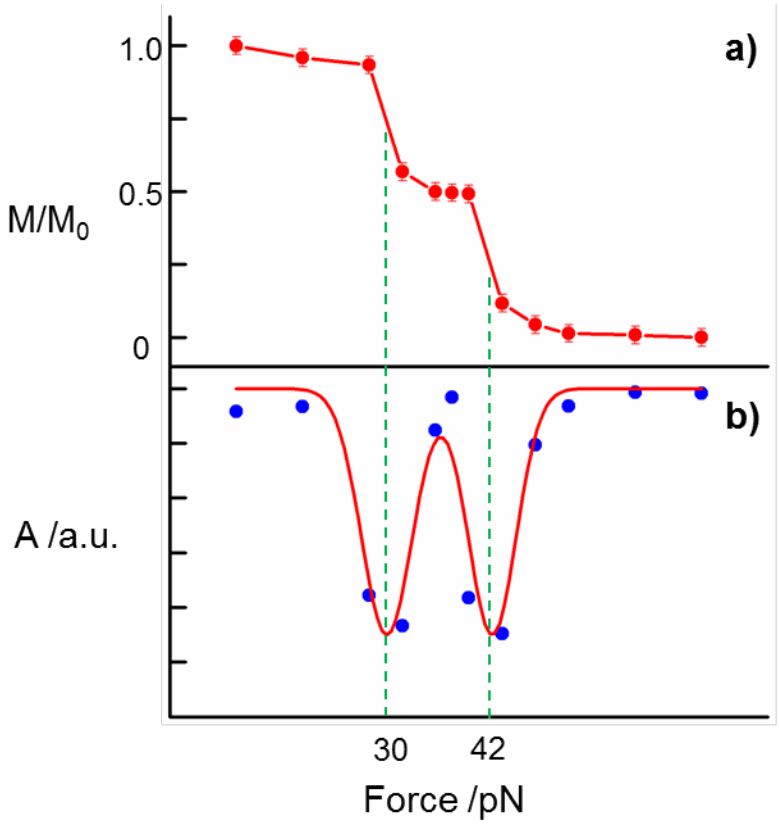


Figure 3.17 Resolving the binding forces of two different DNA duplexes with only one - base pair difference. (a) Relative magnetization vs. calibrated external mechanical force. (b) The corresponding FIRM spectrum.

The force measurements in Figure 3.18 show that the binding forces of the 8th-mismatched and 9th-mismatching 11-bp duplexes are the same, while the binding force of the 7th-mismatching duplex is slightly lower. From the transitions at 800 rpm for the 8th-mismatched and 9th-mismatching duplexes and at 750 rpm for the 7th-mismatching duplex, we deduced the binding force of the latter to be $30\times(750/800)^2 = 26$ pN, which is 4 pN lower than the binding forces of the other two strands.

To verify the small binding force difference between the 7th-mismatching duplex and the 8th-/9th-mismatching duplexes, we used centrifugal force to directly obtain the binding force of the 7th-mismatching duplex (Figure 3. 19). From the fitted peak position of 2510 rpm, the binding force is calculated to be 26 pN, consistent with the force value obtained previously. This result confirms the small thermodynamic difference of the 7th-mismatching duplex compared to the 8th-/9th-mismatching duplexes.

To quantitatively correlate our measured binding forces with thermodynamic parameters, we calculated the $\Delta G$ for the duplexes involved in this work. They were -13.29 and -10.97 kcal/mol for the 12-bp and 9th-mismatching 11-bp, respectively [93]. The 12 pN difference in binding forces and 2.32 kcal/mol difference in $\Delta G$ between the two duplexes match well with thermodynamic prediction in which 13 pN force corresponds to ~2.2 kcal/mol energy [94]. However, although the $\Delta G$ values are identically -10.24 kcal/mol for both the 8th-mismatching and 7th-mismatching 11-bp duplexes based on the nearest-neighbor model [93], their binding forces differ by 4 pN. This might be attributed to the slightly different $\pi$ stacking in the two duplexes, which involves more than just the nearest basepairs [95, 96]. For example, in the 8th-mismatching duplex there is four consecutive T-A pairs, which does not exist in the 7th-mismatching duplex.

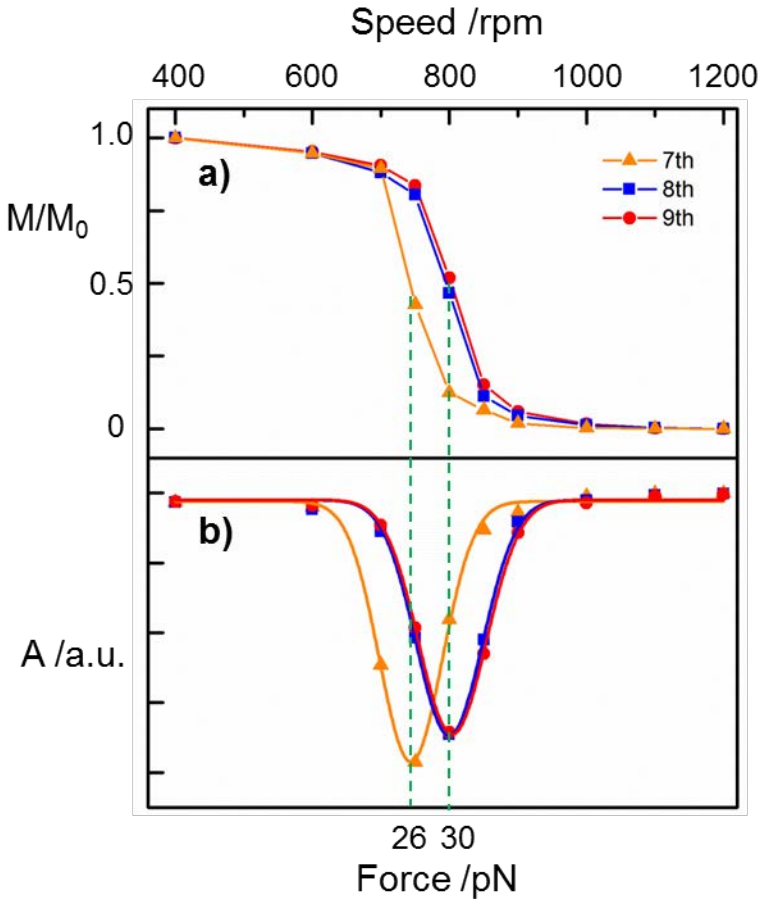


Figure 3.18 Binding forces of three DNA duplexes that differ only at the position of one base. (a) Relative magnetization vs. calibrated external mechanical force. (b) The corresponding FIRM spectra.

Xia et al. reviewed duplexes with identical nearest-neighbor basepairs but different thermodynamic stabilities, and proposed an expanded nearest-neighbor model to predict thermodynamic parameters more precisely [97]. Our results of precise force measurements support the necessity of a more accurate model.

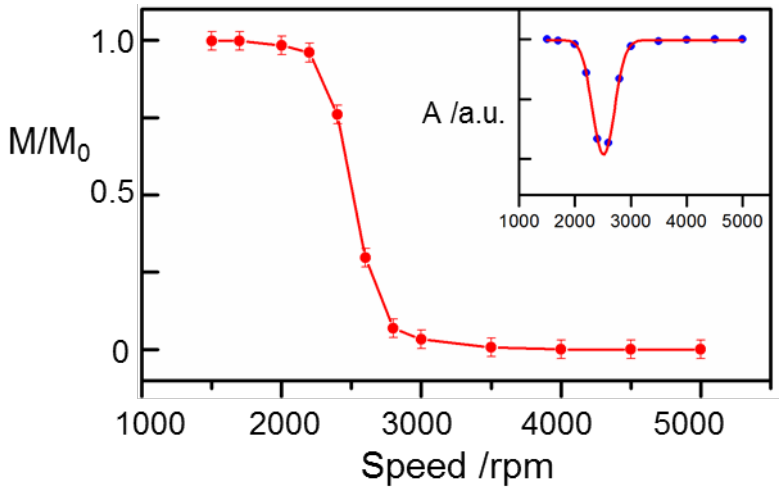


Figure 3.19 Relative magnetization vs. centrifuge speed for dissociating the 7th-mismatching 11-bp DNA duplex. Inset shows the corresponding FIRM spectrum, with a peak position of 2510 rpm from Gaussian fitting. A: amplitude.

The FIRMS technique uses different magnetic properties of the tagged magnetic particles to identify bound and dissociated states. This unique technical feature allows us to noninvasively probe and resolve different molecular interactions, which is an advantage over AFM. However, AFM is able to provide dynamic conformational changes of the bound molecules during stretching, whereas FIRMS detects only the initial bound state and the final dissociated state. We also compare FIRMS to other techniques, for example, optical microscopy. One advantage for magnetic-based FIRMS is that the sample system does not need to be perfectly transparent, which is required for optical-based techniques. In addition, the magnetic property difference clearly indicates the molecular binding states.

Rebinding of the dissociated magnetic particles is unlikely because the dissociated particles are physically removed from the reaction area by the mechanical force. In addition, the Brownian relaxation time of the magnetic particles is shorter than 1 s [98].

In this chapter, we presented well-defined, sequence-specific binding forces for DNA duplexes, using the FIRMS technique. The force distribution is as narrow as 1.8 pN. This feature enables resolving multiple DNA bindings that differ only in one base within the same sample. The high force resolution also reveals DNA binding forces depend on the position of the mismatching base. This work shows FIRMS is capable of resolving different DNA-DNA interactions and protein-DNA/RNA bindings in biological processes in future studies, as well as characterizing the binding strength of DNA-based exotic materials.

It should be noted that the most of the material presented in this chapter is appeared in the reference [103]. FIRMS technique described in this chapter used shaking and centrifugal forces to dissociate the magnetic particles. Our main focus is using FIRMS technique in molecular spectroscopy and imaging. In order to strengthen our work we need a better source for mechanical force. In the next chapter, we use acoustic radiation force generated by ultrasound as a new mechanical force for dissociating magnetic particles in FIRMS.

# Chapter 4

# Characterization of Molecular Interactions by Ultrasound

In this chapter, we present the application of acoustic radiation force, which is produced by extremely-low power ultrasound waves, in the FIRMS technique. This chapter is composed of motivation of the study, thermal and non-thermal effects of ultrasound, resolving binding forces of different antibody subclasses, and binding forces of DNA duplexes with a single base-pair difference.

## 4.1 Motivation of the study

In the previous chapter we presented the characterization of noncovalent binding in DNA duplexes by the FIRMS technique. In the aid of shaking and centrifugal forces we were able to resolve the binding forces of DNA duplexes with single base-pair difference. In addition, we resolved multiple DNA interactions, in which only the locations of the mismatching base-pair were different. Thus FIRMS is a very valuable technique in resolving noncovalent bonds.

Noncovalent molecular binding is a major pathway for molecular recognition in chemical and biological processes [87, 99]. The resulting bonds are usually specific to molecular structures, including antibody subclasses and DNA sequences, with characteristic binding strengths. Current research has primarily focused on characterizing these molecular bonds. Representative techniques include atomic force microscopy (AFM) [72, 100, 101], optical tweezers (OT) [77, 102], and our recently developed force-induced remnant magnetization spectroscopy (FIRMS) [22, 23]. However, noninvasive control of molecular binding remains a challenge: AFM is a single-molecule technique and requires the molecular system to be directly attached to the force medium; the OT technique is also based on single molecules and has a relatively small force range; and FIRMS currently uses shaking or centrifugal forces that are difficult to implement for direct bond manipulation [103].

Therefore, a new source of mechanical force is needed for applying the FIRMS technique in molecular imaging. This new force should be able to be implemented for direct bond manipulation. One possible candidate is acoustic radiation force (ARF) generated by

ultrasound radiation [104]. Here we present the ARF coupled FIRMS in recognition of binding forces of antibody subclasses and DNA Duplexes.

## 4.2 Thermal and non-thermal effects of ultrasound

Any sound of a frequency is greater than the upper limit of human hearing is defined as ultrasound. Typically the frequency range is in between 16 kHz and 10 MHz [105, 106]. Ultrasound has wavelength of 0.01-10 cm and velocity 1000-1600 m/s in liquid [107]. This large frequency range of ultrasound can be divided into two main areas as shown in Figure 4.1. The first one is “high frequency (or diagnostic) ultrasound” or “low power ultrasound”, which is concerned with the physical effects of the medium on the wave. This area is typically from 2 to 10 MHz, and is used in medical imaging, SONAR and non-destructive materials testing. The second area is known as “low frequency ultrasound” or “power ultrasound”, and lies between 20 to 100 kHz. It is used in a variety of applications such as cleaning, plastic welding and recently for sonochemistry. The frequency range available for sonochemistry has been extended to 2 MHz with the development of high power equipment [108].

Interaction of the ultrasound with a medium can occur through either thermal or non-thermal physical mechanisms. The absorption of ultrasound by a medium results in the conversion of ultrasonic energy to heat that leads to thermal effects. Ultrasound-induced temperature increasing is dependent on several factors, including medium properties, e.g., absorption coefficient, density, and ultrasound exposure parameters, e.g., frequency, and pressure amplitude.

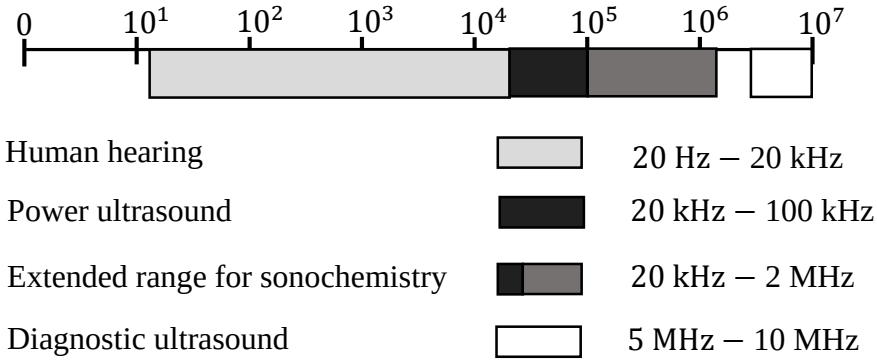


Figure 4.1 The frequency ranges of ultrasound.

Ultrasound-induced effects can also occur through non-thermal mechanisms. Acoustic cavitation is the most widely studied non-thermal mechanism. [109]. Acoustic cavitation is due to the interaction between a sound field and a gas bubble. Sound is transmitted through a medium by inducing vibrational motion of the molecules through which it travels. Thus in a liquid medium, ultrasound propagates via a series of compression and rarefaction waves induced in the molecules of the medium. At sufficiently high power the rarefaction cycle may exceed the attractive forces of the molecules of the liquid and cavitation bubbles will form. Such bubbles grow by a process known as rectified diffusion. The bubbles grow over the period of a few cycles to an equilibrium size for the particular frequency applied. These bubbles collapse in succeeding compression cycles which generates energy for chemical and mechanical effects. In aqueous systems, each cavitation bubble collapse occurs adiabatically to create localized "hotspot" generating temperature of about 4,000 K and pressure in excess of 1000 atmospheres. In aqueous solutions, water vapor molecules and volatiles inside cavities are thermolysed to generate highly reactive hydroxyl, hydrogen and organic radical species [106, 110]. The generation

of these radicals results in either intensification of the chemical reactions or the propagation of certain reactions under ambient conditions thus leading to sonochemistry [111, 112]. The main physical effect associate with acoustic cavitation is formation of high shear forces around the collapsed bubble. These mechanical forces are used to induce the breaking and formation of covalent chemical bonds [113].

Many factors affect the acoustic cavitation such as temperature, ultrasound intensity (irradiation power), ultrasound frequency and solvent. To achieve the cavitation threshold a minimum intensity is required. Figure 4.2 shows the variation of ultrasound intensity versus the threshold frequency for aerated water and air-free water [114].

In addition to the acoustic cavitation, other non-thermal effects mainly result from radiation forces that are associated with ultrasound propagation. A steady, time-average force typically acts upon an object in an acoustic or sound field. This force is known as acoustic radiation force (ARF), which results from a transfer of momentum from the sound field to the object. The magnitude of the radiation force depends on characteristics of both the sound field and the object.

Ultrasound-induced chemical and physical effects described above have led to many applications in research and industry. For examples, ultrasound radiation has been commonly used for cleaning, extracting biological entities from cells, and medical imaging [115,116]. Recently, its application scope has been extended to organic chemistry to promote the synthesis of target products [117,118]. Polymers containing a weak bond in the central portion can be selectively dissociated [119, 120]. Despite these wide-range applications, there have been no reports on the use of precisely controlled ARF for mechanical manipulation of noncovalent bonds.

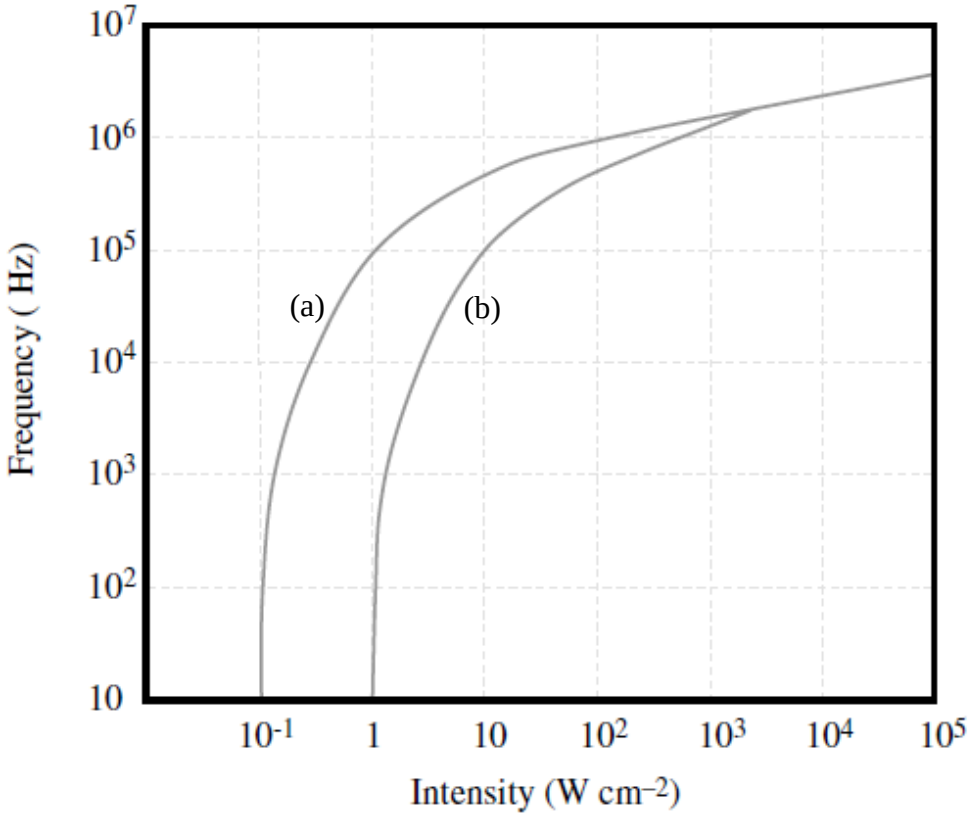


Figure 4.2 Variation in threshold intensity with frequency for (a) aerated water and (b) air-free water. Adapted from reference [114].

In our experiments, we use ARF as a mechanical force in order to dissociate magnetic particles selectively [109]. Because we only use ultra-low power ultrasound, no cavitation occurs under our experimental conditions. Consequently, no chemical and physical effects associated cavitation arise. The frequency we use is 20 kHz.

## 4.3 Resolving noncovalent bonds by ARF coupled FIRMS

Here, we report that ARF, produced by extremely low-power ultrasound radiation and mediated by magnetic particles, can selectively dissociate noncovalent bonds

according to their different binding strengths. The transducer is not immersed in the sample, which paves the way for noninvasive control of molecular binding. The principle is illustrated in Figure 4.3.

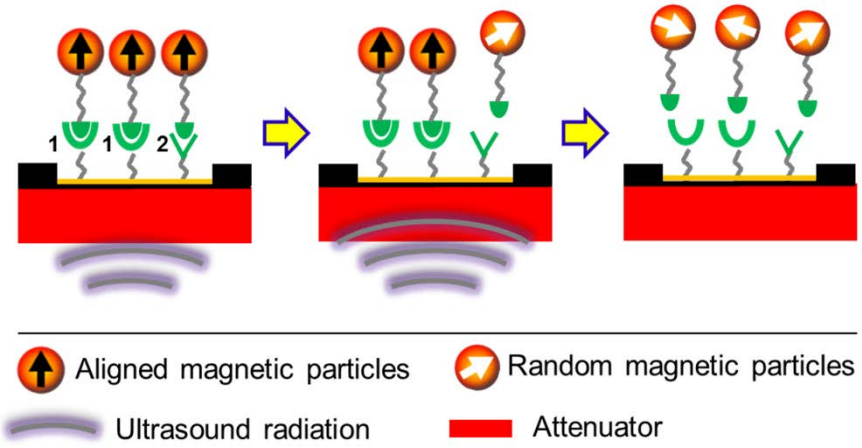


Figure 4.3 Principle of the ARF-based FIRMS technique for selective dissociation of noncovalent molecular bonds. 1 and 2 indicate two different types of receptors on the surface.

The sample well contains multiple types of noncovalent bonds with various abundances. Two types of bonds are shown as an example. One bond occurs between a magnetically labelled ligand and receptor 1. The other bond occurs between the ligand and receptor 2, which is assumed to have a weaker binding force than the former. When low-power ultrasound radiation is applied, the resulting ARF exerted on the magnetic particles will only dissociate the weaker bonds between the ligand and receptor 2. The dissociated magnetic particles will yield a decrease in the magnetic signal because of the randomization of their magnetic dipoles. This is the basis of the FIRMS technique [23]. Then, a stronger ARF produced by a slightly higher-power ultrasound can dissociate the stronger bonds between the ligand and receptor 1. The process can be repeated until all noncovalent bonds

are resolved based on their binding forces, which will be indicated by a zero magnetic field.

In order to resolve noncovalent bonds we have chosen two molecular systems. The first one is a system of protein A binding with three mouse IgG subclasses: $IgG_1$, $IgG_{2b}$, and $IgG_{2a}$. These three immunoglobulins are noncovalently bind to the protein A with different affinities. The order of the IgG antibodies represents their increasing binding strengths for protein A [121]. The antibodies were immobilized on the surface, while protein A was conjugated to the magnetic particles.

The second molecular system is two DNA duplexes with 18 base pairs but having three and two mismatching base pairs, respectively. The overall difference between the two strands is one mismatch. These two duplexes have much lower melting point difference than the two used in Chapter 3 (11-bp and 12-bp). In order to show the greater resolving capability these two duplexes were chosen.

## 4.4 Experimental Section

Schematic of the experimental set up is shown in the Figure 4.4. A rubber spacer is applied in between the sample and sonication probe in order to attenuate the ultrasound power. Two screws from the top are used to fix the sample on the attenuator, so the bottom of the sample makes good contact with the sonication probe covered by the attenuator.

### 4.4.1 Binding of Protein A with mouse IgG subclasses

For each protein A-IgG experiment, a $2\times4\times3$ $mm^3$ sample well was prepared, with the bottom surface coated with streptavidin via streptavidin-biotin interaction. Then, a 0.1

mg/mL solution of biotinylated antibodies (mouse $IgG_1$, mouse $IgG_{2a}$, and mouse $IgG_{2b}$, from Thermo Scientific) was pipetted into the sample well and incubated for 1 hr. After rinsing with a PBS solution (0.05% Tween-20), the sample was immersed in a 1% (w/w) solution of the blocking agent bovine serum albumin (BSA) for 1 hr. Protein A-coated magnetic dynabeads (Invitrogen) were then added and incubated for 2 hr.

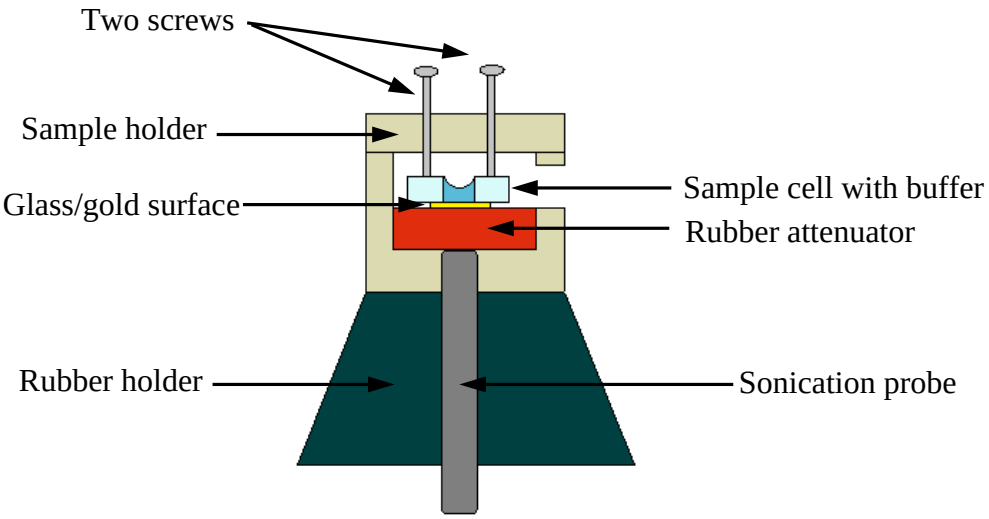


Figure 4.4 Schematic of the experimental apparatus.

### 4.4.2. Hybridization of DNA

The common strand of the sequences, 3´-GGG TTT TTT TTT TTT GGG-5´, was immobilized on the gold-coated surface via thiol-gold bonds. The respective second strands (5´-CCC GGG AAA AAA AAA CCC-3´ and5´-CCC GGA AAA AAA AAA CCC-3´), which were biotinylated, were then added to the sample well for incubation. Streptavidin-coated magnetic particles (M280, Invitrogen) were then added to bind to the second

strands. The remaining experimental parameters are the same as previously described in chapter 3.

### 4.4.3 Detection of the magnetic signal of samples

The samples were magnetized by a permanent magnet for 2 min before measurement. The initial magnetic signal, $B_0$, was then obtained by a Cs atomic magnetometer. The atomic magnetometer had a sensitivity of approximately 100 fT/(Hz)$^{1/2}$. After applying either ARF or centrifugal force with various amplitudes, the magnetic signal of the sample, $B$, was measured and normalized to the corresponding $B_0$. The ARF was applied by a modified commercial sonicator, Q55 from Qsonica (Newtown, CT, USA).

## 4.5 Results and Discussion

### 4.5.1 Modification and power calibration of a sonicator

A commercial sonicator, Q55 from Qsonica (Newtown, CT, USA), was modified by replacing the power-adjusting potentiometer (1 turn, 10 kΩ) with a more precise potentiometer (10 turns, 10 kΩ). Therefore, the output power can be more precisely tuned. The position of the potentiometer gives the relative output power, based on information from the manufacturer. An ultrasound transducer with a diameter of 6.5 mm was placed underneath the sample well. A rubber spacer was placed between the transducer tip and the sample well to attenuate the ultrasound power. The duration for each power was 30 s.

The ultrasound power was quantified by a thermal method, which measures the

power as heat absorbed by a fixed volume of liquid [122]. Here, a sample well was filled with 16 µL of buffer. The buffer temperature was measured by a thermal controller (CN9000A, Omega) with ±0.1 ºC accuracy. The average power was calculated from the equation,

$$\text{Power} = \frac{mC\Delta T}{t}. \tag{4.1}$$

where $m$ is the mass of the buffer, $C$ is the heat capacity of water which is considered equal to that of the buffer, $\Delta T$ is the temperature change, and $t$ is the ultrasound duration of 30 s. The error for the power measurements was calculated to be ±0.3 mW from the temperature uncertainty. The results are shown in Table 4.1, and the power density (intensity) results are plotted in Figure 4.5. The power density was calculated by dividing the measured power by the effective surface area of the cell. The radiation power density was in the range of mW/cm$^2$, with duration of 30 s.

Table 4.1. Power calibration of the attenuated ultrasound radiation

| Relative Output Power (%) | $\Delta T$ (°C) | Measured Power (mW) | Power Density (mW/cm$^2$) |
|---|---|---|---|
| 20 | 0.9 | 2.0 | 25 |
| 30 | 1.3 | 2.9 | 36 |
| 40 | 1.7 | 3.8 | 48 |
| 50 | 2.2 | 4.9 | 61 |
| 60 | 2.8 | 6.3 | 79 |

### 4.5.2 Resolving IgG subclasses binding to protein A

Figure 4.6 shows the results of the ARF-induced dissociation of each type of bond and their respective FIRM spectra, which were obtained by taking the derivative of the corresponding magnetic signal profile. The magnetic signals were detected by an atomic magnetometer (Chapter 2).

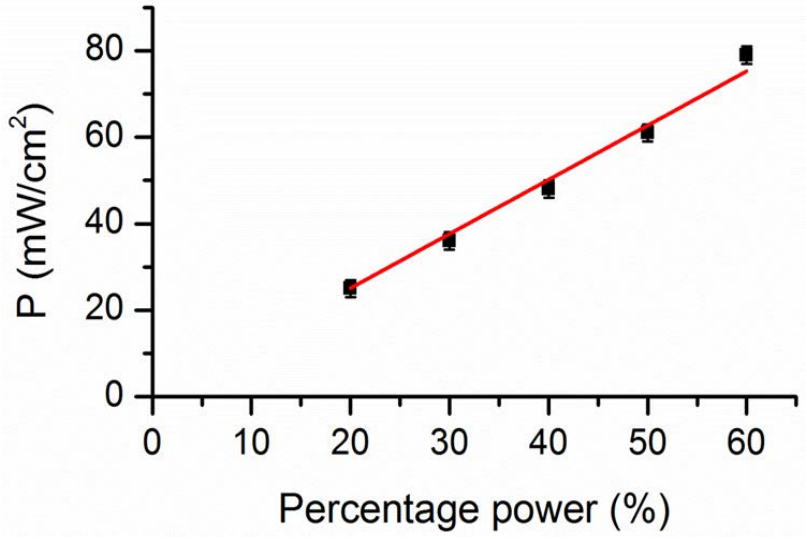


Figure 4.5 Power density calibration of the attenuated ultrasound radiation.

For an incremental power step of 3 mW/cm$^2$, the dissociation ultrasound powers for the three IgG-protein A bonds were found to be 22, 34, and 47 mW/cm$^2$, respectively. The different dissociation power values are consistent with the order of the binding strengths of the three IgG antibodies interacting with protein A. The results also indicate the capability of this technique to resolve different noncovalent bonds by adjusting the ultrasound power and hence the resulting ARF.

To demonstrate the resolving capability of ARF for different bonds, we applied more precisely adjusted ultrasound radiation to a sample well containing both $IgG_{2a}$ and $IgG_{2b}$ (Figure 4.7). The incremental power step was reduced to 1.5 mW/cm$^2$. Two-

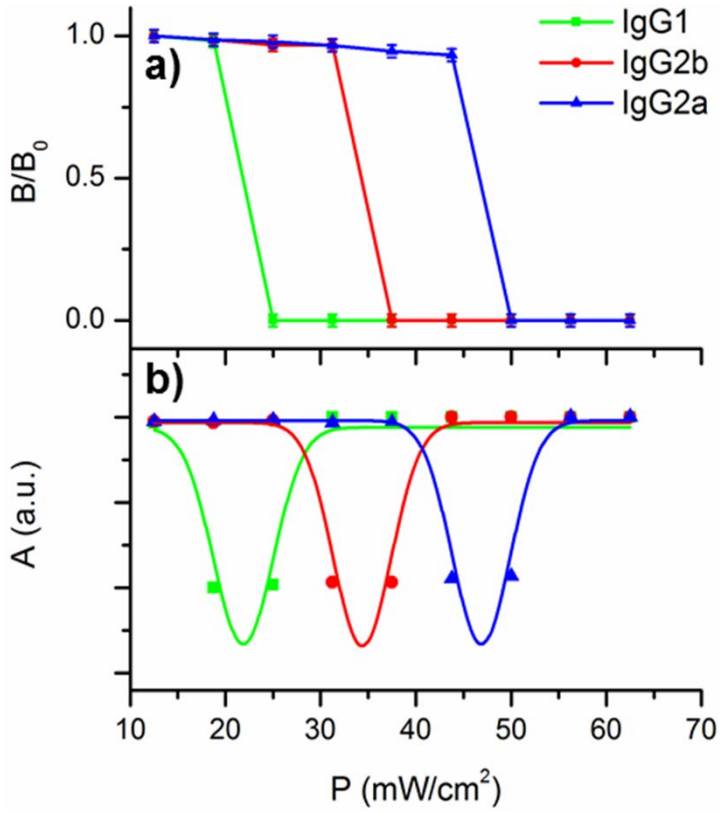


Figure 4.6 ARF-induced selective dissociation of protein A−mouse IgG bonds. (a) Relative magnetic signal as a function of ultrasound power for three different bonds. (b) Corresponding FIRM spectra for the profiles in (a).

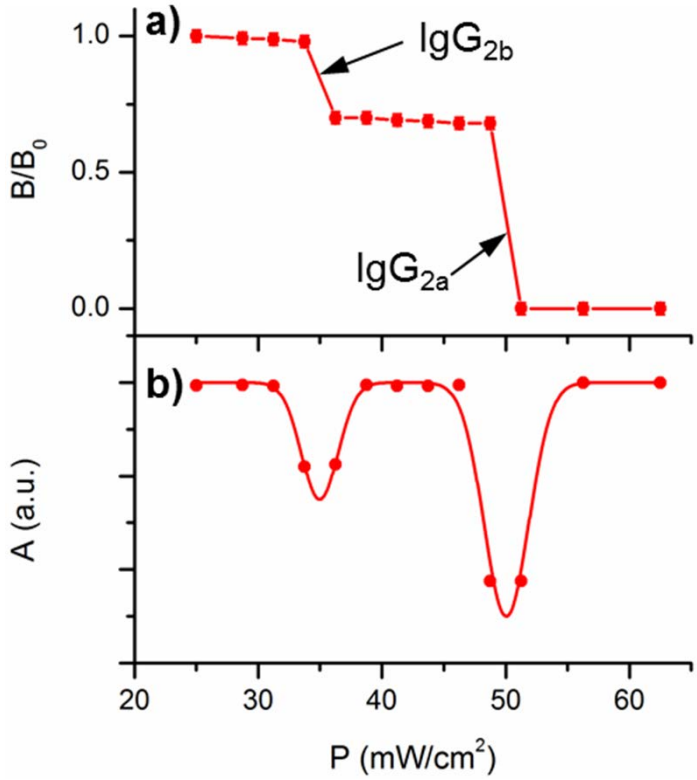


Figure 4.7 Resolving noncovalent bonds using ARF. (a) Magnetic signal profile of ARF-induced dissociation of protein A-$IgG_{2b}$ and protein A-$IgG_{2a}$ in a single sample. (b) Corresponding FIRM spectra of (a).

dissociations were observed, one at 35 mW/cm$^2$ and one at 50 mW/cm$^2$. Based on the individual studies presented in Figure 4.6 we attributed the former dissociation to the protein A-$IgG_{2b}$ bonds and the latter to the protein A-$IgG_{2a}$ bonds. Differentiation of the profile yielded a FIRM spectrum consisting of two well-resolved peaks (Figure 4.7 b). The peak positions represent the respective binding strengths, and the peak heights correspond to the respective abundances.

### 4.5.3 Measuring binding forces of protein A-IgG by Centrifugal force

The binding forces of the noncovalent bonds were obtained with FIRMS by employing a centrifugal force [83,103]. The binding force $F$ of each bond equals the centrifugal force at which the bonds undergo complete dissociation. Therefore,

$$F = m\omega^2 r \tag{4.2}$$

where $m$ is the buoyant mass of the magnetic particles, $\omega$ is the centrifugal speed in rad/s, and $r$ is the distance between the sample and the center of the centrifuge. The diameter of the protein A-coated magnetic particles was measured as 2.58±0.05 μm by scanning electron microscopy (Figure 4.8).

The particle density was determined to be 1.44±0.02 ×10$^3$ kg/m$^3$ by suspending the particles in a series of $Cs_2SO_4$ solutions with known densities. The density of the buffer was 1.0 kg/m$^3$. Therefore, $m$ = 4.0×10$^{-15}$ kg. For the centrifuge used in this work (Eppendorf 5417R), $r$ = 8 cm. Figure 4.9 shows that the dissociation speeds are 1600 rpm (revolutions per minute), 2600 rpm, and 3000 rpm for $IgG_1$, $IgG_{2b}$, and $IgG_{2a}$, respectively. Therefore, the binding forces were calculated to be 9, 24, and 32 pN for $IgG_1$, $IgG_{2b}$, and $IgG_{2a}$, respectively. These values correspond to 9±2, 24±2, and 32±3 pN for protein A

binding to $IgG_1$, $IgG_{2b}$, and $IgG_{2a}$, respectively. The force errors were based on the minimum increment of 100 rpm in the centrifugal speed.

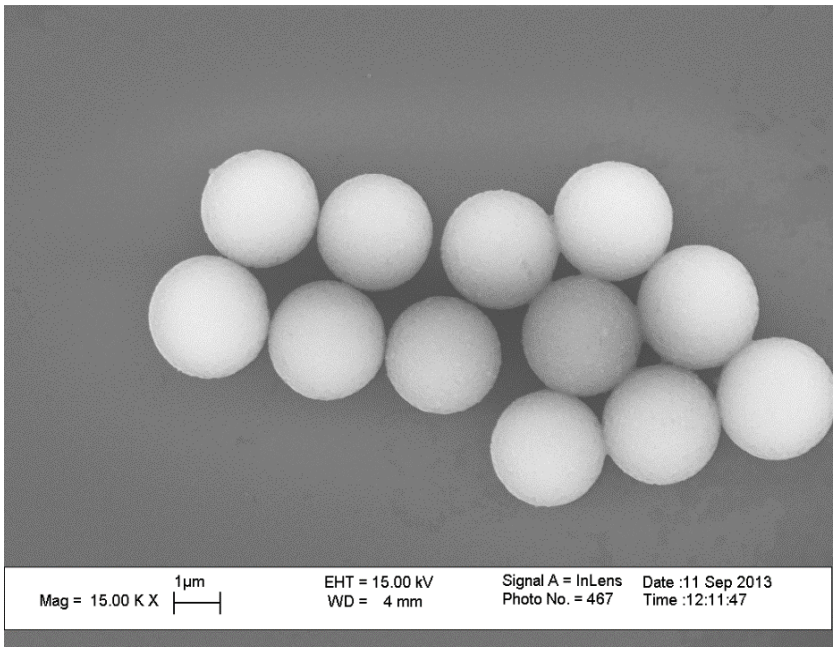


Figure 4.8 A representative SEM image of Protein A coated M280 magnetic particles.

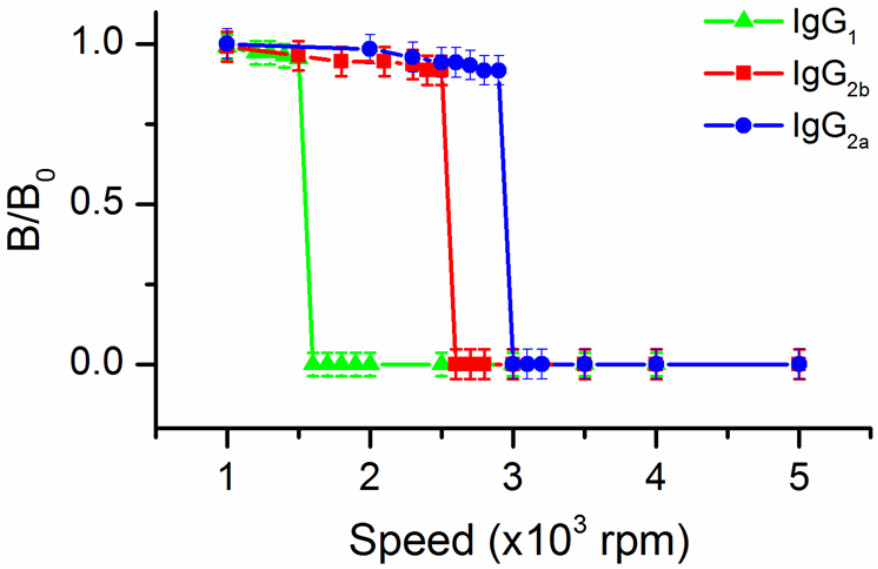


Figure 4.9 Magnetic field profiles of the dissociation of protein A-IgG bonds induced by centrifugal force.

The correlation between the binding force and the ultrasound power is plotted in Figure 4.10. Because exact calculation of the ARF is challenging [123], the use of bonds with well-characterized binding forces offers a viable scale for ARF calibration.

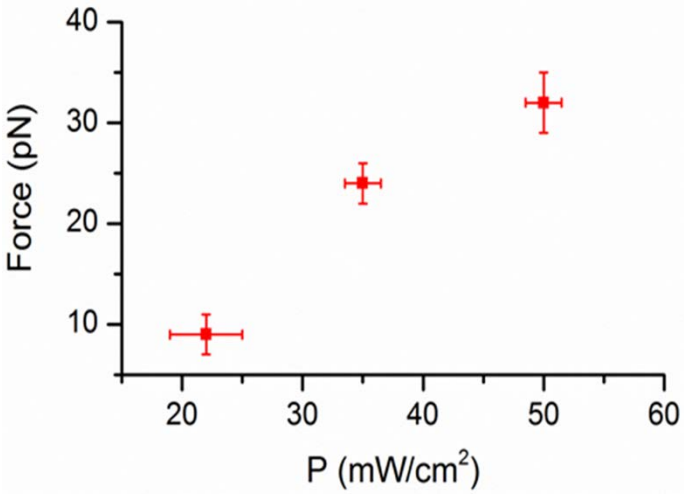


Figure 4.10 Correspondence of ultrasound power with the binding forces of noncovalent bonds.

We compare our application of ARF with other ultrasound applications in chemistry. First, the ultrasound power in this work is much lower than that of other methods [117-119]. The attenuation factor resulting from a 6.5-mm-thick rubber layer placed between the sample and the transducer is estimated to be 5600, by comparing the manufacturer-specified power and the attenuated power. In contrast, ultrasound-induced dissociation of covalent bonds typically requires two orders of magnitude higher power. Second, the duration of this application is only 30 s, compared to the several hours required in organic synthesis assisted by ultrasound. Third, the ARF was precisely tuned to selectively dissociate different molecular bonds, which has not been achieved in previous works. Coupled with a noninvasive scheme in which the transducer does not contact the sample, this work paves the way for mechanical control of molecular bonding.

The power used in this work is nearly an order of magnitude below the cavitation threshold for 20-kHz ultrasound radiation [124]. Therefore, the effects associated with cavitation can be excluded. In addition, due to the low power and short duration of our approach, the thermal effect in our experiments was minimal. For example, the dissociation power for $IgG_{2a}$, the highest of the three, was 50 mW/cm$^2$. This power corresponds to a mere 2.2 °C increase in the sample temperature.

### 4.5.4 Resolving DNA duplexes with single base-pair difference

To further illustrate the resolving capability of ARF for noncovalent bonds, we designed two DNA duplexes with only a 3 °C difference in melting temperatures using mfold software [125]. The two sequences are as follows:

Duplex 1: 3′-GGG TTT TTT TTT TTT GGG-5′

5′-CCC GGG AAA AAA AAA CCC-3′

Duplex 2: 3′-GGG TTT TTT TTT TTT GGG-5′

5′-CCC GGA AAA AAA AAA CCC-3′

The duplexes were designed such that the dissociation power remained low to avoid substantial thermal effects but was higher than that of protein A-$IgG_{2a}$ to expand the force range for studying more molecular binding systems. One of the strands in the duplexes was immobilized on the gold-coated bottom surface of the sample well, and the other was labeled with magnetic particles.

Figure 4.11 shows the results of ARF-induced dissociation of the DNA duplexes. The increment of the ultrasound power was 1.5 mW/cm$^2$. With such fine tuning, the dissociation power of the two DNA duplexes was well characterized.

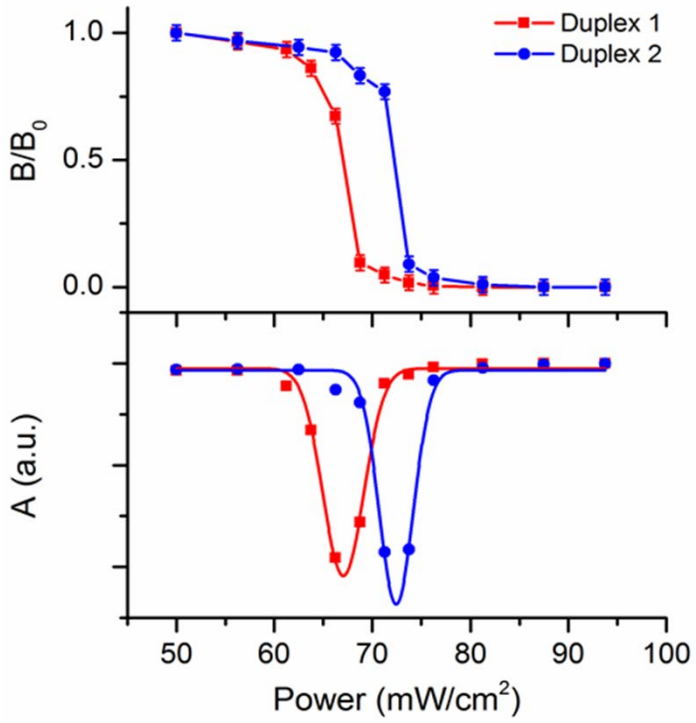


Figure 4.11 ARF-induced selective dissociation of two DNA duplexes. (a) Relative magnetic signal profiles as a function of ultrasound power. (b) Corresponding FIRM spectra of the profiles in (a).

For duplex 1, the dissociation power was 67 mW/cm$^2$, and for duplex 2, it was 72 mW/cm$^2$. The difference of 5 mW/cm$^2$ is substantially greater than the 1.5-mW/cm$^2$ uncertainty. Therefore, ARF can dissociate stronger noncovalent bonds and can still distinguish between them with high resolution. The difference of 3 °C in melting temperatures is significantly smaller than the difference of 7 °C between the two DNA duplexes that we previously reported for centrifugal force [103].

The binding forces of the duplexes were also measured using centrifugal force. The dissociation speeds were 5800 and 6000 rpm for duplex 1 and duplex 2, respectively (Figure 4.12). The streptavidin-coated magnetic particles used here have a buoyant mass of $4.6\times10^{-15}$ kg, as measured in a previous work [103] and $r$ = 8 cm. Therefore, the binding forces are 136 pN and 146 pN for duplex 1 and duplex 2, respectively. The higher binding forces demonstrate the wide application range of ARF-based FIRMS technique in resolving noncovalent bonds, which have typical binding forces between 10 and 150 pN [99].

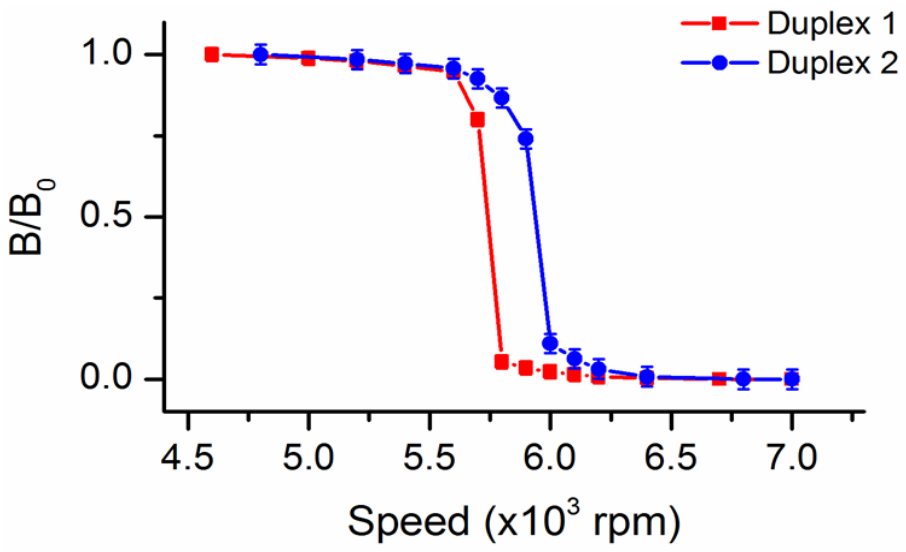


Figure 4.12 Magnetic field profiles of the dissociation of DNA duplexes induced by centrifugal force.

## 4.6 Towards integrating the ultrasound probe with the atomic magnetometer

The use of ARF for highly-selective bond dissociation represents a new branch of mechanochemistry. Compared to the previously reported shaking and centrifugal forces, ARF is advantageous in that the force generator can be integrated with the atomic magnetometer. The ultrasound probe is much smaller than either a shaker or a centrifuge, allowing it to be potentially placed inside the magnetic shield of the magnetometer. This implementation will eliminate the need for a manual sample transfer between the force application and signal measurement. The development of ARF-based bond dissociation also allows for the study of molecular interactions under conditions, for example in vivo, that cannot be employed in a shaker or centrifuge.

One unknown aspect of ARF is how the ultrasound frequency will affect the dissociation of noncovalent bonds. Frequency plays a role in both power reduction due to the attenuation and penetration of the ultrasound into the medium [126, 127]. Research related to this issue will be a topic for future studies.

The most of the material presented in this chapter is appeared in the reference [128]. Here we have shown that selective dissociation of noncovalent bonds can be achieved by ARF. The force produced by precisely adjusted ultrasound radiation is capable of resolving different antibodies and DNA duplexes. Due to their small size, ultrasound probes can be integrated with an atomic magnetometer. Consequently, ARF-based FIRMS will be capable of noninvasive mechanical manipulation of molecular interactions. The next chapter focuses on developing a new instrument in which ultrasound probe is integrated

with an atomic magnetometer for resolving noncovalent bonds in automated operation.

# Chapter 5

# Integrating Ultrasound Probe with an Atomic Magnetometer

In this chapter, the details and characterization of a compact and sensitive atomic magnetometer coupled with an ultrasound probe are presented. The resulting instrument offers several new features, including miniaturized footprint, improved applicability in molecular detection, and potential of multiplexed analysis.

## 5.1 Motivation of the study

In the previous chapter, we presented the application of FIRMS in resolving noncovalent bonds using the ARF generated by ultrasound. We were able to resolve the binding forces of different biomolecules including different antibodies and DNA duplexes with single base-pair difference [128]. Therefore ultrasound is a valuable source of mechanical force in order to use FIRMS for molecular diagnostics.

However, we still need some modifications for our instrument in order to improve detection efficiency. For example, currently we transfer samples manually between the force apparatus and magnetic scanning device back and forth for each force step. If we can consolidate these steps, the detection will be a more efficient and experimental error will be reduced. To achieve this goal, we have designed a new atomic magnetometer device in which an ultrasound probe with sample holder is placed inside the magnetic shield. The sample will move into the sample holder by a linear motor where acoustic radiation force is applied and the magnetic signal is measured subsequently.

This chapter focuses on developing a new atomic magnetometer device. In addition to the ultrasound probe integration, the instrument has some new features compared to our previous atomic magnetometers, such as implementing optical fiber and using a magnetic shield with much reduced size.

## 5.2 Ultrasound probe integrated atomic magnetometer for resolving noncovalent interactions

### 5.2.1 Configuration of the laser, sample and ultrasound probe

Figure 5.1 shows the main part of the instrument with basic arrangement of the ultrasound probe, sample and the Cs atomic sensor with the laser alignment. In order to detect the magnetic signal from the sample, the sensor should be placed as close to the sample as possible because magnetic fieldstrongly depends on the distance. On the other hand, ultrasound causes turbulence on the air because it travels through the air, which may cause substantial noise during signal detection. In order to avoid this issue we separate the Cs atomic sensor from the sample by using a plastic plate which is attached to a Teflon holder placed inside the inner most magnetic shield. This Teflon holder contains a set of coils wound around it to provide required magnetic fields and gradients for proper working of the Cs sensor.

The laser light, which is directed to the Cs sensor and reflected back from the sensor, passes through the upper port of the inner most shield. The sample is fixed on a ceramic rod,which is driven into the sample holder by a linear transducer (Ultra Motion, Cutchogue, New York, USA). A rubber spacer was placed in between the sample and the ultrasound probe in order to attenuate the ultrasound power. The details of all the components of the instrument are provided in the following sections.

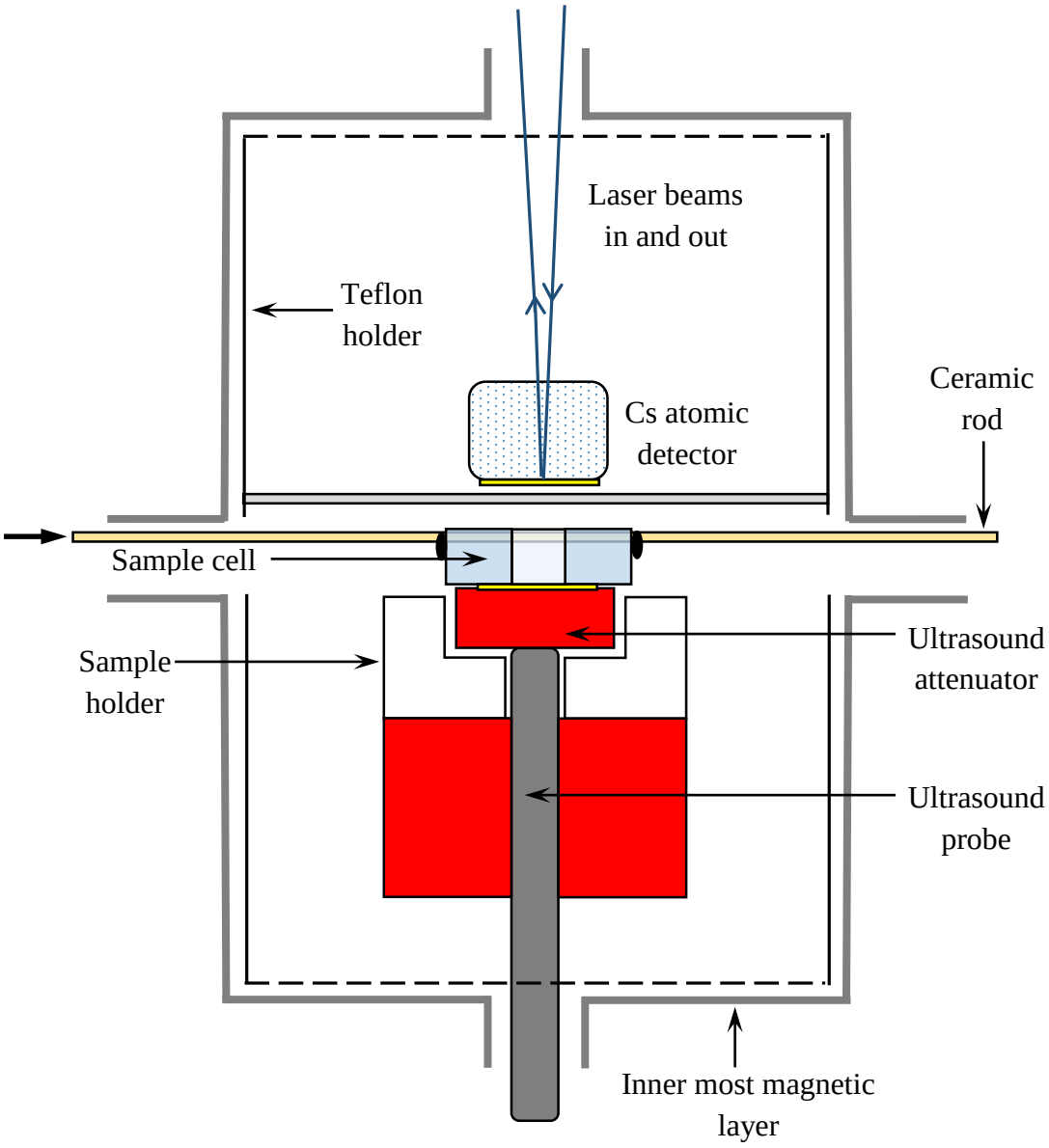


Figure 5.1 Schematic illustration of the configuration of the ultrasound probe, sample and Cs sensor with laser alignment. A rubber attenuator is placed in between the probe and the sample.

### 5.2.2 Laser control and optical layout

A diode laser (New Focus, model 7018) tuned to the D1 transition of Cs (894.95 nm) is used as the light source. The laser has two modes of operation: constant-power and constant-current modes. The constant-power mode results in lower intensity fluctuations and the constant current-mode results in narrower laser linewidth. We use the constant-power mode for all the measurements. The constant-current mode is used to obtain the absorption spectra of Cs.

Frequency of the laser is modulated by driving a piezoelectric transducer in the laser cavity with a function generator (Stanford Research DS345). Figure 5.2 shows the optical layout, which is much similar to the one described in Chapter 2. The main difference of the new optical layout is use of an optical fiber to transmit laser into the Cs atomic detector, which adds more compactness to the instrument. There are three major parts of the optical layout (Figure 5.2): power monitoring, wavelength monitoring and magnetic signal detection.

The laser beam is first attenuated by a neutral density filter. Two beam samplers (5%) are used for controlling the laser. Due to temperature, current and mechanical noises, the power and the frequency of the laser beam tend to drift from the original set value. Therefore power and frequency (or wavelength) monitoring of the laser are required.

#### 5.2.2.1 Power monitoring

The first beam sampler feeds a photodiode for power monitoring. The voltage output of the photodiode is amplified using an amplifier (Stanford Research System,

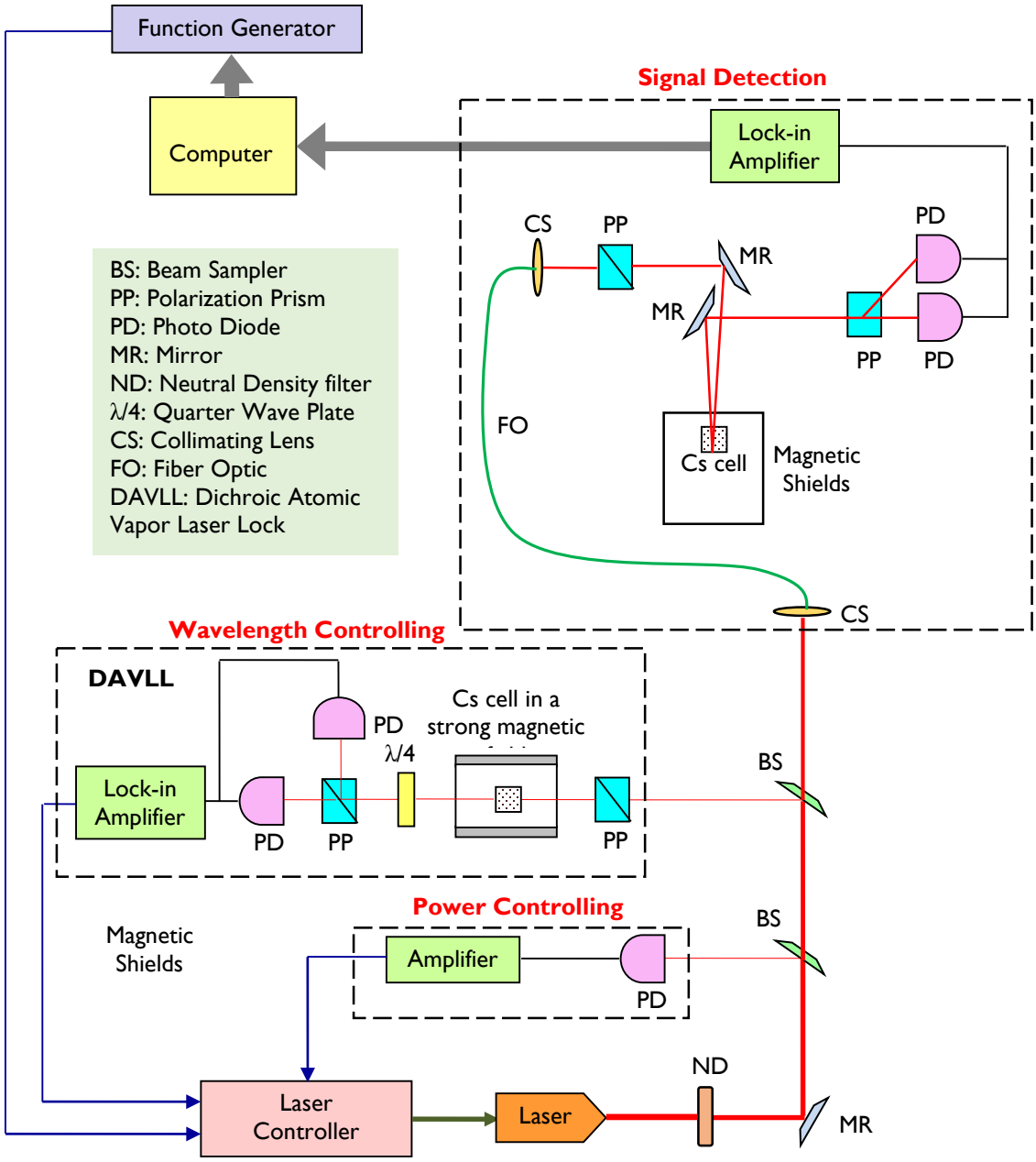


Figure 5.2 Optical layout of the instrument.

SIM900) and fed back to the laser through the laser controller for constant-power operation.

#### 5.2.2.2. Wavelength monitoring

The second beam sampler is used for a dichroic atomic vapor laser lock (DAVLL) for wavelength stabilization. DAVLL contains a Cs Atomic vapor cell placed in a high magnetic field, a quarter-wave plate and two polarization prisms. The light is first linearly polarized by using a Glan polarization prism. In the presence of a very high magnetic field, Cs atoms interact with the light beam to produce linear magneto-optical rotation. The resulting beam is passed through a quarter-wave plate and a Rochon polarization prism. The final beams are fed into two photodiodes and amplified by a lock-in amplifier (Stanford Research System, SR530).

As described in Section 2.1.2, linear magneto-optical rotation results from the difference in the refractive indices for the two circular components of linearly polarized light. In addition to the difference in refractive indices there is also difference in absorption of two circularly components. Both of these optical-rotation and absorption profiles (Figure 5.3) has a zero crossing point, which is suitable for locking the laser at optimal wavelength.

In our experiments, we use the optical rotation signal (by differential refractive indices) for locking the laser. After we lock the laser, any drift of the laser wavelength will shift the differential signal from the zero crossing point, which is detected by the lock-in amplifier and it feeds back a voltage signal to PZT. Once PZT obtained the voltage signal,

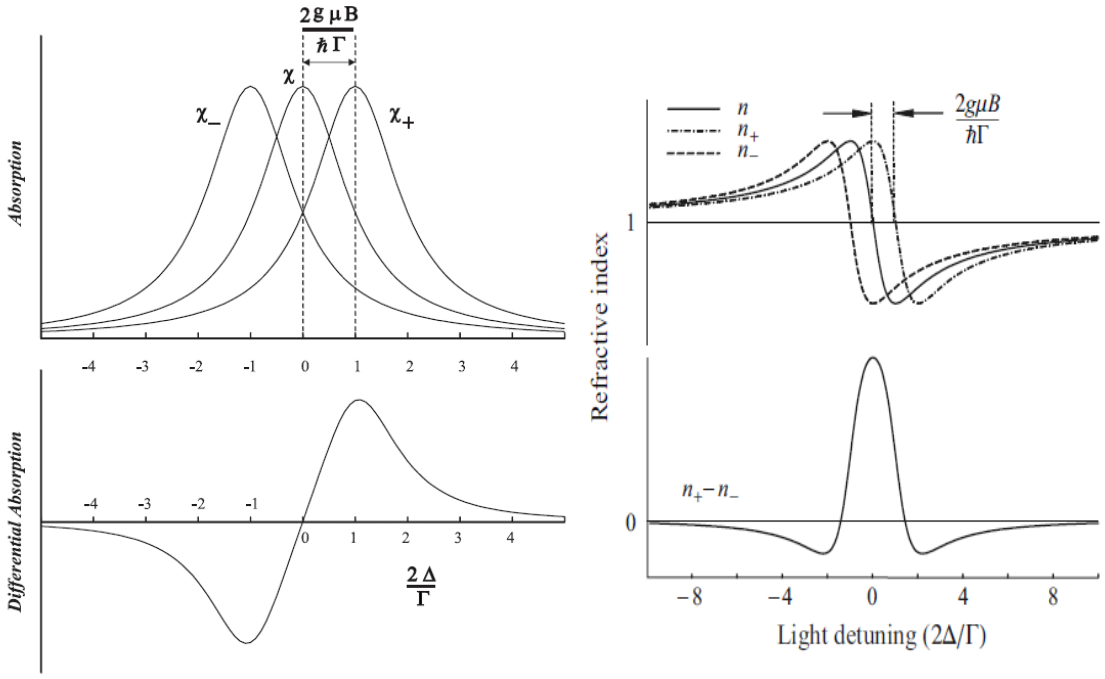


(a) (b)

Figure 5.3 (a) The upper trace shows the absorption curves of different circular components with the laser detuning. The lower one is the differential absorption signal. (b). The upper one is the plot of refractive indices of circular components with laser detuning. The lower trace is the differential refractive indices, where $(n^+ - n^-)$ is proportional to the optical rotation angle. Note that both differential curves has zero crossing point which can be used to lock the laser at optimum wavelength. The figures (a) and (b) are taken from the references [61], [129] respectively.

it tilts the mirror of the external cavity laser to adjust the wavelength back to the previous value.

The laser follows the Littman-Metcalf configuration to adjust the wavelength as shown in Figure 5.4. In this configuration, the first order diffraction beam goes to a mirror, which then reflects the beam back to the grating and into the diode laser as optical feedback. The laser tuning is achieved by varying the mirror angle but fixing the grating [131]. The angle of the mirror is adjusted by the attached PZT, which is operated by the voltage signal received from the DAVLL through the laser controller.

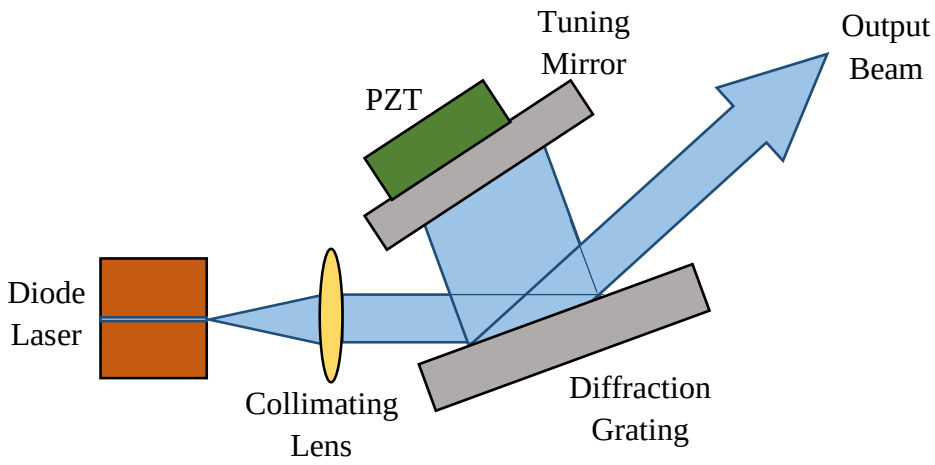


Figure 5.4 Littman-Metcalf configuration for adjusting diode laser wavelength. The PZT is attached to a reflecting mirror. Upon receiving the voltage signals, PZT varies the angle of the mirror to adjust the laser wavelength.

Figure 5.5 shows the Laser diode with optical system for power and wavelength monitoring. The metal box in the DAVLL system contains a strong magnet.

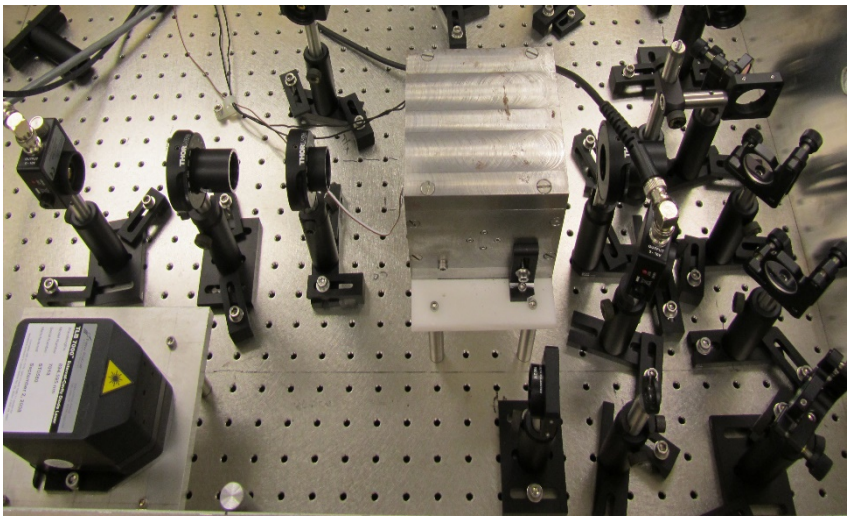

Figure 5.5 Laser diode with power and wave length monitoring optics

#### 5.2.2.3 Magnetic signal detection

After feeding the laser into power and wavelength monitoring, the rest of the beam passes through a fiber optic to reach the atomic sensor (Figure 5.6). This is a new component of our atomic magnetometers compared to the previous ones. It improves the compactness and portability of the magnetometer.

The output light of the fiber optic passes through a Glan polarizer to set the initial polarization of the beam (Fig. 5.2). A dielectric mirror is used to direct the beam into the Cs detector which is placed inside the inner most layer of the magnetic shields. Then, it hits an end mirror mounted at the back of the Cs cell holder and is reflected back to another mirror. The double pass-arrangement of the beam through the cell was chosen in order to increase the optical path (the rotation is additive on the two passes), which increases the sensitivity.

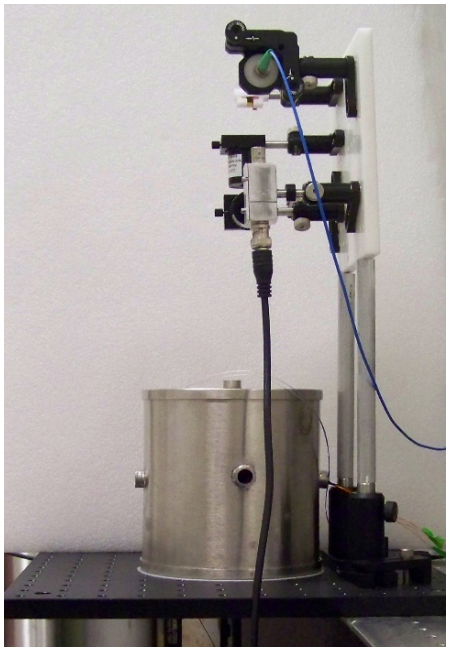

Figure 5.6 Signal detection part of the instrument. An optical fiber is used to couple the laser beam with the atomic sensor (inside the shield).

The second dielectric mirror directs the beam into Rochon polarizer oriented 45° to the initial polarization prism. This balanced polarimeter arrangement is sensitive to magneto-optical rotation induced by the Cs vapor. Two refracted beams from the polarizer feed into two photodiodes. (Figure 5.7) Due to the balanced polarimeter arrangement, the two intensities on the photodiodes are given by the following equations.

$$I_1 = I\,\mathrm{Sin}^2(\pi/4\ - \varphi) \tag{5.1}$$

$$I_2 = I\,\mathrm{Cos}^2(\pi/4\ - \varphi) \tag{5.2}$$

Here, $I = I_1 + I_2$ and $\varphi$ is the optical rotation angle. The rearrangement of the above equations results the optical rotation angle,

$$\varphi = \frac{I_1 - I_2}{2(I_1 + I_2)}. \tag{5.3}$$

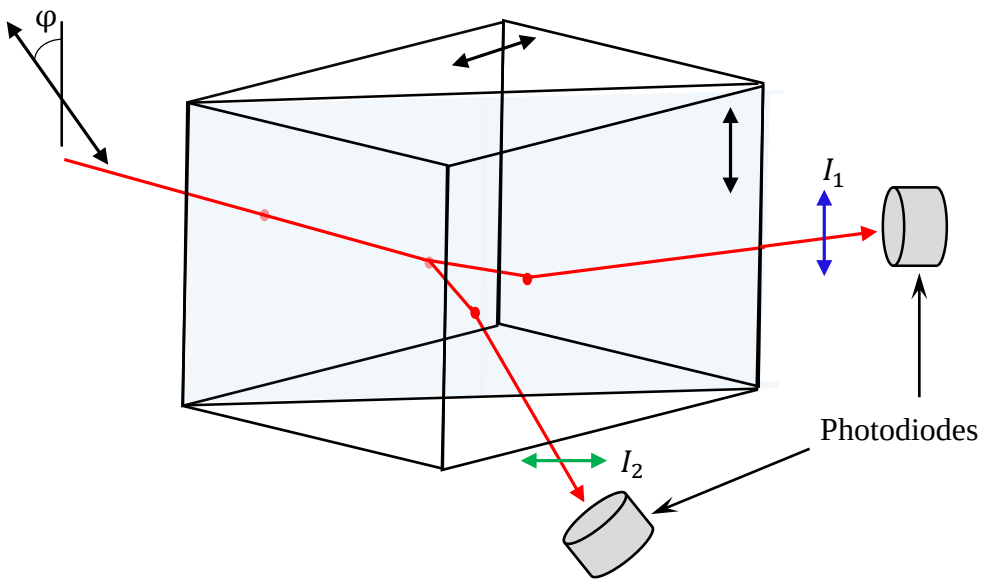


Figure 5.7 Detecting optical rotation by a Rochon polarizer.

### 5.2.3. Magnetic shield and internal coils

A four-layer magnetic shield is used in order to reduce the laboratory magnetic field (Figure 5.8). The shield was made of high-permeability alloy. Exposure to magnetic fields and mechanical stress are avoided to maintain the efficiency of the material. Each of the four layers consists of a cylindrical center piece and two removable end caps. Between the layers, silicone rubber foam is used to hold the shield in place, which also provides thermal insulation from the environment (Figure 5.9).

For each layer of the magnetic shield, four ports with 1 cm inner diameter are available on the cylindrical part and one each on the end caps. Two ports on the cylindrical parts are located from off center (Figure 5.8). One of them is used to hold a ceramic rod in which Cs atomic cell has mounted while the other one is used to carry all the internal coils out. The other two ports on the cylindrical part are aligned with the center, which are used

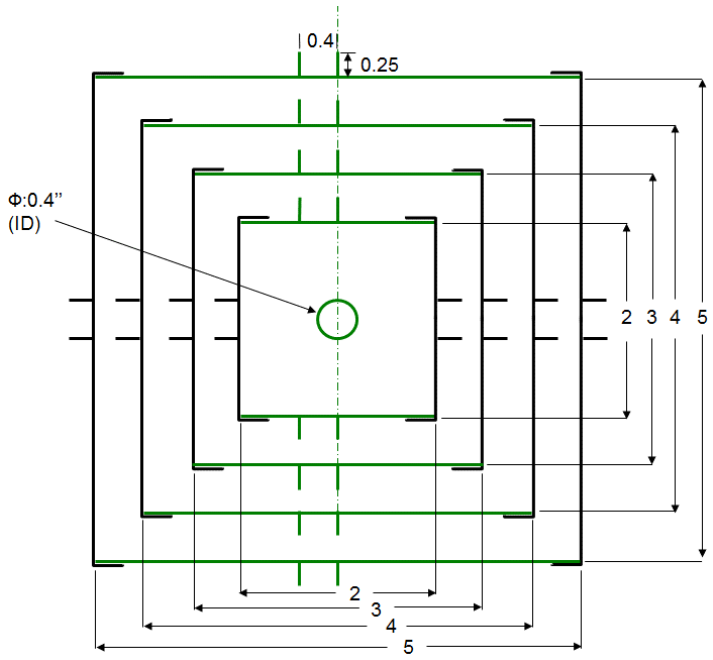


(a)

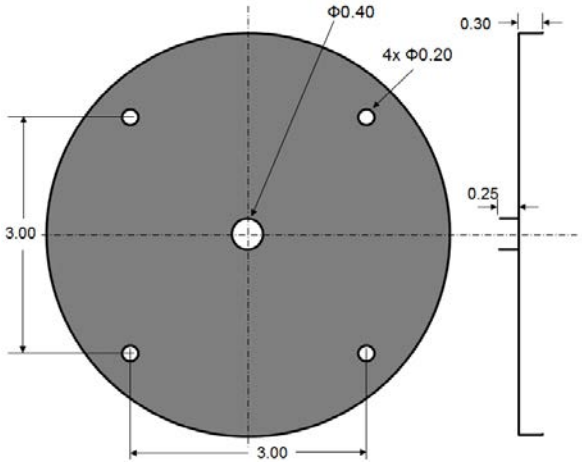


(b)

Figure 5.8 (a) Sideview of the magnetic shields. Two ports of the each cylindrical part are off-centered. (b) Face view of the outer most end cap. Four holes adjacent to the end are designed for mounting the shield on platform.

(a)

(b)

Figure 5.9 (a) Cylindrical parts of the magnetic shield. Silicone rubber foam is placed between each layer in order to hold the layers and provide thermal insulations. A Teflon cylinder which bears the coils is placed inside the inner most layer. (b) Four bottom end caps with rubber form. The outer most layer is attached to the platform via plastic screws. Ultrasound probe is fixed through the aligned ports of the end caps. A plastic tube is placed around the probe in order to avoid the contact between the probe and the magnetic shield. to scan the samples. All the ports on the end caps are aligned, respectively, among different

to scan the samples. All the ports on the end caps are aligned, respectively, among different layers during assembly and are used for optical access and inserting the ultrasound probe.

A set of coils are wound around a hollow cylindrical Teflon holder [Figure 5.10 (a)], which is placed inside the inner most layer of the magnetic shield. The technical design of the coil holder is shown in Figure 5.10 (b).These internal coils include a one Helmholtz coil, one Maxwell coil and four saddle coils (Figure 5.11). The Helmholtz coil is used to provide a bias magnetic field and the Maxwell coil is designed for providing a gradient field. The rest of the coils are for cancelling residual magnetic fields and gradients inside the shield.

The bias field (~ 185 nT) is directed along the ports on the end caps, defined as the *z*- axis, and parallel to the laser path. The sample magnetic field is much smaller compared to the bias field. The magnetometer is only sensitive to the magnetic field change along the *z*- axis. Current for the internal coils is provided via a resistor box with 0.2 ppm/°C stability.

### 5.2.4. Cesium atomic vapor cell

In our experiment, we use a (5 mm × 5 mm × 5 mm) glass cell that contains Cs atoms. Figure 5.12 shows a photo of the sensor with a U.S. penny to illustrate the dimensions. In order to minimize the relaxation of ground-state polarization due to collisions with the walls, the inner wall of the cell are coated with a layer of paraffin. The Cs cell is attached to a ceramic rod via its side arm. The cell is inserted into the shields through the ports on the cylindrical part of the shields. The ceramic rod is mounted outside the shield to allow fine adjustments from the outside.

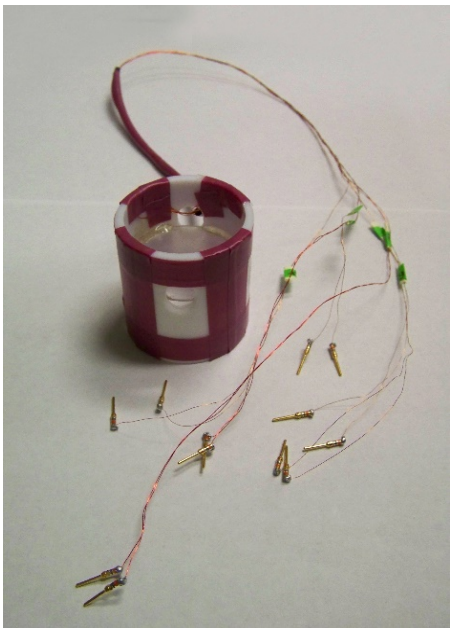

(a)

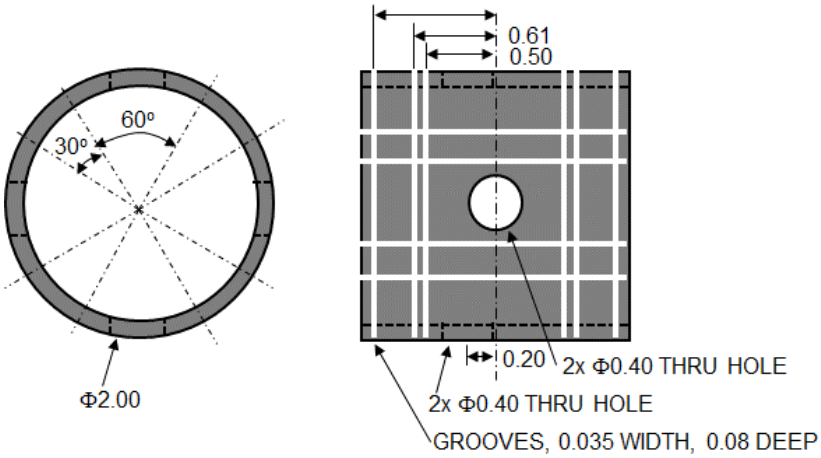


(b)

Figure 5.10 (a) Teflon coil holder. There is a plastic compartment in the center of the holder which separates the detector from the sample environment. (b) Technical design for coil holder.

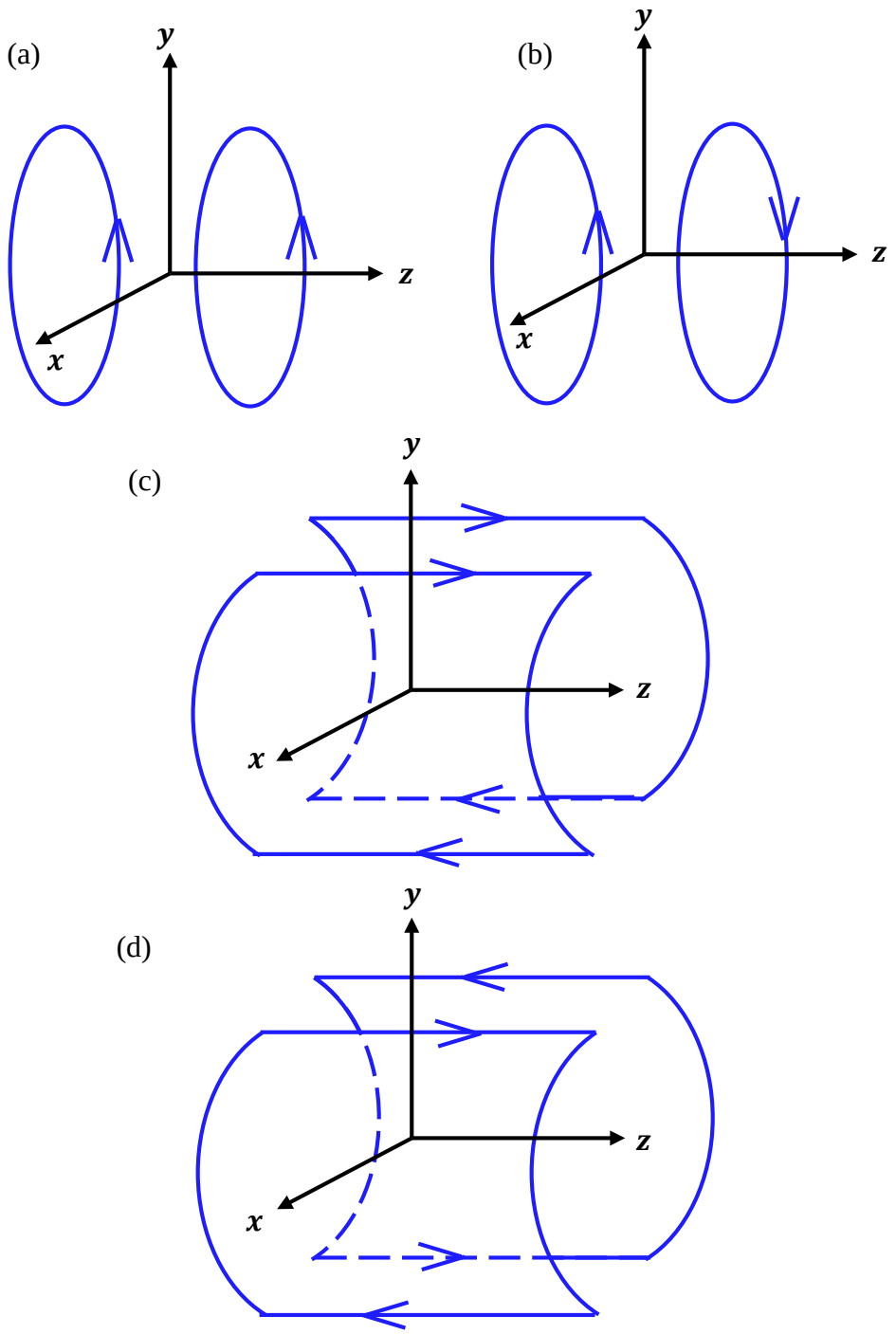


Figure 5.11 Configuration of coils. (a) Helmholtz coil for bias magnetic field in the $z$-direction (b) Maxwell coil for gradient magnetic field in the $z$-direction (c) Saddle coil for homogeneous magnetic field in the $x$-direction (d) Saddle coil for gradient magnetic field in the $x$-direction. A similar pair of saddle coils are used for the $y$-direction.

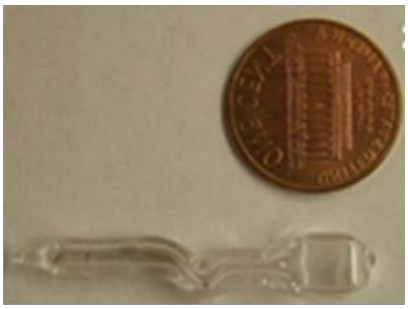

Figure 5.12 A photo of the Cs sensor with a U. S. penny.

The density of the Cs atoms is controlled by the operating temperature. The heating method should be carefully chosen because it may introduce overwhelming noise. We use a twisted Teflon-coated stainless steel wire wound around the outside part of the inner most cap of the magnetic shield (Figure 5.13). This heating method was found to be efficient and not to introduce significant noise, because the magnetic noise generated by the heating current is largely canceled and shielded by this configuration. A dc power supply is used to generate continuous heating. The upper limit of the cell temperature is restricted by paraffin's melting point, which is approximately 60 °C. In our experiments, the optimum cell temperature found to be 37 °C – 41°C for the best signal-to-noise ratio.

### 5.2.5. Ultrasound probe and the sample holder

The newest feature of our atomic magnetometer is the ultrasound probe. A low-power sonicator, Q55 from Qsonica (Newtown, CT, USA), is used. The sonicator was modified by replacing the power-adjusting potentiometer (1 turn, 10 kΩ) with a more precise potentiometer (10 turns, 10 kΩ). Therefore, the output power can be more precisely

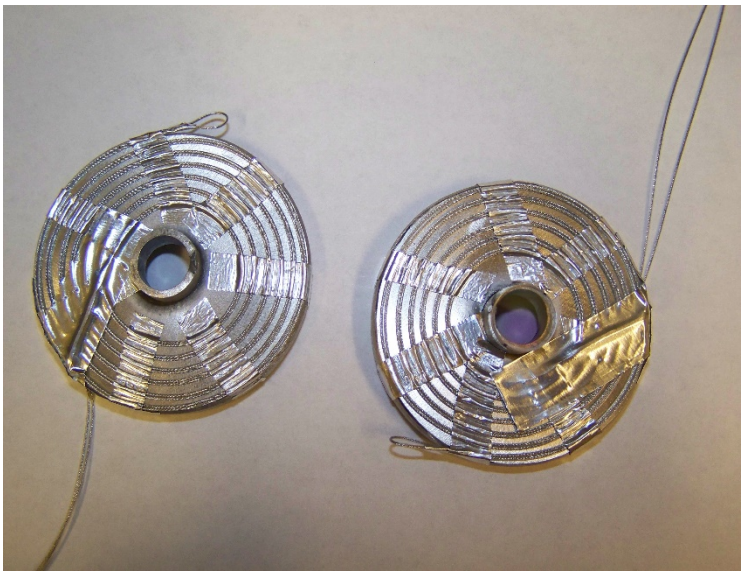

Figure 5.13 Heating coils wounded on inner most end cap. These coils provide continuous heating to the Cs sensor to maintain the optimum temperature.

tuned. The position of the potentiometer gives the relative output power, based on information from the manufacturer.

The diameter of the ultrasound probe is 6.5 mm and made of nonmagnetic material. The probe is inserted through the ports of the bottom end caps (Figure 5.14) and it is fixed onto a translational stage. Therefore fine adjustments of the probe height can be done easily. The sample holder is attached to the ultrasound probe.

The sample holder is made from Teflon (Figure 5.15). It is attached to the rubber holder, which holds the ultrasound probe. In the middle part of the holder has a 13 × 13 mm hole to bear the rubber attenuator. There is a deep grove around the attenuator. Silicone rubber form is placed inside the grove in order to prevent the transmission of ultrasound into the environment because it introduces some noise. Rubber form is a good ultrasound

absorbent as well as a good thermal insulator.  So most of theheat generated by ultrasound can be insulated and it may help to prevent any temperature gradients.

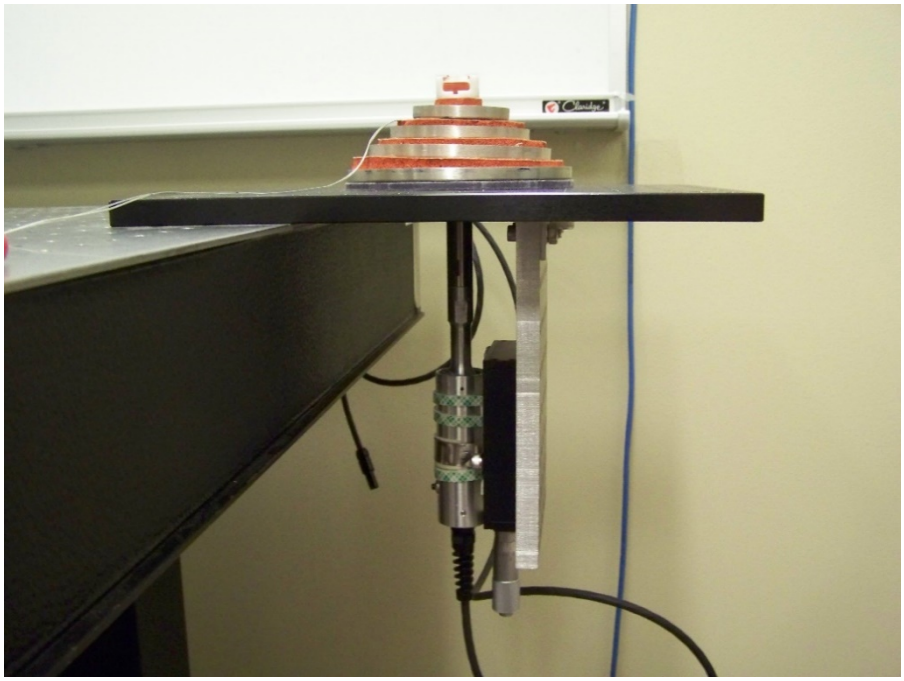

Figure 5.14 The ultrasound probe reaches the inner most layer of the shield through the ports of the bottom end caps. The sample holder is placed on top of the probe.

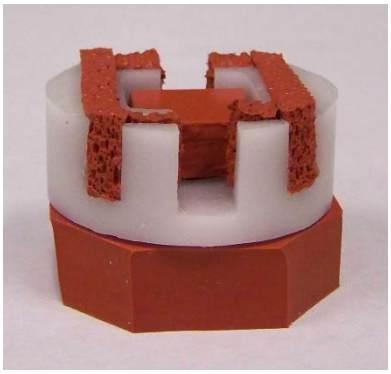

Figure 5.15 Sample holder with the attached rubber holder at the bottom part. In the middle part of the sample holder is a rubber attenuator.

### 5.2.7. Characterization of the instrument

We are now at the initial testing stage of the instrument. The first step is the testing of a magnetic signal. In order to do that we introduced a magnetic field via *z*- gradient coil on the Teflon coil holder using -0.1 V and 0.1 V square signal from a function generator (3314 A Hewlett Packard). The jump in the magnetic signal (Figure 5.16) represented the change in voltage from -0.1 V to 0.1 V. The instrument yet to be calibrated for a known magnetic fields.

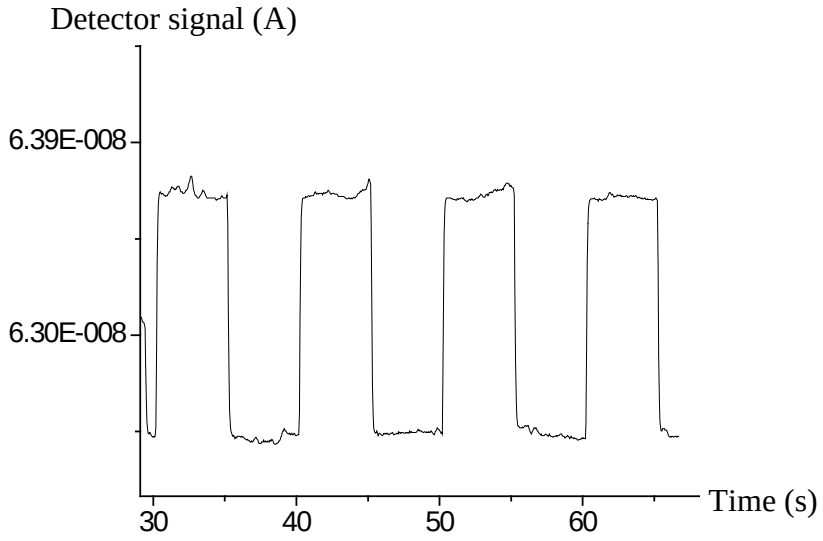


Figure 5.16Measuring a test magnetic field using the new instrument.

The next step was testing the square signal in the presence of ultrasound. In order to do that we used three different ultra sound powers (10%, 20% and 30%) with no sample. Figure 5.17 shows the results. The duration for ultrasound application was 30 s. All three traces with the ultrasound are not much deviated from the original signal without the ultrasound. So it shows the feasibility of using the ultrasound probe inside the shield. Our

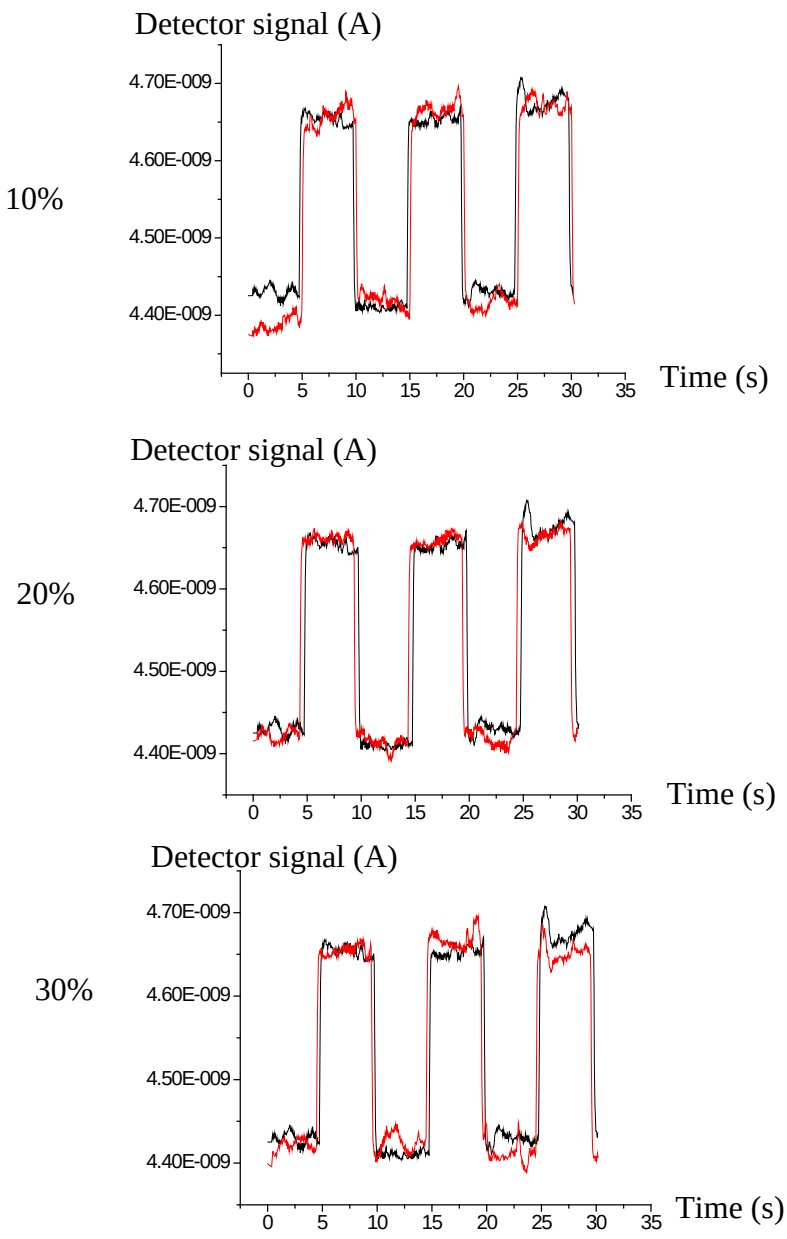


Figure 5.17 Testing magnetic field signal in the presence of ultrasound for three different powers. Red color traces represent the signal with the ultrasound.

future work for the instrument will include calibrating the instrument for magnetic fields, optimizing the parameters for better signal-to-noise ratio, monitoring the sensitivity of the instrument with time and finally testing with samples for resolving noncovalent bonds.

# Chapter 6

# Conclusions

In this work, development of a magnetic-based high resolution force spectroscopic technique was demonstrated. The technique is named as Force Induced Remnant Magnetization Spectroscopy (FIRMS). FIRMS precisely measures the binding forces between molecular pairs with high resolution. Therefore it is a valuable technique for quantitative and molecule-specific detection of noncovalent bonds.

The FIRMS technique provides well-defined and sequence-specific binding forces of DNA duplexes. The force distribution was as narrow as 1.8 pN, which is nearly an order of magnitude better than that of other force spectroscopic techniques. This feature enabled resolving multiple DNA bindings that differ only in one base within a single sample. The high force resolution also revealed that the binding forces of DNA depend on the position of the mismatching base. Therefore FIRMS is capable of distinguishing different DNA-DNA interactions and characterizing the binding strength of DNA duplexes.

Acoustic radiation force (ARF) generated by precisely attenuated ultrasound in the ultra-low power regime can be coupled with FIRMS to resolve molecular bonds. Noncovalent bonds of different antibodies and DNA duplexes with single-base force resolution can be resolved by ARF. Therefore ARF-based FIRMS is potentially capable of noninvasive mechanical manipulation of molecular interactions.

A new instrument has been constructed, which couples an ultrasound probe and a compact atomic magnetometer. Due to the small size of the ultrasound probe, it can be integrated with an atomic magnetometer by being placed inside the magnetic shield. The new instrument offers several new advantages, including miniaturized footprint and improved applicability in molecular detection. Although this instrument has not been optimized yet, the preliminary results strongly show the feasibility of using the ultrasound probe inside the shield. This instrument will facilitate the applications of FIRMS in multiplexed detecting and resolving molecular interactions.

# Bibliography


[1] S. P. Gubin (ed), *Magnetic nanoparticles* (WILEY-VCH Verlag GmbH & Co. KGaA, Weinheim, 2009)

[2] A. H. Morrrish, *The physical principles of magnetism*, (IEEE, New York, 2001)

[3] E. W. Lee, *Magnetism An Introductory Survey*, (Dover Publications, New York, 1970)

[4] M. Ashby, H. Shercliff, D. Cebon, *Materials Engineering, Science, Processing and Design*, (Elsevier, Oxford, 2007)

[5] Q. A. Pankhurst, J. Connolly, S. K. Jones, J. Dobson, *J. Phys. D: Appl. Phys.* **36,** R167 (2003).

[6] W. D. Callister, *Fundamentals of Materials Science and Engineering An Integrated Approach*, (John Wiley & Sons, Hoboken, 2005)

[7] R. Narayan (ed.), *Biomedical Materials*, (Springer Science+Business Media, Berlin, 2009)

[8] B. S. Mitchell, *An introduction to materials engineering and science for chemical and material engineers*, (John Wiley & Sons, Hoboken, 2004)

[9] J. Xu, K. Mahajan, W. Xue, J. O. Winter, M. Zborowski, J. J.Chalmers, *J. Magn. Magn. Mater.* **324**, 4189 (2012).

[10] A.-H. Lu, E. L. Salabas, F. Schüth, *Angew. Chem. Int. Ed.* **46**, 1222 (2007)

[11] M. C. Tan (ed), *Nanostructured Materials for Biomedical Applications,* (Transworld Research Network, Trivandrum, 2009)

[12] V. P. Torchilin (ed), *Nanoparticulates as drug carries*, (Imperial College Press, London, 2006)

[13] I. Koh, L. Josephson, *Sensors* **9**, 8130 (2009)

[14] A. P. Astalan, C. Jonasson, K. Petersson, J. Blomgren, D. Ilver, A. Krozer, C. Johansson, *J. Magn. Magn. Mater.* **311,** 166 (2007)

[15] T. Knopp, T. M. Buzug, *Magnetic particle imaging*, (Springer-Verlag, Berlin 2012)

[16] A. Akbarzadeh, M. Samiei, S. Davaran, *Nanoscale Res. Lett.* **7**, 144 (2012)

[17] D. S. Wang, M. D. Dake, J. M. Park, M. D. Kuo, *J. Vasc. Interv. Radiol.* **17**, 1405 (2006)

[18] T. F. Massoud, S. S. Gambhir, *Genes Dev.* **17**, 545 (2003)

[19] A. Rahmima, H. Zaidib, *Nucl. Med. Commun.* **29**, 193 (2008)

[20] J. P. Christiansen, J. R. Lindner, *Eng. Med. Biol. Mag.* **93**, 809 (2005)

[21] J.P. Basilion, S. Yeon, R. Botnar, *Curr. Top. Dev. Biol.* **70**, 1 (2005)

[22] L. Yao, S. Xu, *Angew. Chem. Int. Ed.* **50**, 4407 (2011)

[23] L. Yao, S. Xu, *J. Phys. Chem. B* **116** , 9944 (2012)

[24] C. Albrecht, K. Blank, M. L. Mülthaler, S. Hirler, T. Mai, I. Gilbert, S. Schiffmann, T. Bayer, H. C. Schaumann, H. E. Gaub, *Science* **301**, 367 (2003)

[25] S. Xu, M. H. Donaldson, A. Pines, S. M. Rochester and D. Budker, V. V. Yashchuk, *Appl. Phys. Lett.* **89**, 224105 (2006)

[26] F. Jelezko, *Physics* **7**, 43 (2014)

[27] H. B. Dang, A. C. Maloof, M. V. Romalis, *Appl. Phys. Lett.* **97**, 151110 (2010)

[28] D. Budker, M. V. Romalis, *Nat. Phys.* **3**, 227 (2007)

[29] O. Knudsen, *Arch. Hist. Exact Sci.* **15**, 235 (1976)

[30] M. Faraday, *Philos. Trans. R. Soc. (London)* **136**, 1 (1846).

[31] M. Faraday, *Philos. Mag.* **28**, 294 (1846).

[32] G. Charier, *Introduction to Optics* (Springer, New York, 2005)

[33] M. Faraday, *Experimental Research in electricity* (Taylor, London, 1855)

[34] D. Budker, W. Gawlik, D.F. Kimball, S.M. Rochester, V.V. Yashchuk, A. Weis , *Rev. Mod. Phys.* **74**, 1153 (2002)

[35] D. Macaluso, O. M. Corbino, *Nuovo Cimento*, **8**, 257, (1898).

[36] D. Macaluso, O. M. Corbino, *Nuovo Cimento*, **9**, 384, (1898).

[37] W. Voigt, Kgl. Ges. Wiss. Nachr., *Math.-Phys. Kl.* **1898**, 329 (1898).

[38] W. Voigt, Kgl. Ges. Wiss. Nachr., Math.-Phys. Kl. **1898**, 355 (1898).

[39] D. Budker, D.J. Orlando, V.V. Yashchuk, *Am. J. Phys.* **67**, 584 (1999).

[40] G. J. Roberts, P. E. G. Baird, M. W. S. M. Brimicombe, P. G. H. Sandars, D. R. Selby, D. N. Stacey, *J. Phys. B* **13**, 1389 (1980).

[41] V. N. Novikov, O. P. Sushkov, and I. B. Khriplovich, Opt. Spectrosk. **43**, 621 (1977)

[42] N. Papageorgiou, A. Weis, V. A. Sautenkov, D. Bloch, M. Ducloy, *Appl. Phys. B* **59**, 123 (1994).

[43] X. Chen, V. L. Telegdi, A. Weis, *J. Phys. B* **20**, 5653 (1987).

[44] D. Kimball, Non-Linear Magneto-Optical Rotation with Frequency-Modulated Light (2013). http://budker.berkeley.edu/D_Kimball_Qual/.

[45] D. Budker, V. Yashchuk, M. Zolotorev, *Phys. Rev. Lett.* **81**, 5788 (1998).

[46] D. Budker, D. F. Kimball, D. P. DeMille, *Atomic Physics: an exploration through problems and solutions* (Oxford University Press, Oxford, 2004).

[47] S. Gröger, (2005) Laser-pumped cesium magnetometers for the PSI-nEDM experiment, (Doctoral Dissertation).

[48] W. Gawlik, J. Kowalski, R. Neumann, F. Träger, *Opt. Commun.* **12**, 400 (1974).

[49] D. Budker, D. F. Kimball, S. M. Rochester, V. V. Yashchuk, *Phys. Rev. A* **65**, 033401 (2002).

[50] L. M. Barkov, D. A. Melik-pashayev, M. S. Zolotorev, *Opt. Commun.* **70**, 467 (1989)

[51] S. M. Rochester, D. Budker, *Am. J. Phys.* **69**, 450 (2001)

[52] E. B. Alexandrov, V. A. Bonch-Bruevich, *Opt. Engin.* **31**, 711 (1992).

[53] E. B. Alexandrov, M. V. Balabas, A. S. Pasgalev, A. K. Vershovskii, N. N. Yakobson, *Laser Phys.* **6**, 244 (1996).

[54] W. Gawlik, S. Pustelny, *Photonics Lett. Pol.*, **1**, 34 (2009)

[55] D. Budker, D. F. Kimball1, S. M. Rochester1, V. V. Yashchuk, M. Zolotorev, *Phys. Rev. A* **62**, 043403 (2000)

[56] D. Budker, D.F. Kimball, V.V. Yashchuk, and M. Zolotorev, Phys. Rev. A **65**, 055403 (2002).

[57] I. K. Kominis, T. W. Kornack, J. C. Allred, M. V. Romalis, *Nature* **422**, 596 (2003).

[58] S. Huard, *Polarization of light* (Wiley, New York, 1997).

[59] D. Yu, N. Garcia, S. Xu, *Concept. Magn. Reson. A*, **34**, 124 (2009)

[60] L. Yao, S.-J. Xu, *Angew. Chem., Int. Ed.* **48**, 5679 (2009)

[61] L. Yao, Y. Li, T. Tsai, S.-J. Xu and Y.Wang, *Angew. Chem., Int. Ed.* 52, 14041 (2013)

[62] K. R. Chaurasiya, T. Paramanathan, M. J. McCauley, M. C. Williams, *Phys. Life Rev.* **7**, 299 (2010)

[63] C. Bustamante, Z. Bryant, S. B. Smith, *Nature* **421**, 423 (2003)

[64] M. D. Brenner, R. Zhou, T. Ha, *Biopolymers* **95**, 332 (2011)

[65] P. A. Sharp, *Genes Dev.* **13**, 139 (1999)

[66] P. M. D. Severin, D. Ho, H. E. Gaub, *Lab Chip* **11**, 856 (2011)

[67] H. Wang, R. Yang, L. Yang, W. Tan, *ACS Nano* **3**, 2451 (2009)

[68] R. J. Macfarlane, B. Lee, M. R. Jones, N. Harris, G. C. Schatz, *Science* **334**, 204 (2011)

[69] A. Rajendran, M. Endo, H. Sugiyama, *Angew. Chem. Int. Ed.* **51**, 874 (2012)

[70] G. U. Lee, L. A. Chrisey, R. J. Colton, *Science* **266**, 771 (1994)

[71] R. Krautbauer, M. Rief, H. E. Gaub, *Nano Lett.* **3**, 493 (2003).

[72] T. Strunz, K. Oroszlan, R. Schäfer, H-J Güntherodt, *Proc. Natl. Acad. Sci.* **96**, 11277 (1999)

[73] U. Bockelmann, P. Thomen, B. Essevaz-Roulet, V. Viasnoff, F. Heslot, *Biophys. J.* **82**, 1537 (2002)

[74] S. J. Koch, A. Shundrovsky, B. C. Jantzen, M. D. Wang, *Biophys. J.* **83**, 1098 (2002)

[75] D. B. Ritchie, D. A. N. Foster, M. T. Woodside, *Proc. Natl. Acad. Sci. USA* **109**, 16167 (2012)

[76] D. Ho, J. L. Zimmermann, F. A. Dehmelt, U. Steinbach, M. Erdmann, P. Severin, K. Falter, H. E. Gaub, *Biophys. J.* **97**, 3158 (2009)

[77] X. Qu, L. Lancaster, H. F. Noller, C. Bustamante, I. Tinoco, *Proc. Natl. Acad. Sci. USA* **109**, 14458 (2012)

[78] A. Ulman, *An Introduction to Ultrathin Organic Films from Langmuir-Blodgett to Self-Assembly* (Academic Press, Boston, 1991)

[79] G. Georgiadis, K. P. Peterlinz, A.W. Peterson, *J. Am. Chem. Soc.* **122**, 3166. (2000)

[80] T. M. Herne, M. J. Tarlov, *J. Am. Chem. Soc.* **119**, 8916 (1997)

[81] R. Levicky, T. M. Herne, M. J. Tarlov, S. K. Satija, *J. Am. Chem. Soc.* **120**, 9787 (1998)

[82] R. Wirtz, C. Wälti, W. A. Germishuizen, M. Pepper, A. P. J. Middelberg, A. G. Davies, *Nanotechnol.* **14**, 7 (2003)

[83] K. Halvorsen, W. P. Wong, *Biophys. J.* **98**, 53 (2010)

[84] M. Rief, H. Clausen-Schaumann, H. E. Gaub, *Nat. Struct. Biol.* **6**, 346 (1999)

[85] U. Bockelmann, P. Thomen, F. Heslot, *Biophys. J.* **87**, 3388 (2004)

[86] L. H. Pope, M. C. Davies, C. A. Laughton, C. J. Roberts, S. J. B. Tendler, P. M. Williams, *Eur. Biophys. J.* **30**, 53 (2001)

[87] E. Evans, K. Ritchie, *Biophys. J.* **72**, 1541 (1997)

[88] J. M. Fernandez, H. B. Li, *Science* **303**, 1674 (2004)

[89] S. Garcia-Manyes, J. Brujić, C. L. Badilla, J. M. Fernández, *Biophys. J.* **93**, 2436 (2007)

[90] M. Capitanio, M. Canepari, M. Maffei, D. Beneventi, C. Monico, F. Vanzi, R. Bottinelli, F. S. Pavone, *Nat. Method* **9**, 1013 (2012)

[91] B. D. Sattin, A. E. Pelling, M. C. Goh, *Nucleic Acids Res.* **32**, 4876 (2004)

[92] T. A. Taton, C. A. Mirkin, R. L. Letsinger, *Science* **289**, 1757 (2000)

[93] J. SantaLucia, D. Hicks, Annu. Rev. Biophys. *Biomol. Struct.* **33**, 415 (2004)

[94] R. Lavery, A. Lebrun, J-F. Allemand, D. Bensimon, V. Croquette, *J. Phys.: Condend. Matter* **14**, 383 (2002)

[95] J. Šponer, P. Jurečka, I. Marchan, F. J. Luque, M. Orozco, P. Hobza, *Chem. Eur. J.* **12**, 2854 (2006)

[96] P. L. Vanegas, T. S. Horwitz, B. M. Znosko, *Biochemistry* **51**, 2192 (2012)

[97] T. B. Xia, J. SantaLucia, M. E. Burkard, R. Kierzek, S. J. Schroeder, X. Q. Jiao, C. Cox, D. H. Turner, *Biochemistry* **37**, 14719 (1998)

[98] Y. R. Chemla, H. L. Grossman, Y. Poon, R. McDermott, R. Stevens, M. D. Alper, J. Clarke, *Proc. Natl. Acad. Sci. USA* **97**, 14268 (2000)

[99] J. W. Weisel, H. Shuman, R. I. Litvinov, *Curr. Opin. Struct. Biol.* **13**, 227 (2013)

[100] V. T. Moy, E.-L. Florin, H. E. Gaub, *Science* **266**, 257 (1994)

[101] J. Kim, C.-Z. Zhang, X. Zhang, T. A. Springer, *Nature* **466**, 992 (2010)

[102] J. W. Shaevitz, E. A. Abbondanzieri, R. Landick, S. M. Block, *Nature* **426**, 684 (2003)

[103] L. De Silva, L. Yao, Y. Wang, S.-J. Xu, *J. Phys. Chem. B* **117**, 7554 (2013)

[104] G. T. Silva, S. Chen, L. P. Viana, *Phys. Rev. Lett.* **96**, 234301 (2006)

[105] T.G. Leighton, *Prog. Biophys. Mol. Biol.* **93**, 3 (2007)

[106] N. H. Ince, G. Tezcanli, R. K. Belen, I. G. Apikyan, *Appl. Catal., B* **29**,167 (2001)

[107] A. Gáplovsky´, Š. Toma, J. Donovalová, *J. Photochem. Photobiol. A* **191**, 162 (2007)

[108] T. J. Mason, J. P. Lorimer, *Applied Sonochemistry the uses of Power ultrasound in Chemistry and processing*, (Wiley-VCH Verlag GmbH, Weinheim, 2002)

[109] D. Dalecki, *Annu. Rev. Biomed. Eng.* **6**, 229 (2004)

[110] S.-K. Han, S.-N. Nam, J.-W. Kang, *Water Sci. Technol.* **46**, 7 (2002)

[111] J. L. Luche, *Synthetic Organic Chemistry*, (Plenum Press, New York, 1999)

[112] J. Lindley, T. J. Mason, *Chem. Soc. Rev.* **16**, 275 (1987)

[113] S. R. Jezowski, L. Zhu, Y. Wang, A. P. Rice, G. W. Scott, C. J. Bardeen, E. L. Chronister, *J. Am. Chem. Soc.* **134**, 7459 (2012)

[114] J.-L. Capelo-Martínez (ed), *Ultrasound in Chemistry: Analytical Applications*, (Wiley-VCH Verlag GmbH, Weinheim, 2009)

[115] H. R. Guzman, D. X. Nguyen, S. Khan, M. R. Prausnitz, *J. Acoustic. Soc. Am.* **110**, 588 (2001)

[116] P. N. T. Wells, *Phys. Med. Biol.* **51**, 83 (2006)

[117] C. R. Hickenboth, J. S. Moore, S. R. White, N. R. Sottos, J. Baudry, S. R. Wilson, *Nature* **446**, 423 (2007)

[118] J. N. Brantley, K. M. Wiggins, C. W. Bielawski, *Science* **333**, 1606 (2011)

[119] K. L. Berkowski, S. L. Potisek, C. R. Hickenboth, J. S. Moore, *Macromolecules* **38**, 8975 (2005)

[120] A. Piermattei, S. Karthikeyan, R. P. Sijbesma, *Nat. Chem.* **6**, 133 (2009)

[121] P. L. Ey, S. J. Prowse, C. R. Jenkin, *Immunochemistry* **15**, 429 (1978)

[122] T. Kikuchi, Y. Uchida, *J. Phys.: Conf. Ser.* **279**, 012012 (2011)

[123] M. Settnes, H. Bruus, *Phys. Rev. E* **85**, 016327 (2012)

[124] J.-L. Capelo-Martinez (ed), *Ultrasound in Chemistry. Analytical Applications*, (Wiley-VCH, Weinheim, 2009)

[125] http://mfold.rna.albany.edu/?q=mfold.

[126] R. Zheng, L. H. Le, M. D. Sacchi, D. Ta, E. Lou, *Phys. Med. Biol.* **52**, 5855-5869 (2007).

[127] F. G. Mitri, *New J. Phys.* **8**, 138 (2006)

[128] L. De Silva, L. Yao, S.-J. Xu, *Chem. Comm.*, doi: 10.1039/c4cc03305a (2014).

[129] V. V. Yashchuk, D. Budker, J. R. Davis, *Rev. Sci. Instrum.* **71**, 341 (2000)

[130] K. L. Corwin, Z.-T. Lu, C. F. Hand, R. J. Epstain, C. E. Wieman, *Appl. Opt.* **37**, 3295 (1998)

[131] K. C. Harvey, C. J. Myatt, *Opt. Lett.* **16**, 910 (1991)